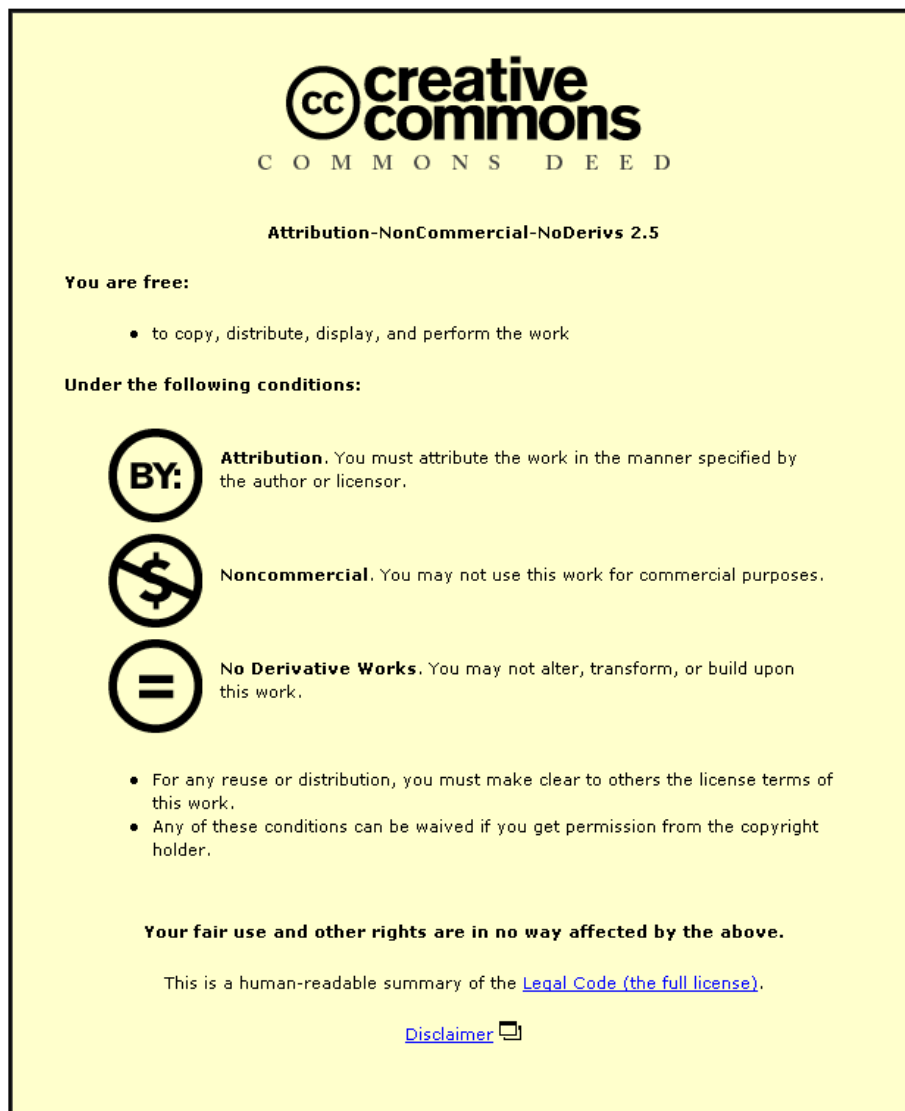


This item was submitted to Loughborough University as a PhD thesis by the author and is made available in the Institutional Repository (<https://dspace.lboro.ac.uk/>) under the following Creative Commons Licence conditions.



For the full text of this licence, please go to:
<http://creativecommons.org/licenses/by-nc-nd/2.5/>

**NOVEL METHODS OF DRAG REDUCTION FOR
SQUAREBACK ROAD VEHICLES**

BY ROB LITTLEWOOD

DOCTORAL THESIS

**SUBMITTED IN PARTIAL FULFILLMENT OF THE REQUIREMENTS
FOR THE AWARD OF DOCTOR OF PHILOSOPHY OF
LOUGHBOROUGH UNIVERSITY**

APRIL 2013

© R.P.LITTLEWOOD 2013

ABSTRACT

Road vehicles are still largely a 'consumer product' and as such the styling of a vehicle becomes a significant factor in how commercially successful a vehicle will become. The influence of styling combined with the numerous other factors to consider in a vehicle development programme means that the optimum aerodynamic package is not possible in real world applications.

Aerodynamicists are continually looking for more discrete and innovative ways to reduce the drag of a vehicle. The current thesis adds to this work by investigating the influence of active flow control devices on the aerodynamic drag of square back style road vehicles. A number of different types of flow control are reviewed and the performance of synthetic jets and pulsed jets are investigated on a simple 2D cylinder flow case experimentally.

A simplified $\frac{1}{4}$ scale vehicle model is equipped with active flow control actuators and their effects on the body drag investigated. The influence of the global wake size and the smaller scale in-wake structures on vehicle drag is investigated and discussed. Modification of a large vortex structure in the lower half of the wake is found to be a dominant mechanism by which model base pressure can be influenced. The total gains in power available are calculated and the potential for incorporating active flow control devices in current road vehicles is reviewed. Due to practicality limitations the active flow control devices are currently ruled out for implementation on a road vehicle.

The knowledge gained about the vehicle model wake flow topology is later used to create drag reductions using a simple and discrete passive device. The passive modifications act to support claims made about the influence of in wake structures on the global base pressures and vehicle drag. The devices are also tested at full scale where modifications to the vehicle body forces were also observed.

ACKNOWLEDGEMENTS

I would like to thank my supervisor Martin Passmore for his continued support from when I was an undergraduate student and throughout my postgraduate studies. I would also like to thank Rob Hunter and Stacey Prentice for their work to keep the wind tunnel running and supply me with various incarnations of wind tunnel models and components. Thanks also go to all my fellow PhD students, undergraduate students and staff within the Aeronautical and Automotive Engineering Department at Loughborough University who helped along the way.

I would also like to thank Jeff Howell for the wealth of advice he provided on automotive bluff body testing, and Adrian Gaylard at Jaguar Land Rover for his continued interest and support of the work.

Finally thanks go to my fiancé, parents and whole family for their continued support and patience.

Nomenclature

A	Frontal area (m ²)
a	Sensor temperature coefficient
α_0	Overheat ratio
A_d	Coefficient of tyre resistance (static)
AP_{NET}	Net change in aerodynamic power (W)
ASC	Acoustic streaming criterion
A_t	Coefficient of transmission resistance (static)
A_u	Coefficient of undriven wheel resistance (static)
b	Jet characteristic length (Hole: diameter, Slot: width) (m)
B_d	Coefficient of tyre resistance (dynamic)
B_t, C_t	Coefficients of transmission resistances (dynamic)
B_u	Coefficient of undriven wheel resistance (dynamic)
C_μ	Jet momentum coefficient
C_b	Pressure contributions from base
C_d	Coefficient of drag
C_F	Coefficient of force
C_f	Pressure contributions from skin friction
CFD	Computational fluid dynamics
C_k	Pressure contributions from front of model
C_l	Coefficient of lift
C_{lr}	Coefficient of rear lift
C_p	Coefficient of pressure
$\overline{C_p}$	Area weighted pressure coefficient
C_s	Pressure contributions from slant
D	Model characteristic length scale (m)
d	Displacement (m)
E	Blockage ratio
e_μ	Statistical accuracy
E_a	Applied voltage
E_{corr}	Corrected applied voltage
f	Frequency (Hz)
F^+	Reduced actuation frequency, (usually a multiple of a characteristic shedding frequency)

F_{DRAG}	Drag force (N)
FoV	Field of view
F_{TR}	Tractive resistance
g	Gravity (9.81)
H	Characteristic length/ height (m)
I_0	Jet momentum
L	Characteristic length (m)
L_{advec}	Advection length (m)
LDA	Laser doppler annemometry
\dot{m}	Mass flow rate (kg/s)
M	Vehicle mass (Kg)
MSBC	Moving surface boundary layer control
N	Number of samples
P	Pressure (Pa)
p	Pressure local to tapping measurement (Pa)
p_∞	Reference pressure in freestream (Pa)
P_{AERO}	Aerodynamic power (W)
PIV	Particle image velocimetry
q	Freestream dynamic pressure (Pa)
R	Specific gas constant for air (287)
Re	Reynold's number
Re_{10}	Jet Reynold's number
RMS	Root mean squared
σ_d	Standard deviation of displacement (m)
SJ	Synthetic jet
σ_t	Standard deviation of time (s)
St	Strouhal number
St_{act}	Actuation Strouhal number
STOL	Short take off and landing
σ_v	Standard deviation of veelocity (m/s)
T	Temperature (K)
t	Time (s)
t^*	distribution factor for a given confidence level
T_0	Ambient temperature at the time of setting the overheat

T_a	Ambient temperature at the time of sampling
T_w	Hot wire sensor operating voltage
U_∞	Freestream velocity (m/s)
U_c	Advection speed (m/s)
U_j	Jet exit velocity (m/s)
V	Velocity (m/s)
η	Jet efficiency
μ	Kinematic viscosity
ρ	Density (Kg/m ³) (Air = 1.225)
ρ_j	Jet fluid density (Kg/m ³)
ρ_0	Freestream density (kg/m ³)
θ	Angle (degrees)

TABLE OF CONTENTS

Nomenclature	iv
1.0 Introduction	2
1.1 Tractive Resistance.....	3
1.2 Sources of Drag	4
1.2.1 Base Pressure and Vortex Drag.....	5
1.2.2 Rear edge conditioning.....	8
1.2.3 Drag Reduction Techniques	9
1.3 Drag Reduction Techniques; Passive	9
1.3.1 Diffusers.....	9
1.3.2 Boat Tailing.....	10
1.3.3 Flaps and Plates.....	12
1.4 Drag Reduction Techniques; Active.....	14
1.4.1 Moving Surface Boundary Layer Control (MSBC).....	14
1.4.2 Continuous Suction	15
1.4.3 Continuous Blowing.....	15
1.4.4 Synthetic Jet Actuators.....	18
1.5 Drag Reduction Techniques; Further Investigation.....	27
2.0 Experimental Method	30
2.1 Experimental Uncertainty.....	30
2.2 Wind Tunnel and Force Balance	31
2.3 Surface Pressure Measurement.....	33

2.4	Hot Wire Anemometry	34
2.5	Particle Image Velocimetry	35
2.5.1	Seeding and Camera Field of View.....	36
2.5.2	Image Acquisition	37
2.5.3	Data Processing.....	38
2.5.4	Post Processing.....	39
2.5.5	PIV Resolution, Accuracy and Precision	40
2.5.6	PIV Summary.....	47
3.0	Baseline Vehicle Configuration and Passive Optimisation	49
3.1	Introduction	49
3.2	Force and Pressure Measurement Results	52
3.3	PIV Results.....	58
3.4	Discussion and Implications for Further Work	65
4.0	Active Control Actuator Design and Testing.....	68
4.1	Introduction	68
4.2	Initial Testing.....	70
4.2.1	Low Frequency Jet	70
4.2.2	High Frequency Jet	73
4.2.3	PIV and LDA Analysis of ‘Speaker Driven’ Synthetic Jet and Pneumatic Pulsed Jet ...	74
4.3	2D Cylinder Testing	79
4.3.1	Experimental Setup	79
4.3.2	Results; Pressure Measurements	81

4.4	Results; Balance Measurements	86
4.5	Discussion.....	88
5.0	Active Control Constant Blowing – Experiments, Results and Discussion	91
5.1	Model.....	91
5.2	Slot Exit Velocity Measurements	93
5.2.1	Jet Characterisation	94
5.3	Force Measurements.....	96
5.4	Pressure Measurements	97
5.5	PIV.....	97
5.6	Results – Balance Measurements	98
5.7	Results - Pressure Measurements	101
5.8	Results - PIV.....	103
5.9	Net Drag Changes.....	109
5.10	Discussion.....	111
6.0	Active Control Pulsed Blowing – Experiments, Results and Discussion..	114
6.1	Introduction	114
6.2	Model.....	114
6.3	Jet Characterisation.....	117
6.4	Balance Results	120
6.5	PIV.....	123
6.5.1	Configuration B.....	124
6.5.2	Configuration C.....	127

6.5.3	Configuration D	130
6.6	Discussion.....	132
7.0	Passive Control of In Wake Structures – Experiments, Results and Discussion	135
7.1	Introduction	135
7.2	Experimental Configurations.....	135
7.2.1	Model Scale.....	135
7.2.2	Full Scale Vehicle Testing	136
7.3	Experimental Results.....	139
7.3.1	Model Scale.....	139
7.3.2	Full Scale.....	143
7.4	Discussion.....	145
8.0	Conclusions and Further Work	148
9.0	References	151

Table of Figures

Figure 1.1 - Forces opposing the motion of a typical road vehicle (Ford Escort) 2

Figure 1.2 - Percentage contributions of resistive forces contributing to Equation 1 (Ford Escort)..... 3

Figure 1.3 Wake sizes of different vehicle shapes (Heisler, 2002)..... 5

Figure 1.4 - Effect of backlight angle on C_d (Barnard, 1996)..... 6

Figure 1.5 - Isosurfaces of zero total pressure on Ahmed car model for increasing back angle (Keating, Shock and Chen, 2008) 7

Figure 1.6 - Variation of drag with base slant angle (Ahmed, Ramm and Faltin, 1984) 7

Figure 1.7 - Drag due to large trailing radii (Kee, Kim and Lee, 2001) 8

Figure 1.8 - Audi A2 rear spoiler configuration..... 9

Figure 1.9 – Drag produced by an underbody diffuser at various angles and ride heights (Cooper et al., 1998) 10

Figure 1.10 - Drag produced by an underbody diffuser at various angles and ride heights (Jowsey, 2008) 10

Figure 1.11 - fully streamlined rigid boat tail (Lanser and Ross, 1991)..... 10

Figure 1.12 - Shortened rigid boat tail fairing (Wong and Mair, 1983)..... 10

Figure 1.13 - Boat tailing using extension plates (Khalighi, Zhang and Koromilas, 2001) 11

Figure 1.14 - Pressure coefficient at rear of bluff body left: standard setup right: with extension plates (Khalighi, Zhang and Koromilas, 2001) 11

Figure 1.15 - 2D bluff body incorporating splitter plates of various lengths (Bearman, 1965)..... 12

Figure 1.16 - Spanwise base pressure distribution. x = without splitter plate and end plates, o = without splitter plates but with end plates, □ = with splitter plate but without end plates (Bearman, 1965) . 12

Figure 1.17 - Rear Flap configuration for drag reduction (Kowata et al., 2008) 13

Figure 1.18 - Flaps model (Beaudoin and Aider, 2008) 13

Figure 1.19 - PIV vortex reduction (Beaudoin and Aider, 2008)..... 14

Figure 1.20 – Moving surface boundary layer control on a bluff body (Roumeas, 2006) 15

Figure 1.21 - Effect of continuous suction on Ahmed car (Roumeas, 2006) 15

Figure 1.22 - Blowing technique on a wing (Englar, 2003)..... 16

Figure 1.23 – Continuous blowing at various angles into the wake of a bluff body (Rouméas, Gilliéron and Kourta, 2006) 17

Figure 1.24 - Synthetic Jet Illustration (Glezer and Amitay, 2002) 18

Figure 1.25 - Variation of the pressure coefficient around a tube with increasing dimensionless actuation frequency $SrD_{act} = \bullet; 0.24, \Delta; 0.50, *; 0.83$ and $-$; base line flow (Glezer, Amitay and Honahan, 2005) 19

Figure 1.26 - Pressure distribution around 2D cylinder: \square unactuated with laminar BL, \circ unactuated with tripped turbulent BL, \bullet actuated with tripped turbulent BL (Glezer, Amitay and Honahan, 2005) 20

Figure 1.27 - Pressure distribution around 2D cylinder: \bullet unactuated, tripped turbulent BL, \square (thin) low level actuation, tripped turbulent BL, \square (thick) high level actuation, tripped turbulent BL (Béra et al., 2000) 20

Figure 1.28 – Velocity vectors and rotational intensity (Béra et al., 2000) 21

Figure 1.29 - 2D diffuser (Brunn and Nitsche, 2006) 22

Figure 1.30 - Model configuration (Leclerc and Levallois, 2006) 22

Figure 1.31 - Cd vs reduced actuator frequency F^+ (Leclerc and Levallois, 2006) 22

Figure 1.32 - D-Shaped body used in vortex suppression experiments (Pastoor et al., 2008) 23

Figure 1.33 – Instantaneous pressure distribution and wake flow distribution behind a D shaped bluff body, without control (Pastoor et al., 2008) 24

Figure 1.34 - Instantaneous pressure distribution and wake flow distribution behind a D shaped bluff body, controlled by SJ actuators (Pastoor et al., 2008) 24

Figure 1.35 – Velocity vector plots at different actuator frequency F^+ (Amitay and Glezer, 2002) 25

Figure 1.36 - Recirculation bubble and shape 26

Figure 1.37 - Jet vectoring (Smith and Glezer, 2002) 26

Figure 2.1 - Loughborough University Wind Tunnel 31

Figure 2.2 - Example of drag coefficient measurement for a road car bluff 33

Figure 2.3 - Pressure scanner and CanDaq 33

Figure 2.4 - Jet velocity measurement using hot wire 34

Figure 2.5 – Typical PIV configuration (Raffel et al., 2007) 35

Figure 2.6 – Onset of peak locking 37

Figure 2.7 - Non-peak locked PDF 37

Figure 2.8 - Camera and laser timing sequence (Hollis, 2004) 37

Figure 2.9 - Example interrogation cell correlation plot 38

Figure 2.10 - PIV interrogation cell passes 39

Figure 2.11 – Instantaneous PIV velocity field of squareback vehicle model showing vector resolution achieved..... 42

Figure 2.12 - a) Synthetic and b) calculated data..... 43

Figure 2.13 - Uncertainty in velocity measurement 44

Figure 2.14 - Measurement uncertainty in velocity magnitude for example wake flow data. Contour plots show statistical uncertainty using averages of A)200 B) 500 and C) 1000 instantaneous image samples 46

Figure 3.1 - Windsor model showing insert to facilitate different rear chamfer angles 49

Figure 3.2 - Windsor model and interchangeable rear chamfer components 50

Figure 3.3 - Pressure tapping locations..... 51

Figure 3.4 - Isometric view of PIV system configuration 51

Figure 3.5 – Coefficient of drag vs Reynolds number for Windsor model 52

Figure 3.6 - Coefficient of drag vs chamfer angle 53

Figure 3.7 - Comparison of current aspect ratio slant with previous higher aspect ratio investigations (Howell and Le Good, 2008)..... 54

Figure 3.8 - Coefficient of lift vs chamfer angle 55

Figure 3.9 - Contour plots of coefficient of pressure on the base area of the model for: a) Square-back; b) 4° chamfer; c) 8° chamfer; d) 12° chamfer; e) 16° chamfer and f) 20° chamfer configurations. Dotted black line illustrates slant-base intersection point 56

Figure 3.10 - Coefficient of drag vs chamfer angle from balance measurements and calculated area weighted pressure measurements 57

Figure 3.11 - Coefficient of drag vs chamfer angle with and without PIV equipment in place 58

Figure 3.12 - Time averaged PIV vector plots for: a) square-back; b) 4° chamfer; c) 8° chamfer; d) 12° chamfer and e) 20° chamfer 61

Figure 3.13 - Time averaged PIV streamline plots for: a) square-back; b) 4° chamfer; c)12° chamfer and d) 20° chamfer 62

Figure 3.14 - Example instantaneous PIV images of the Square-back configuration showing vector arrows and streamlines in the background..... 64

Figure 4.1 - Acoustic streaming criterion (McKormick, 2000)..... 69

Figure 4.2 - Synthetic jet with characteristic vortices (Glezer and Amitay, 2002)..... 69

Figure 4.3 - Single frame from high speed camera images of synthetic jet at 50Hz 71

Figure 4.4 - 50 Hz small diameter cylinder..... 72

Figure 4.5 - 50Hz 200mm OD cylinder 73

Figure 4.6 - Schematic of high frequency jets	74
Figure 4.7 - Speaker driven SJ rig for time resolved PIV studies	75
4.8 - Phase averaged PIV (left) and LDA (right) measurements of the 50Hz SJ centreline at time steps of 2ms (top) and 5ms (bottom) viewed perpendicular to the slot axis (Plackett, 2009)	76
4.9 - Phase averaged PIV data of 50Hz SJ viewing along the slot axis at time steps of 2,4 and 6ms	77
4.10 - Velocity vs time plot for the centre line of the SJ running at 50Hz acquired using LDA (Plackett, 2009)	78
4.11 - Velocity vs time plot for the centre line of the pulsed jet running at 5Hz acquired using LDA (Plackett, 2009)	78
Figure 4.12 - Cylinder rig setup in Loughborough University wind tunnel	80
Figure 4.13 - Close up of jet exit and presure tappings	80
Figure 4.14 - Variation of Strouhal number with Reynolds number for flow around a cylinder (White, 1991)	81
Figure 4.15 - Coefficient of pressure around 2D tube at $Re = 1.48 \times 10^5$ (Laminar)	82
Figure 4.16 - Coefficient of pressure around 2D tube at $Re = 2.22 \times 10^5$ (Transitional).....	83
Figure 4.17 - Coefficient of pressure around 2D tube at $Re = 2.96 \times 10^5$ (Transitional/Turbulent)	84
Figure 4.18- Variations of C_p on a tube with a synthetic jet at $\theta=120^\circ$	85
Figure 4.19 - Coefficient of pressure around 2D tube at $Re = 3.70 \times 10^5$ (Fully Turbulent)	85
Figure 4.20 - C_d of tube with varying actuation frequency	87
Figure 4.21 - C_l of tube with varying actuation frequency	87
Figure 4.22 - Variation of the lift and the pressure drag coefficients with Sr_{Dact} (Glezer, Amitay and Honahan, 2005).....	88
Figure 5.1 - Winsor model in working section showing NACA0021 wing profile.....	91
Figure 5.2 – Configuration under working section showing feed lines into model	92
Figure 5.3 - Windsor model showing pressurised cavity and jet angle adaptor component	93
Figure 5.4 - Model dimensions and geometric jet exit configurations.....	93
Figure 5.5 - Example hot wire measurement of jet exit velocity profile	95
Figure 5.6 - Jet exit velocity contour plot at different spatial locations	96
Figure 5.7 - Accuracy of C_d measurements.....	96
Figure 5.8 - PIV experimental setup	98
Figure 5.9 - Changes in balance measured C_d for configuration B at ride heights of 10.3%, 13.8% and 24.1%.....	99

Figure 5.10 - Changes in balance measured Cd for the Configuration D at a ride height of 10.3% 100

Figure 5.11 - Base pressure contours for: a)baseline and b) blowing configuration D at $C_{\mu} = 0.013$ and $Re = 3.01 \times 10^6$ 102

Figure 5.12 - Balance and area weighted calculations of changes of C_d Configuration D at $Re = 3.01 \times 10^6$ 103

Figure 5.13 - Streamline plot in the wake of un-actuated baseline configuration at 10.3% ride height ... 104

Figure 5.14 - Streamline plot in the wake of un-actuated baseline configuration at 13.8% ride height ... 105

Figure 5.15 - Streamline plot in the wake of blown case at $C_{\mu}=0.012$ $h/H=10.34\%$; configuration B. 106

Figure 5.16 - Time averaged PIV image for unblown baseline configuration $h/H=10.3\%$, $Re = 3.01 \times 10^6$ showing vorticity 107

Figure 5.17 - Time averaged PIV image for downward blowing configuration D, $C_{\mu}=0.012$ $h/H=10.3\%$, $Re = 3.01 \times 10^6$ showing vorticity 107

Figure 5.18 - Vertical velocity components for baseline (a) and blown case (b)..... 109

Figure 5.19 - Aerodynamic Power savings available at different blowing system efficiencies 110

Figure 6.1 - Festo MHJ fast acting valves connected to custom PCB 115

Figure 6.2 - Model of Windsor model with jet angle adaptor located at roof trailing edge 115

Figure 6.3 - Section view of jet angle adaptor showing internal ducting 116

Figure 6.4 - View looking into rear of the Windsor model with the base panel removed 116

Figure 6.5 - Jet exit velocity profiles at different positions along an outlet section at 10 Hz actuation frequency 117

Figure 6.6 - Jet exit velocity profile at position 5 for an actuation frequency of 1Hz 118

Figure 6.7 - Pulsed jet orientations tested..... 119

Figure 6.8 – Images of wool tufts at slot exit for configuration D, for A) valve closed state B) valve closed state 119

Figure 6.9 - Change in drag coefficient vs actuation frequency for configuration B..... 121

Figure 6.10 - Change in drag coefficient vs actuation frequency for configuration C..... 122

Figure 6.11 - Change in drag coefficient vs actuation frequency for configuration D,E and F 123

Figure 6.12 - PIV vector fields with vorticity contours in the background for jet orientation B, with the jet running at $C_{\mu}= 0.0066$ as: A) steady blowing; B) Pulsed 10Hz actuation and C) Pulsed 25Hz actuation..... 125

Figure 6.13 - Example data set of positive vorticity with region of interest used for averaging shown in red..... 126

Figure 6.14 - Averaged vorticity within region of interest for configuration B..... 127

Figure 6.15 - PIV vector fields with vorticity contours in the background for jet orientation C, with the jet running at $C_{\mu}= 0.0066$ as: A) Pulsed 10 Hz actuation; B) Pulsed 15Hz actuation and C) Pulsed 25Hz actuation..... 129

Figure 6.16 - Averaged vorticity within region of interest for configuration C 130

Figure 6.17 - PIV vector fields with vorticity contours in the background for jet orientation D, with the jet running at $C_{\mu}= 0.0066$ as A) Baseline flow case, B) Pulsed 1Hz actuation and C) Pulsed 25Hz actuation..... 131

Figure 6.18 - Averaged vorticity within region of interest for configuration D 132

Figure 7.1 - Windsor model illustrating the position of slats 136

Figure 7.2 - Images showing vehicle under floor: A) standard rear floor section; B) Standard central floor section and C) Smoothed floor section viewed from rear of vehicle looking forwards 137

Figure 7.3- Full scale test vehicle shown in configuration 1 with pressure ‘spades’ attached to one half of the vehicle base surface..... 138

Figure 7.4 - Change in C_d from baseline vs configuration number 139

Figure 7.5 - Change in C_l from baseline..... 140

Figure 7.6 - C_p distribution on model base with no slats fitted (freestream velocity 40m/s) 141

Figure 7.7 - C_p distribution on model base with 4 slats fitted (freestream velocity 40m/s) 141

Figure 7.8 - Change in model base pressure relative to baseline configuration with 3 slats fitted (freestream velocity 40m/s)..... 142

Figure 7.9 - Change in model base pressure relative to baseline configuration with 4 slats fitted (freestream velocity 40m/s)..... 142

Figure 7.10 - Change in C_d vs configuration number 144

Figure 7.11 - Change in C_l vs configuration number..... 144

Figure 7.12 – Change in base pressure (C_p) with 6 slats applied 145

Chapter 1

INTRODUCTION

1.0 Introduction

A global drive to reduce CO₂ emissions is forcing vehicle manufacturers to use new technologies to meet ever increasing emissions targets. A great deal of the research is concentrated on refining vehicle powertrain systems and developing new ones. However large CO₂ emissions savings can also be realised by focusing on reducing a vehicle's tractive resistance. Reducing the tractive resistance reduces the power required from the powertrain to accelerate or move a vehicle. Figure 1.1 shows the forces produced by the different resistances to motion for an example production vehicle (Ford Escort) and highlights that a major contributor to tractive resistance is the aerodynamic drag, especially at motorway speeds.

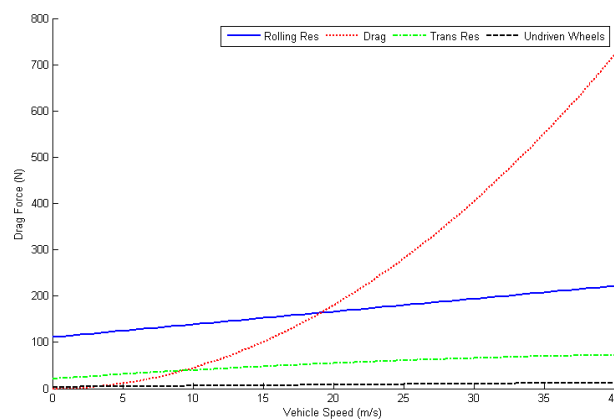


Figure 1.1 - Forces opposing the motion of a typical road vehicle (Ford Escort)

Since the oil crisis of the 1970's vehicle manufacturers have worked to reduce the coefficient of drag (C_d) of their vehicles, and with ongoing increasing cost of oil and the added awareness of climate change this work is set to continue. However, other considerations such as styling, passenger comfort, safety and loading space, mean that aerodynamic optimisation does not always take precedence in a vehicle's final shape. In order to further reduce C_d of road vehicles without impinging on these other requirements, new technologies must be investigated in an attempt to go further than traditional shape optimisation.

In the following sections the various sources and components that make up vehicle drag are discussed and the influence that drag force has on power demand is highlighted. Past, present and emerging technologies that provide a potential means of drag reduction are reviewed and assessed. Finally, the technologies that display the greatest potential for development are discussed further and developed for experimental investigation.

1.1 Tractive Resistance

From Equation 1.1 it can be seen that tractive resistance (F_{TR}) or the forces and resistances acting to oppose or slow a vehicles motion are made up of four main components in a standard front wheel drive vehicle.

- A) Tyre Forces
- B) Aerodynamic drag
- C) Transmission/Driven wheel resistances
- D) Undriven wheel resistances

$$\text{Equation 1.1} \quad F_{TR} = \underbrace{Mg(A_d + B_dV)}_A + \underbrace{(1/2 \rho AC_d V^2)}_B + \underbrace{(A_t + B_tV + C_tV^2)}_C + \underbrace{(A_{ud} + B_uV)}_D$$

Tyres with less rolling resistance and lower vehicle weights can both reduce the tractive resistance but because the aerodynamic drag force is proportional to V^2 it becomes the dominant term as vehicle speed increases. Figure 1.2 shows how the percentage contributions of the constituent parts of Equation 1.1 vary with vehicle speed for an example vehicle (Ford Escort), and that aerodynamic drag becomes the dominant term above 19m/s.

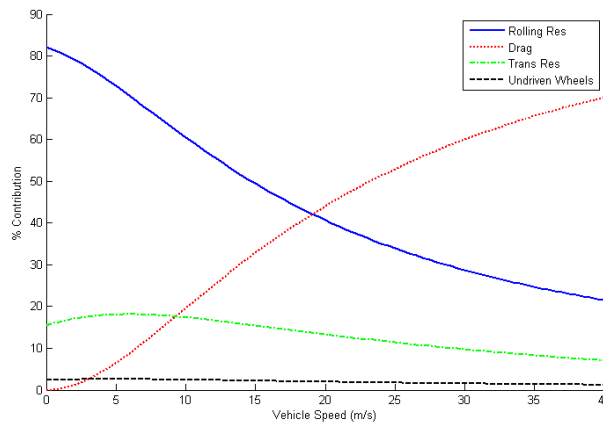


Figure 1.2 - Percentage contributions of resistive forces contributing to Equation 1 (Ford Escort)

If the aerodynamic force term is expressed as an ‘aerodynamic power’ (P_{AERO}) (Equation 1.2) supplied by the powertrain to overcome it, it is made apparent that a small reduction in the C_d of a vehicle can have significant influence on its power demands.

Equation 1.2
$$P_{AERO} = 1/2 \rho A C_d V^3$$

However, because aerodynamic power losses are also heavily dependent on vehicle speed their influence on a calculated measure of vehicle fuel consumption becomes dependent on the drive cycle used in the calculation. Some authors have suggested that if more realistic drive cycles were used (relative to the current European drive cycles used) in calculations of CO₂ contributions, it would show that the influence of aerodynamic drag power is even more prominent than currently believed (Schultz, 2010).

If engineers are to understand how C_d may be reduced it is important to understand what factors influence the development of aerodynamic drag acting on a vehicle, and in the following sections sources of drag for typical road car shapes will be investigated.

1.2 Sources of Drag

The aerodynamic drag force acting on a vehicle moving through air is a function of velocity (V), vehicle frontal area (A) and C_d (Equation 1.3). Frontal area is generally determined by vehicle class, component packaging, loading and ergonomic constraints, but has generally been increasing since the 1980's. C_d can be manipulated by an aerodynamicist, in the pursuit of lower drag forces, but it must be recognised that if frontal areas continue to increase any gains associated by lowering C_d will be negated.

Equation 1.3
$$F_{DRAG} = 1/2 \rho A C_d V^2$$

The resolved drag force along a vehicle body axis is the integration of the skin friction forces and the normal pressure drag forces. Skin friction drag forces are the longitudinal component of viscous forces created when air moves over the surfaces of a vehicle, and the pressure drag force is a result of the fact that generally the pressure over rearward facing surfaces of a vehicle will be lower than the forward facing ones. The pressure distribution around a vehicle body is influenced by a number of factors such as; small scale separations, 3D separations or vortex formation, and shape configurations that induce pressure gradients. In the case of a road vehicle skin friction drag is a relatively small contributor (~15% (Hucho, 1998) (Ahmed, Ramm and Falin, 1984)) to the overall drag force and therefore the pressure drag is comparatively large. For that reason the work of the road vehicle aerodynamicist will generally focus on creating a more favourable pressure distribution around the vehicle body.

Aerodynamic drag can also be broken down into its constituent parts in terms of its location of generation (Carr, Atkin and Sommerville, 1994); forebody, afterbody, underbody, wheel and wheel wells, protuberances, and engine cooling system. This breakdown was initially used to allow an estimation of C_d and although this is not a very reliable technique, it assists in approximating the relative contributions of each area to the total drag. In the current work it has been decided to focus on the flow around the afterbody of the vehicle because around 40-60% (depending on vehicle shape) of pressure drag is a result of the separations occurring in the afterbody area. Some of the main contributors to drag in the afterbody region are low base pressures, trailing vortex generation, and suction peaks on rearward facing surfaces.

1.2.1 Base Pressure and Vortex Drag

Base pressure drag is the result of low pressure flow in the wake of a vehicle generating low static pressures on the rear facing surfaces. The overall size of the wake and magnitude of pressure within it is largely determined by the vehicle shape, specifically the backlight configuration. The vehicle shape causes variations in the velocity field such as separations which result in a failure to recover pressure. Square back style vehicles suffer the most from high amounts of base pressure drag because the flow separates at its outer edges producing a wake almost as large as the frontal area of the vehicle. Fastback and notch back vehicles can generate a smaller wake if the flow remains attached to the rear screen panel before it separates, as can be seen from Figure 1.3.

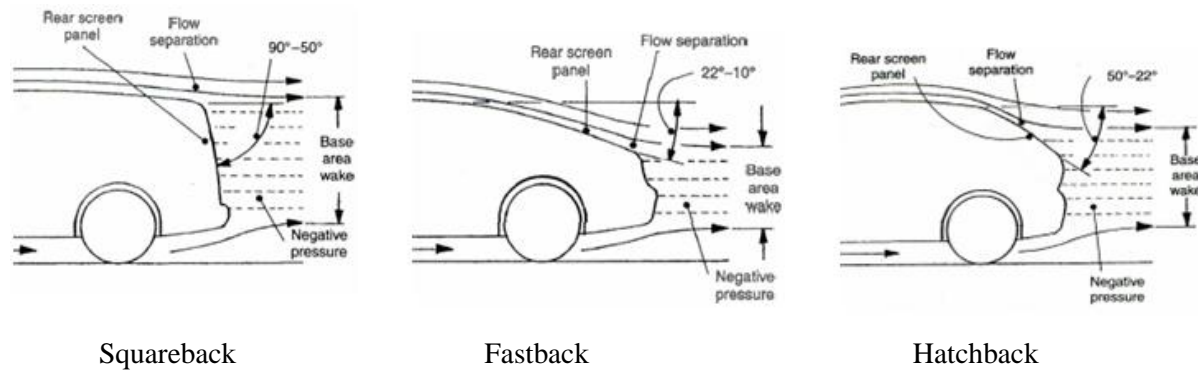


Figure 1.3 Wake sizes of different vehicle shapes (Heisler, 2002)

In order to generate the gains associated with an increase in base pressure by keeping the flow attached, the backlight angle must stay within a well known range of angles. Figure 1.4 illustrates the drag characteristics of various vehicle shapes with varying backlight angle relative to a squareback configuration.

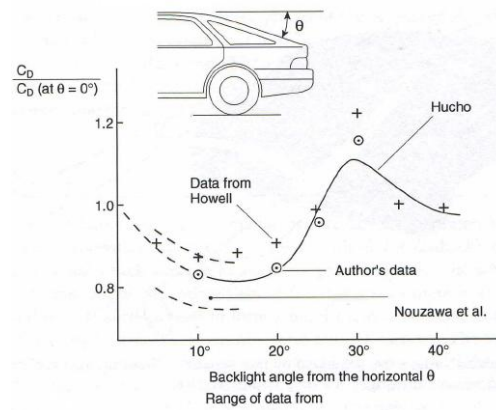


Figure 1.4 - Effect of backlight angle on C_d (Barnard, 1996)

The effect of backlight angle has been investigated by many authors such as Ahmed, Ramm and Faltn (1984), Howell, Sheppard and Blakemore (2003) and Keating, Shock and Chen (2008) and understanding of the mechanisms involved is improving but not complete, because the wake structure is very unsteady. As backlight angle increases from 0° to the optimum of around 12° , drag is reduced. Within this range of angles the flow stays attached to the rear screen panel and the reduction in drag is due to the reduced size of the vehicle base and wake and an increase in base pressure. However, as the angle increases further the gains from reduced base and wake size are counteracted by growing suction peaks on the C-pillar and rear screen panel, associated with the generation of trailing vortices along the C-pillar. Above $\theta \approx 20^\circ$ the vortices and suction peaks are sufficiently strong that the drag is worse than that of a squareback having a larger wake and base area. The highly 3D separations that develop into trailing vortices are very difficult to predict or model numerically. These structures make it very difficult for computational fluid dynamics (CFD) codes to generate accurate measures of their effect on drag or lift. In order to accurately predict the pressure distributions created by these vortical structures, CFD codes need to be able to predict the energy used up in the generation of these structures very accurately. This expenditure of energy, and the resulting pressure distributions created will obviously be seen as a source of drag, if they create suction peaks on rearward facing surfaces. The scale of which is discussed by Ahmed, Ramm and Faltn (1984), who artificially controlled the development of C-pillar vortices on a backlight angle of 30 degrees. When a splitter plate was placed behind the model to prevent the C-pillar vortex development, a C_d reduction of 0.118 was achieved.

Another feature of increasing backlight angle is the build up of a horse shoe vortex or separation bubble at the roof edge. Figure 1.5 show images from a CFD simulation of a simple Ahmed car model with increasing back angles. The results show isosurfaces of zero total pressure (an indication of separation and vortex location) which display how the horseshoe bubble develops.

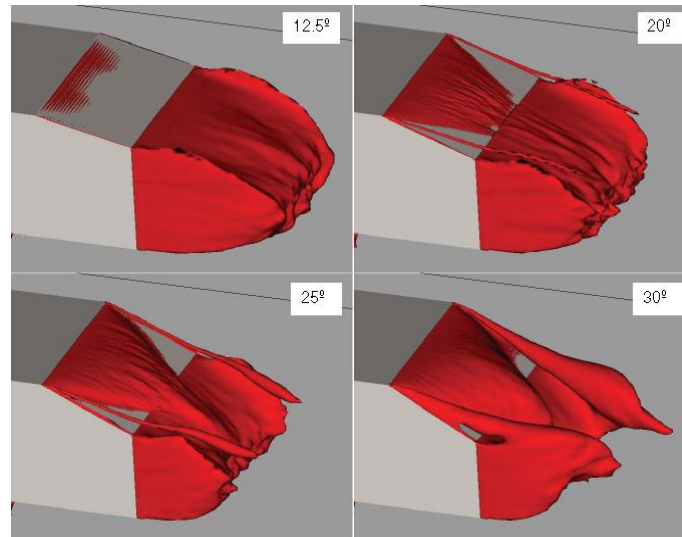


Figure 1.5 - Isosurfaces of zero total pressure on Ahmed car model for increasing back angle (Keating, Shock and Chen, 2008)

It is at $\theta \geq 30^\circ$ that this bubble bursts and the drag and flow structure resembles that of a squareback with separation occurring at the upper roof edge. Figure 1.6 from the original study (Ahmed, Ramm and Faltin, 1984) shows the sudden decrease in drag at 30° (known as the drag crisis) and is a more representative plot of the unsteady nature of the separations than the smooth characteristic shown in Figure 1.4.

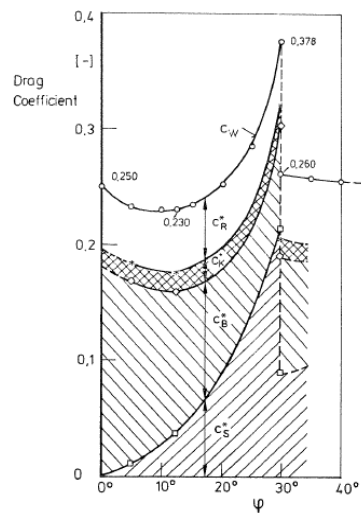


Figure 1.6 - Variation of drag with base slant angle (Ahmed, Ramm and Faltin, 1984)

It is clear from this plot that care must be taken when designing the afterbody of a car to get the best combination of reduced wake size, whilst limiting vortex generation and suction peaks.

1.2.2 Rear edge conditioning

Another technique used to try and reduce the wake area and increase the base pressure is address the shape the rear separating edge to turn the flow in a desired way. If a radiused rear edge is used instead of a sharp one, the magnitude and orientation of the radius can create positive or negative effects, depending on the implementation

Although no plot for drag vs increasing rear edge radius has been found in previous automotive aerodynamics work, previous publications such as Kee, Kim and Lee (2001) suggest that the variation of C_d with increasing radius would be of a similar shape to Figure 1.6. As edge radius increases from zero, C_d is expected to decrease to a minimum value at an optimum radius before rising to a worst case value as suction around the radius increases and vortex strength increases. Whether or not a sudden ‘drag crisis’ would occur is unknown. Figure 1.7 illustrates the reasoning for potential increases in drag using large rear radius.

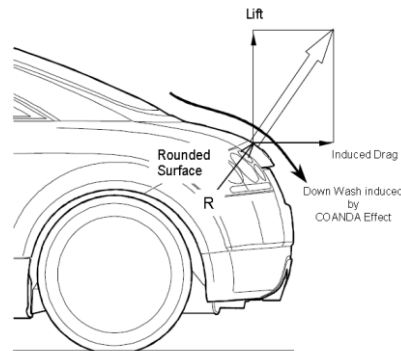


Figure 1.7 - Drag due to large trailing radii (Kee, Kim and Lee, 2001)

As the rear edge radius increases the suction peak shown in Figure 1.7 also increases, adding to the induced drag component force. Additionally this shape creates a downwash of fluid which will add to the rotational strength of the trailing vortices on the C-pillar. In a similar way to the effects found in increasing backlight angle the build up of these two mechanisms will outweigh any potential gains from a reduced wake and base area. The addition of a rear spoiler to force the flow to separate will therefore reduce drag. This addition effectively induces a ‘drag crisis’ region of the drag vs radii curve. This approach also reduces the unsteady forces felt by the vehicle that would otherwise be created as a result of the rear separation point location being transient. An example of this technique employed on a road vehicle can be seen on the Audi A2 (Figure 1.8), where a lip spoiler is placed around $\frac{3}{4}H$ on rear of the vehicle to induce separation.



Figure 1.8 - Audi A2 rear spoiler configuration

1.2.3 Drag Reduction Techniques

From the previous section the aims for reducing drag contributions of the afterbody section of a vehicle can be summarised below:

- Reduced wake and base size giving rise to increased static pressures on rearward facing surfaces
- Prevent the build up of trailing vortices whilst maintaining attachment of any rear slant flow
- Prevent the occurrence of suction peaks on rearward surfaces

Detail optimisation, and vehicle shape evolution have played a part in working towards these goals, however an increasing number of investigations are being carried out into more novel passive and active technologies to yield further gains.

1.3 Drag Reduction Techniques; Passive

1.3.1 Diffusers

Jowsey (2008) and Cooper et al. (1998) conducted studies on the performance of underbody diffusers for drag and downforce production, both found that the performance is sensitive to ride height and diffuser configuration. These studies suggest single channel underbody diffusers can offer drag reductions at high ride heights and low diffuser angles, as can be seen from Figure 1.9 and Figure 1.10. At lower ride heights and higher diffuser angles ground effect and increased trailing vortex strength increase downforce production, with the penalty of increased drag.

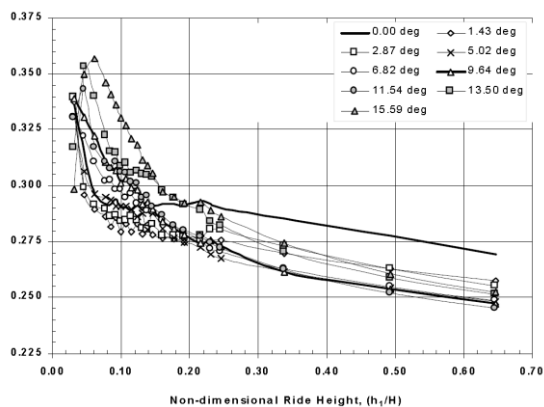


Figure 1.9 – Drag produced by an underbody diffuser at various angles and ride heights (Cooper et al., 1998)

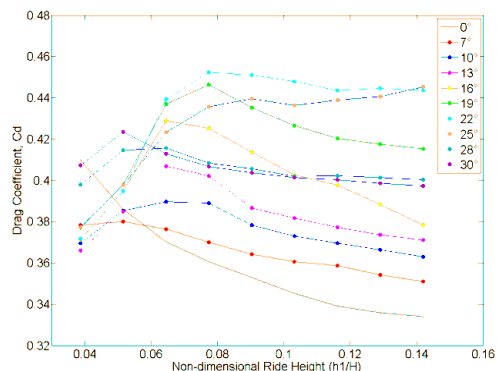


Figure 1.10 - Drag produced by an underbody diffuser at various angles and ride heights (Jowsey, 2008)

Figure 1.10 does not show tests on ride heights as high as Figure 1.9, however it is worthy of note that the ride heights above $0.2h/H$ are unlikely to be found on any road vehicles. It should also be highlighted that these configurations were tested on a fixed ground which may require a translation of the curves in the y-axis if they are to be compared to a moving belt setup.

1.3.2 Boat Tailing

One of the oldest methods for reducing the size of a vehicles wake is known as boat tailing and would prove most effective on squareback cars or lorries. In the process of boat tailing a bluff body or road vehicle such as in Lanser and Ross (1991), Peterson (1981), Khalighi, Zhang and Koromilas (2001) and Verzicco et al. (2002), the rear of the vehicle is modified as in Figure 1.11 and Figure 1.12 to allow the flow to stay attached and so reduce size of the wake and the base pressure deficit. Wong and Mair (1983) also showed that a ‘shortened boat tail’ such as in Figure 1.12 could be just as effective as a ‘fully streamlined’ one in reducing drag.

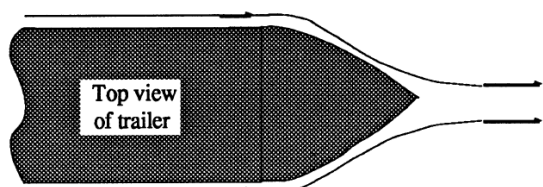


Figure 1.11 - fully streamlined rigid boat tail (Lanser and Ross, 1991)



Figure 1.12 - Shortened rigid boat tail fairing (Wong and Mair, 1983)

Boat tailing takes its methodology from the basics of streamlining however the physical sizes and shapes involved are the main limiting factor and are either impractical or even dangerous. In an effort

to gain a boat tailing effect using a more practical configuration research has been conducted into so called ‘truncated boat tail’ configurations by Lanser and Ross (1991), Khalighi, Zhang and Koromilas (2001) and Verzicco et al. (2002) using extension plates(Figure 1.13).

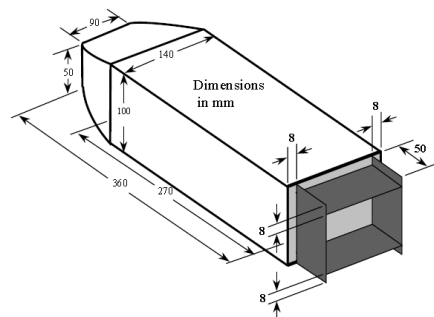


Figure 1.13 - Boat tailing using extension plates (Khalighi, Zhang and Koromilas, 2001)

The flow mechanisms involved with this latter approach are different from traditional rigid boat tailing. When compared to the flow over the rear edge of a standard bluff body it can be seen that a separation bubble is formed between the rear face of the body and the edge of the plates (Figure 1.14). This bubble entrains the flow towards the centre of the wake, in some cases the flow will re-attach itself to the rear edge of the plates before separating again into the wake flow. Although the extension plates do not reduce the overall length of the wake they do reduce its width and height. It has also been observed that the air inside the cavity formed by the plates is almost quiescent, so the mean base pressure on the rear surface of the model is higher compared to the standard bluff body. This is thought to be because the fluctuating part of the wake has been shifted downstream and so the unsteady pressure field in the wake acts on the open surface of the cavity as opposed the rear face of the body.

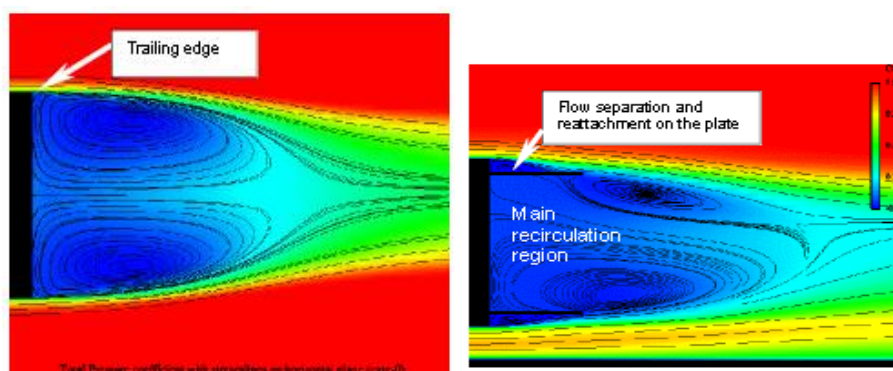


Figure 1.14 - Pressure coefficient at rear of bluff body left: standard setup right: with extension plates (Khalighi, Zhang and Koromilas, 2001)

This setup is still an unlikely addition to any road vehicle because of its physical size, and appearance. However a commercialised form has recently been used in the USA (TrailerTail, 2007). The product can only be used in the USA currently because of laws restricting the length of additions to the rear of

road vehicles in other parts of the world such as Europe. The current product is only applicable to large haulage trailers but claims 6.6% fuel savings were achieved in SAE Type 2 fuel efficiency tests.

1.3.3 Flaps and Plates

Experiments conducted by Bearman (1965) used a single splitter plate of various lengths applied to the base of a two dimensional bluff body, as shown in Figure 1.15.

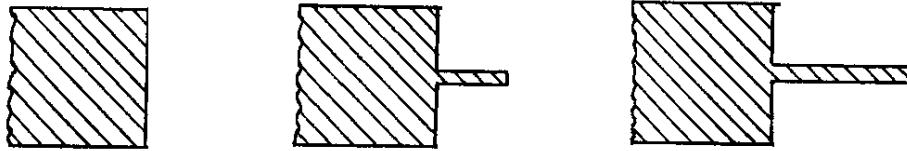


Figure 1.15 - 2D bluff body incorporating splitter plates of various lengths (Bearman, 1965)

The splitter plate inhibited the interaction of upper and lower vortex structures meaning that large coherent vortex structures were not formed until further downstream in the wake. Although in this case the wake length and overall size was increased the base pressure was increased using the splitter plates because the vortex structures could not interact with the base and create low pressures. Figure 1.16 shows a spanwise base pressure distribution for the model with and without splitter plates and clearly shows regions of increased base pressure where vortex-base surface interaction was suppressed.

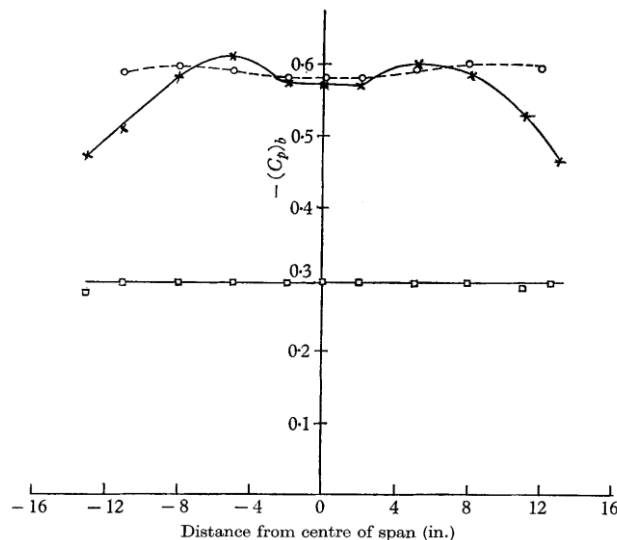


Figure 1.16 - Spanwise base pressure distribution. x = without splitter plate and end plates, o = without splitter plates but with end plates, □ = with splitter plate but without end plates (Bearman, 1965)

Kowata et al. (2008) conducted studies on a simplified car model with an underbody slant similar to a diffuser setup, but with the addition of flaps (Figure 1.17). It was found that while a drag reduction could be found from the underbody slant alone at low angles, the gains could be increased by adding flaps to inhibit the development and shedding of trailing vortices into the wake. Although PSD plots of hot wire measurements taken in the wake show that the flaps suppressed the trailing vortices, it could also be argued that some of the gains arose from creating a rear cavity, as was found by Howell, Sheppard and Blakemore (2003).

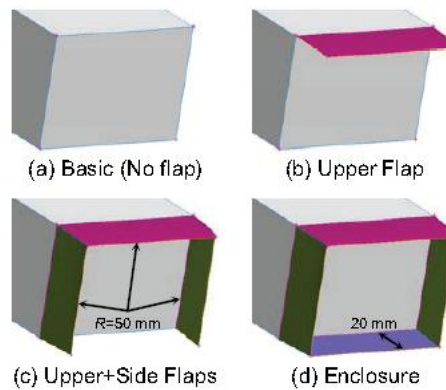


Figure 1.17 - Rear Flap configuration for drag reduction (Kowata et al., 2008)

Beaudoin and Aider (2008) used the addition of flaps to an Ahmed car model with 30 degree back angle, as shown in Figure 1.18 to control the flow at the rear of the body.

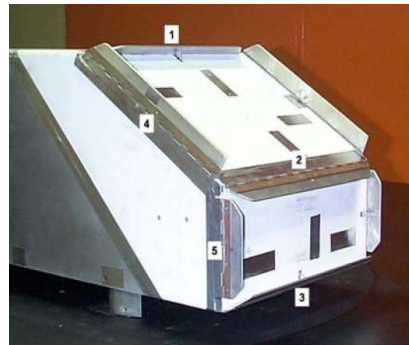


Figure 1.18 - Flaps model (Beaudoin and Aider, 2008)

They discovered that the most effective combination of flaps (1 plus 4 as seen in Figure 1.18) could reduce drag by up to 25%. A reduction in drag of this magnitude corresponds to, if not exceeds, the drag reduction associated with reducing the back angle from 30 degrees to the optimum of around 12 degrees. It is suggested that the bulk of the reduction is due to a suppression of the trailing vortices on the C-pillar whilst also using flap 1 to control the separation of flow over the rear slant. Figure 1.19 illustrates this using plots of the cross stream velocity field 129mm downstream of the model, for a model with flaps and a model without. The test velocity was 40m/s.

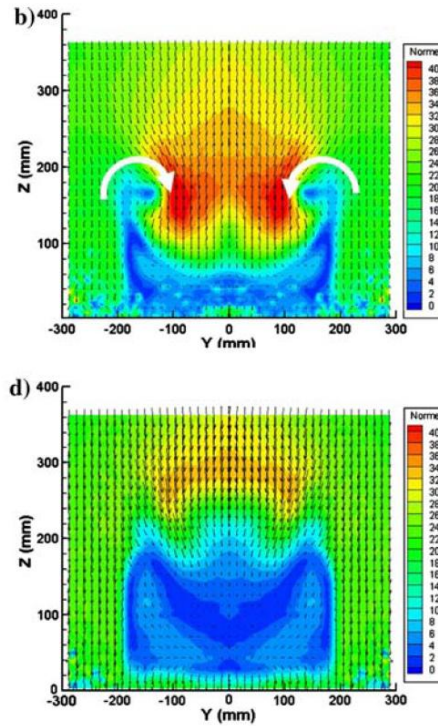


Figure 1.19 - PIV vortex reduction (Beaudoin and Aider, 2008)

From these results it may be possible to create additional gains in drag reduction beyond the optimum back angle of 12 degrees using flaps in combination with other slant angles.

All the methods discussed seem to offer substantial drag reduction possibilities, however with the exception of an underbody diffuser the physical addition of large flaps or truncated boat tails would not be acceptable on most road vehicles. For this reason work is being carried out to find a discrete non intrusive system that can generate the same recoveries in base pressure, or suppression of vortex formation without the need for bulky or unacceptable styling additions to a vehicle.

1.4 Drag Reduction Techniques; Active

1.4.1 Moving Surface Boundary Layer Control (MSBC)

MSBC involves the use of a moving surface, usually a rotating cylinder to inject momentum to a fluid flow. The concept was originally used on flat plates, and 2D stalled aerofoils to delay the separation of the boundary layer (Modi, 1997), however work has also been carried out on truck and trailer models. In this application a rotating tube can be used to inject momentum and turn the separating flow on the rear surfaces of a squareback configuration, downwards into the wake. Figure 1.20 shows a flow visualisation image of the technique being used on separated flow over a bluff body, where the wake size is dramatically reduced. It is conjectured that the use of this turning technique would assist

in a global increase in overall base pressure of a vehicle. Using a splined roller at the front and rear of the trailer Modi and Ying (1990) claim a drag saving of up to 26%

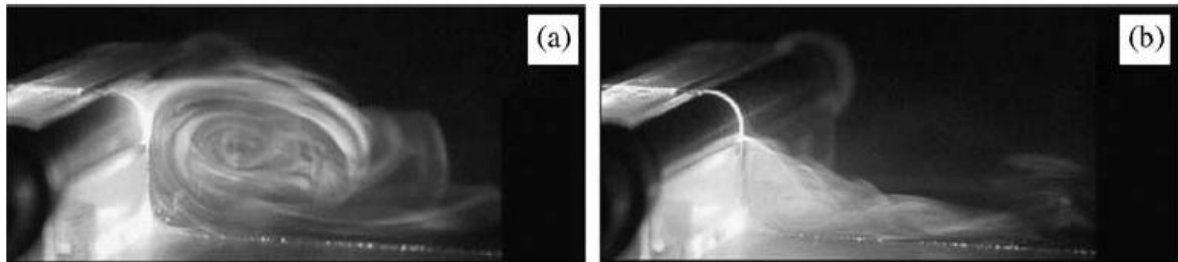


Figure 1.20 – Moving surface boundary layer control on a bluff body (Roumeas, 2006)

1.4.2 Continuous Suction

Roumeas (2006) investigated the effect of constant suction placed at various positions on the rear of an Ahmed car model with backlight inclination of 25° . It was found that the most effective position was at the roof/windscreen junction, where a constant suction velocity of $0.6U_\infty$ gave a drag reduction of 17%. The process of applying constant suction is said to deflect the naturally separated flow downwards and force it to remain attached to the rear screen panel, as shown in Figure 1.21. However most of the studies were CFD based and it is questionable how well the CFD could simulate the effects of increased C-pillar vortex strength. By applying suction to retain an attached flow on the backlight it is anticipated that C-pillar vortex strength would increase, and the balance of gains achieved through reduced wake size against the negative effect of increased C-pillar vortex strength should be quantified experimentally.

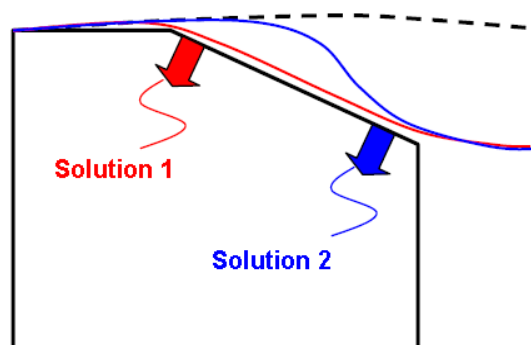


Figure 1.21 - Effect of continuous suction on Ahmed car (Roumeas, 2006)

1.4.3 Continuous Blowing

Continuous blowing techniques use a continuous jet of air as either a momentum injection or a deflector of the flow. The combination of continuous blowing and Coanda effect was used by Englar

(1987) originally as a means of producing high lift wings for Short Take Off and Landing (STOL) aircraft. The technique employed a continuous jet of air to entrain flow around a radius at the rear of a wing as shown in Figure 1.22.

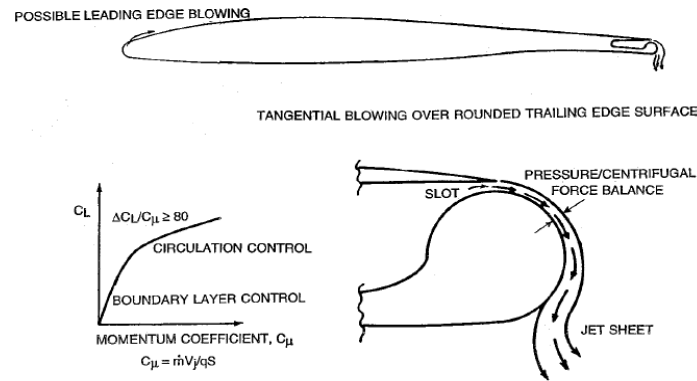


Figure 1.22 - Blowing technique on a wing (Englar, 2003)

The technique was then applied in the form of an additional radius applied to the rear edges of a truck trailer, with the aim of improving the base pressure distribution (Englar, 2003) (Englar, 2005). The specific radii used on each surface was investigated through a number of iterative tests on a scale model in a wind tunnel. During the tunnel tests drag reductions of up to 50% percent were recorded and an ambitious claim of up to 32% reduction in horsepower requirements was quoted for a full scale vehicle. The technique was then tested at full scale using SAE Type II fuel economy runs. The improvement in fuel efficiency over a standard vehicle was 4-6%, which was considerably less than predicted but still represents a valuable improvement. Englar suggested that Reynolds number effects could be a reason for the discrepancy, and concluded that the discrepancy should be investigated further.

Geropp and Odentha (2000) also tried to use a blowing and Coanda control technique in the same way as Englar on a 2D simplified car model. The tests conducted were very Reynolds number sensitive, and any drag reductions were lost with increasing Reynolds number. In this case the rear radii used actually increased the pressure drag and any net drag reduction found at low Reynolds numbers is attributed to the thrust imposed by the jets.

When relying on a Coanda effect the need to implement a large trailing edge radius means that whenever the jet is not blowing there is a net drag gain associated with the large suction peaks that will be created on the trailing edge radius. Modern road vehicle aerodynamicists usually strive to avoid large trailing edge radii for exactly this reason and the barriers to incorporation for a technology of this type may be significant.

Rouméas, Gilliéron and Kourta (2006) conducted a CFD investigation into the use of continuous blowing on a squareback bluff body. A combination of rectangular jets, operating at various angles were positioned on the rear face of the model as shown in Figure 1.23. In this investigation the rear trailing edges were left sharp creating a clean separation position.

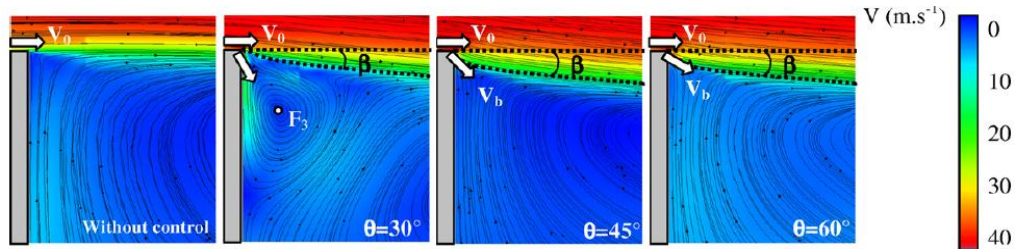


Figure 1.23 – Continuous blowing at various angles into the wake of a bluff body (Rouméas, Gilliéron and Kourta, 2006)

The optimum configuration was a jet angled at 45° which deflected the freestream high momentum flow downwards into the wake. It is claimed that drag reductions of up to 29% were achieved, however a jet velocity of $1.5U_\infty$ was required, and the source for this energy injection is not identified.

Howell, Sheppard and Blakemore (2003) investigated the use of continuous blowing in the form of base bleed, again in an attempt to increase the base pressure, however the gains found as a consequence of the bled air were negligible. The work actually served to highlight the benefits of a rear cavity in the effort to increase base pressure.

One of the main issues with blowing and suction techniques is that the power to create the suction or blowing velocities required can be high. Some authors suggest the use of cooling air flow, or compressed air from a turbo already available on a vehicle. However, this would require ducting of the fluid to the required area, and generates losses within the ducting and packaging difficulties. A good compromise might be to locally duct air close to the point of jet application, but the mechanisms that create the drag change would still need to be validated. Currently the study by Rouméas, Gilliéron and Kourta (2006) is only a CFD study and has not been experimentally validated.

A relatively new technology that requires no ducting and is a zero net mass flux device is a Synthetic Jet (SJ). If the momentum required to influence flow could be generated using this technique it may offer an attractive solution to the problem of ducting.

1.4.4 Synthetic Jet Actuators

A Synthetic Jet is a micro-actuator consisting of a cavity having three solid boundaries, one containing an orifice, and an oscillating diaphragm which momentarily ejects and ingests fluid across the orifice such that the net mass flux in one phase of operation is zero (see Figure 1.24).

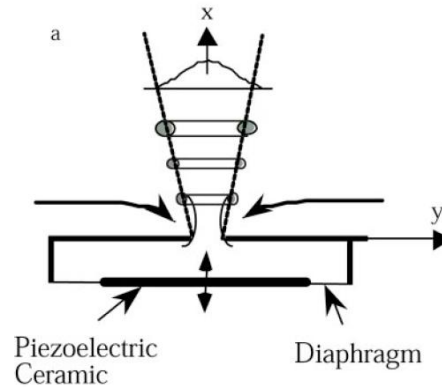


Figure 1.24 - Synthetic Jet Illustration (Glezer and Amitay, 2002)

A unique feature of the synthetic jet when compared to a continuous or pulsed jet, is that it is formed entirely from the working fluid of the flow system, so no net mass is injected across the flow boundary. Synthetic jets can be formed over a broad range of length and timescales, and when this is coupled with some of their unique attributes in terms of interaction with a flow field, they become an attractive mechanism for fluid flow control.

Synthetic jet actuators have been studied in a variety of systems and flow control applications, and the mechanisms with which they are said to influence flows can vary widely. For the purposes of drag reduction on road vehicles the field of synthetic jet flow control shows promise but could easily encompass a vast area of study. Some of the methods used to control flow using a synthetic jet are discussed below.

1.4.4.1 Separation Control

It is well known that laminar flow around a 2D cylinder will separate at an azimuthal position of $\theta \approx 90^\circ$ whereas turbulent flow separation will be delayed until $\theta \approx 110^\circ$. In the case where flow is laminar it is of benefit to 'trip' the flow to become turbulent because the resistance to separation is higher, allowing the flow to remain attached for longer and reduce the size of the wake produced. Glezer, Amitay and Honahan (2005) used a synthetic jet actuator installed at an azimuthal position of $\theta = 60^\circ$ on a 2D cylinder placed in laminar flow conditions. When the synthetic jets were driven at the frequency associated with the natural vortex shedding of the cylinder they could delay separation until $\theta \approx 110^\circ$. When the synthetic jet actuator frequency was increased the flow separation was delayed until $\theta \approx 135^\circ$, as can be seen from Figure 1.25. It was concluded that when the actuation frequency is

nominally of the same order as the natural shedding frequency (or up to five times magnitude) the performance of the actuator in influencing the point of separation increases with increasing actuation frequency. At actuation frequencies above five times the natural shedding frequency, performance becomes invariant with actuation frequency. Unfortunately in road vehicle applications the flow is usually turbulent and any gains found in laminar flow may be lost when introduced in a turbulent flow.

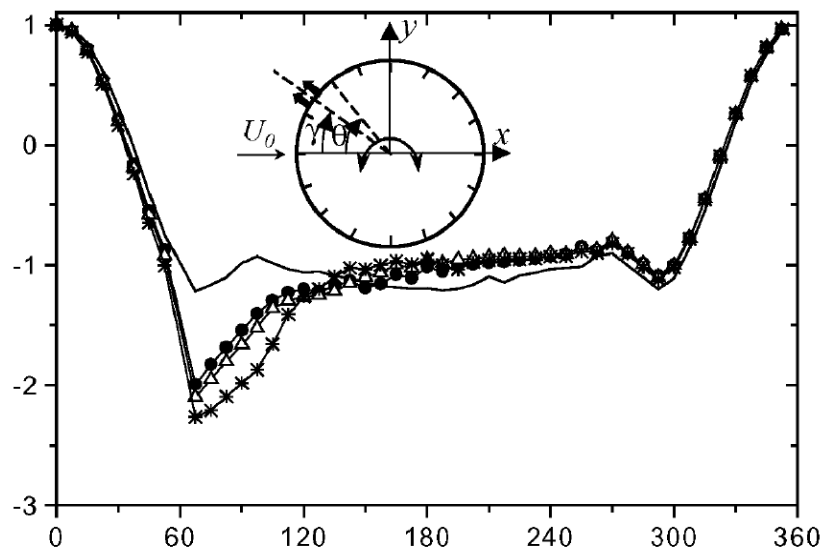


Figure 1.25 - Variation of the pressure coefficient around a tube with increasing dimensionless actuation frequency $SrD_{act} = \bullet; 0.24, \Delta; 0.50, *; 0.83$ and $-$; base line flow (Glezer, Amitay and Honahan, 2005)

Glezer, Amitay and Honahan (2005) and Béra et al. (2000) investigated this effect using conventional trip wires on the front of the cylinder to create a turbulent boundary layer. The synthetic jet was oriented at an azimuthal position of 110° relative to the freestream direction. Pressure distributions around the tube studied by Glezer, Amitay and Honahan (2005) (Figure 1.26) and by Béra et al. (2000) (Figure 1.27) are shown below.

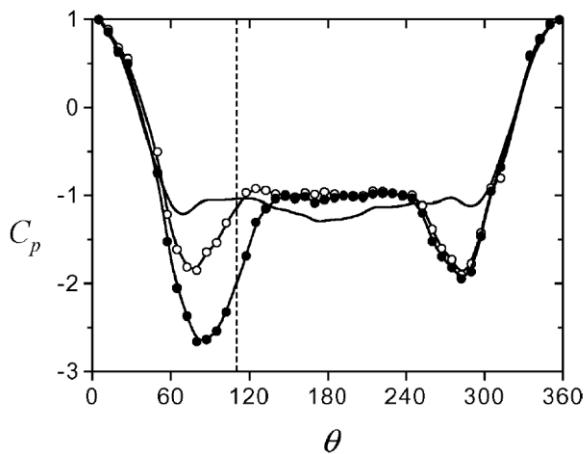


Figure 1.26 - Pressure distribution around 2D cylinder: \square unactuated with laminar BL, \circ unactuated with tripped turbulent BL, \bullet actuated with tripped turbulent BL (Glezer, Amitay and Honahan, 2005)

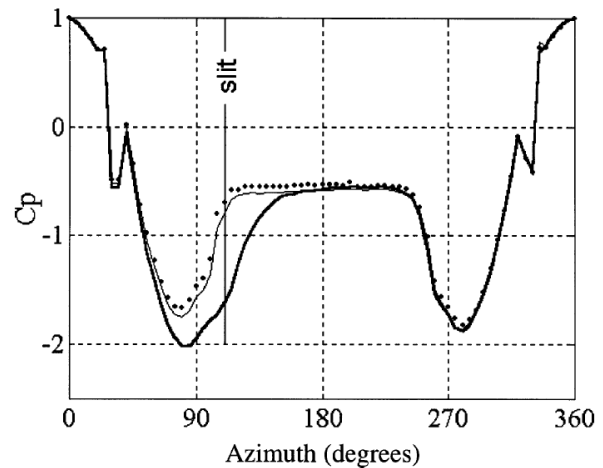


Figure 1.27 - Pressure distribution around 2D cylinder: \bullet unactuated, tripped turbulent BL, \square (thin) low level actuation, tripped turbulent BL, \square (thick) high level actuation, tripped turbulent BL (Béra et al., 2000)

Figure 1.26 illustrates how the point of separation will shift from $\theta \approx 90^\circ$ in a laminar boundary layer to $\theta \approx 110^\circ - 120^\circ$ in a turbulent boundary layer. When a synthetic jet is employed at $\theta \approx 110^\circ$ a further suppression of the separation point can be observed, as far as $\theta \approx 135^\circ$ confirming that the synthetic jet can also influence the flow when a turbulent boundary layer is present.

Figure 1.27 shows a similar plot but compares the effects of low and high levels of actuation (slot exit velocities of 22m/s and 42m/s respectively). Using low level actuation the width and depth of the suction peak, just before the point of separation slightly increases relative to the unactuated flow, but the point of separation is relatively unchanged. Using high levels of actuation the separation point is shifted toward the rear of the cylinder to around $\theta \approx 135^\circ$, correlating with Figure 1.26, but illustrating the sensitivity to different levels of actuation, or momentum coefficient (C_{μ}) as defined in Equation 4.3.

1.4.4.2 Active Vortex Generator

Vortex generators work by creating a vortex which imparts rotation into the flow. This rotation then entrains high momentum freestream fluid towards the areas required; usually low momentum boundary layers or wake regions. A vortex generator can be a physical addition to the structure however in the current discussion synthetic jets are used to actively generate vorticity. Glezer, Amitay and Honahan (2005) suggest a similar mechanism is what accounts for the delay in separation around

the cylinder in Figure 1.25 to an azimuthal position of $\theta \approx 135^\circ$. Béra et al. (2000) studied the flow around a 2D cylinder in turbulent flow and found that with a synthetic jet located at $\theta \approx 110^\circ$ they could also delay the separation point until further around the tube. The rotation imposed on the flow to deflect it can be seen in Figure 1.28 which displays instantaneous velocity vectors and rotational intensity for the actuated flow case. This plot shows areas of high intensity rotation moving around the surface of the tube at a characteristic shedding wavelength. At these points of high rotational intensity the velocity vectors show the freestream fluid being drawn down towards the tube surface, serving to delay separation.

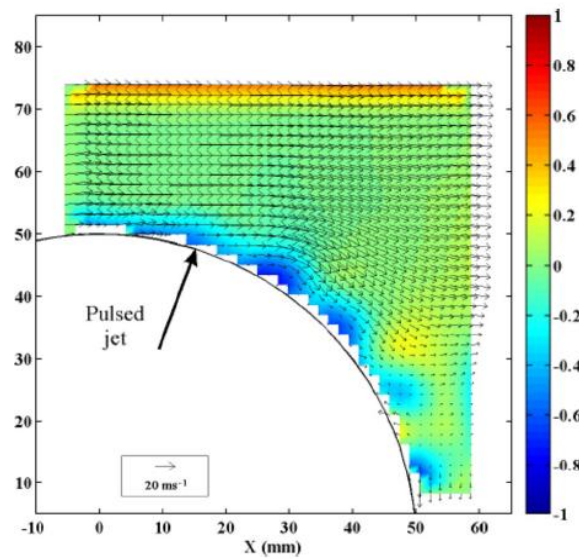


Figure 1.28 – Velocity vectors and rotational intensity (Béra et al., 2000)

Glezer, Amitay and Honahan (2005) also used this principle on the suction side of a stalled aerofoil to deflect flow downwards and partially reattach the wake to the top surface of the wing to increase lift. It is shown that there is a spike in performance when the actuation frequency of the jet is matched to the characteristic vortex shedding frequency, which is dependent on the characteristic scale of the wake. This scenario corresponds to an actuation Strouhal number as defined in Equation 1.4, where L_{advec} and U_c are the characteristic advection length and speed respectively.

Equation 1.4

$$St_{act} = \frac{L_{advec}/U_c}{T}$$

Brunn and Nitsche (2006) used a synthetic jet on an overcritical 2D diffuser setup in a wind tunnel as shown in Figure 1.29. In this case Strouhal number was based on the characteristic diffuser height H . The effect of matching the actuation with the typical vortex shedding frequencies and with the shear layer instabilities was investigated.

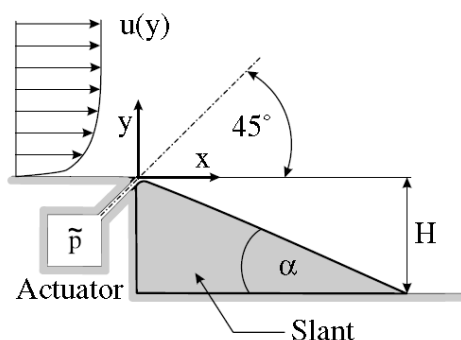


Figure 1.29 - 2D diffuser (Brunn and Nitsche, 2006)

The greatest receptivity in the wake to excitation occurred using Strouhal numbers associated with vortex shedding frequencies, far less receptivity was seen when Strouhal numbers associated with shear layer instabilities were used. This effect was also demonstrated on a 2D Ahmed car model used in a water tunnel, where excitation at vortex shedding frequencies reduced the height and halved the length of the wake.

Leclerc and Levallois (2006) also conducted a 2D study on a simplified Ahmed car model using CFD simulation as in Figure 1.30. It was found that an actuator reduced frequency of $0.7F^+$ based on model height H gave the best results in terms of increasing the base pressure on the model. If the physical dimension used in the calculation of the Strouhal number is assumed to be the factor that drives the shedding frequency it may be questioned why the best results were not obtained at $F^+=1$. However further observation of the model suggests that the characteristic length used should have been the base height as opposed to the model height, as the base height is equal to $0.7H$. Figure 1.31 illustrates that there was a narrow band of receptivity to actuation, where the drag reduction potential is at its greatest. This narrow band of receptivity suggests that care must be taken when defining a reference dimension, as this dimension will inevitably determine the actuation frequency used in the search for optimum receptivity to actuation. Alternatively a wake study must be conducted to identify any characteristic shedding frequencies that may be present.

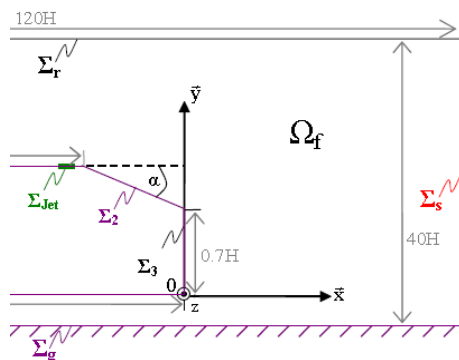


Figure 1.30 - Model configuration (Leclerc and Levallois, 2006)

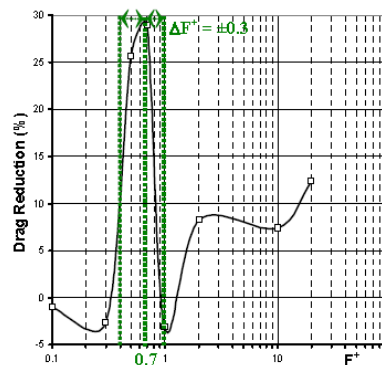


Figure 1.31 - C_d vs reduced actuator frequency F^+ (Leclerc and Levallois, 2006)

1.4.4.3 Vortex Suppressor

In contrast to the approach of generating vortices Pastoor et al. (2008) used synthetic jets controlled in a closed loop, linked to base pressure transducers to suppress the formation and interaction of vortices. Figure 1.32 shows the D shaped two dimensional bluff body that was used in the experiments. In the unactuated case vortices would be shed from the upper and lower surface 180° out of phase and the two vortices would interact to build up vortex strength in the near wake.

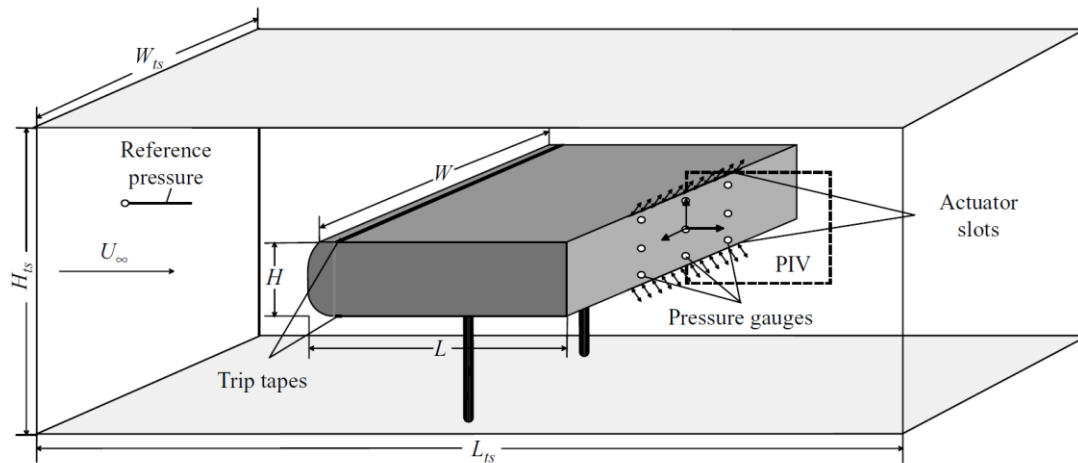


Figure 1.32 - D-Shaped body used in vortex suppression experiments (Pastoor et al., 2008)

Figure 1.33 shows an instantaneous wake flow field, with upper and lower vortices A and B 180° out of phase and interacting with one another. Figure 1.33 also shows the low pressure region that is created on the base by the large vortex B when it is shed and interacts very closely with the base surface.

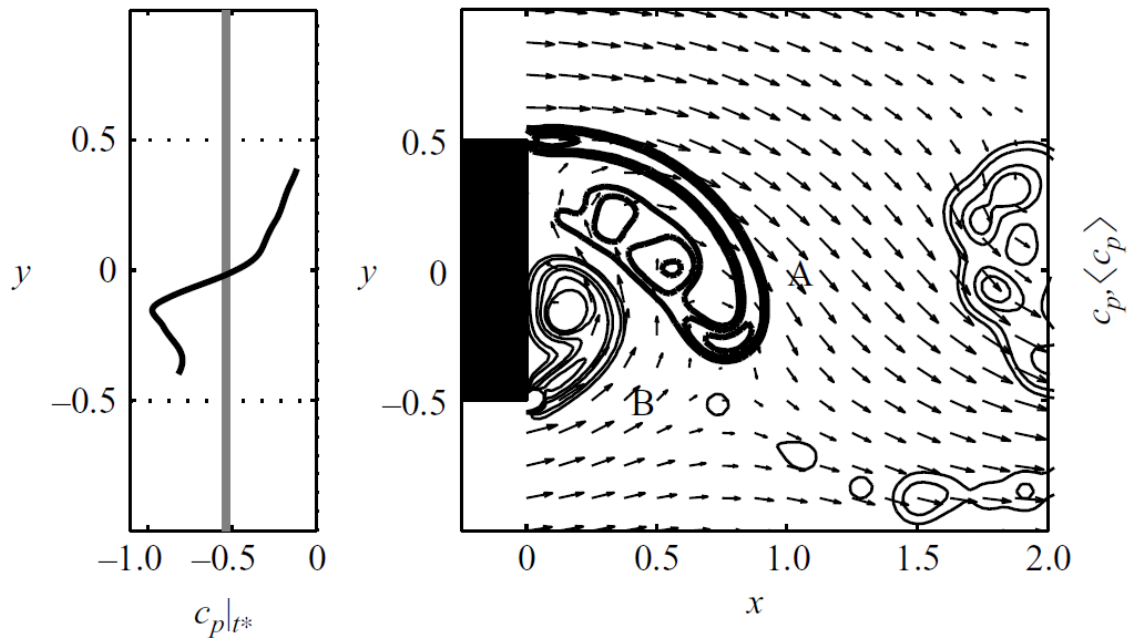


Figure 1.33 – Instantaneous pressure distribution and wake flow distribution behind a D shaped bluff body, without control (Pastoor et al., 2008)

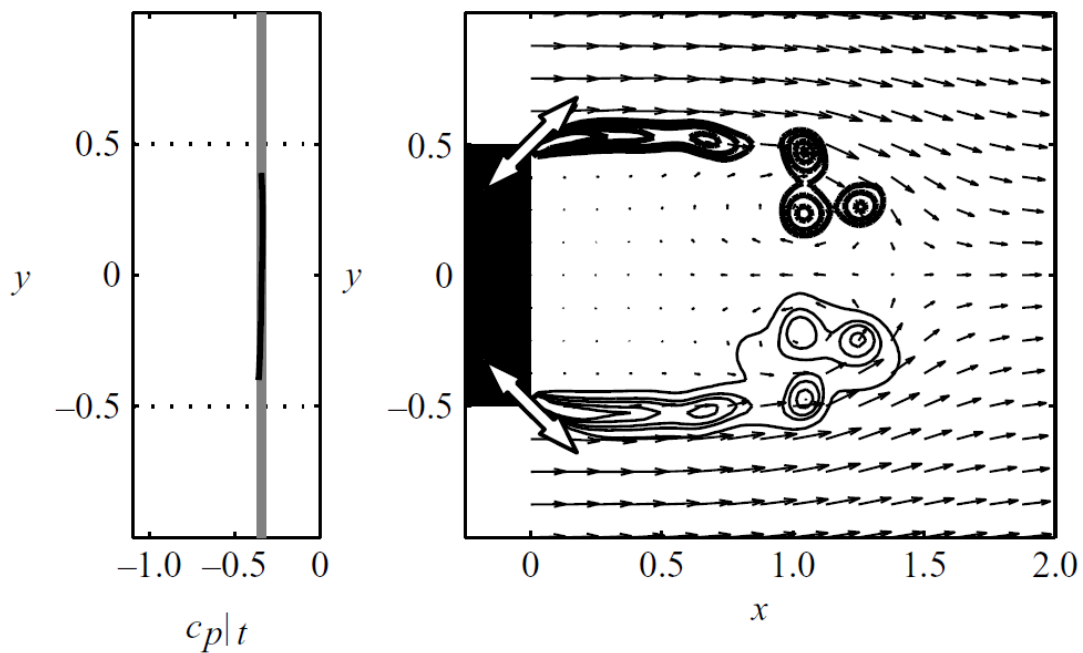


Figure 1.34 - Instantaneous pressure distribution and wake flow distribution behind a D shaped bluff body, controlled by SJ actuators (Pastoor et al., 2008)

In the SJ controlled case (Figure 1.34) the synthetic jet actuators were timed to ensure a vortex was shed from the upper and lower separating edges at the same time. This prevented the vortices from interacting and building up vorticity very close to the base surface. This approach elongates the wake

but increases base pressure by inhibiting the build up of vorticity until further downstream. The technique is closely linked to that of Bearman (1965) using splitter plates as shown in Figure 1.15.

1.4.4.4 Virtual Shape Change

In the work conducted on a stalled aerofoil, Amitay and Glezer (2002) carried out investigations into the effects of actuation frequencies over an order of magnitude higher than typical vortex shedding frequencies. Actuation at much higher frequencies not only produced complete reattachment of the upper wake from the stalled wing, but it significantly reduced fluctuating force components associated with the shedding process. Figure 1.35 shows time averaged velocity vector plots for the baseline flow, actuation at $St=0.95$ and actuation at $St=10$.

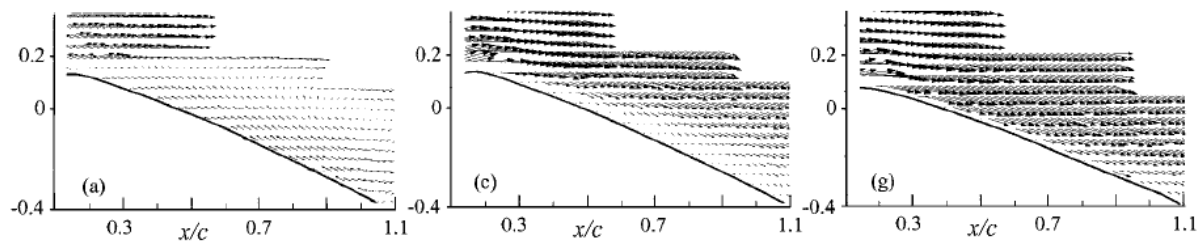


Figure 1.35 – Velocity vector plots at different actuator frequency F^+ (Amitay and Glezer, 2002)

It was hypothesised that a jet actuated at high enough frequencies will form a re-circulating region of flow or a bubble that is time independent of the surrounding flow field. This bubble would divert streamlines around it in effect creating a virtual shape change.

The virtual shape change mechanism was investigated by Mittal and Rampunggoon (2002) in numerical simulations of a synthetic jet influencing laminar boundary layer cross-stream flow over a flat plate. The simulations showed that when mean jet exit velocities were large relative to the freestream velocities, a large recirculation bubble was formed diverting the streamlines of the freestream flow around the bubble, as shown in Figure 1.36. However when jet exit velocities were low the bubble size shrank and may not even form at all. Results were presented that showed an almost linear scaling of the overall bubble length with jet momentum coefficient, (see Equation 4.3) indicating the importance of momentum flux available from the jet orifice.

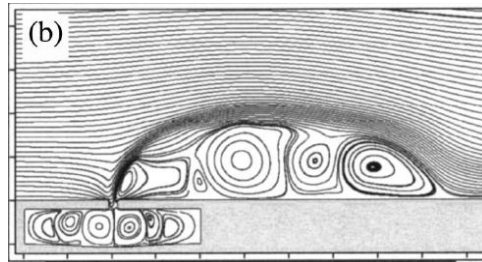


Figure 1.36 - Recirculation bubble and shape change effect of a synthetic jet (Mittal and Rampungoon, 2002)

1.4.4.5 Directed Synthetic Jets

McKormick (2000) investigated the effect of a ‘directed synthetic jet’ on a 2D overcritical diffuser (diffuser angle of 30°) and a stalled aerofoil. The control mechanism of a directed synthetic jet as opposed to a standard synthetic jet is to combine the effects of suction and blowing. Because the jet neck is curved in the direction of the flow, the in stroke removes low momentum fluid and ejects it as high momentum fluid through tangential blowing. As the jet is used as a simple momentum injection/removal device less emphasis is placed on matching the operating frequency to a specific shedding frequency, instead emphasis is placed on tuning the jet orifice and cavity for an optimum momentum injection to power draw ratio. Using a directed synthetic jet on a 30° diffuser McKormick (2000) was able to create a pressure recovery at the diffuser exit twice as large as the optimum case of a 13° diffuser.

1.4.4.6 Thrust Vectoring

Smith and Glezer (2002) used a synthetic jet to alter the path of a steady jet of air. Figure 1.37 shows the streamlines of a steady jet being deflected by a synthetic jet actuator. The original focus of the work was for an aeronautical application, however this technique may be applied to the flow separating from the rear surfaces of a road vehicle to deflect high momentum flow downwards and into the wake.

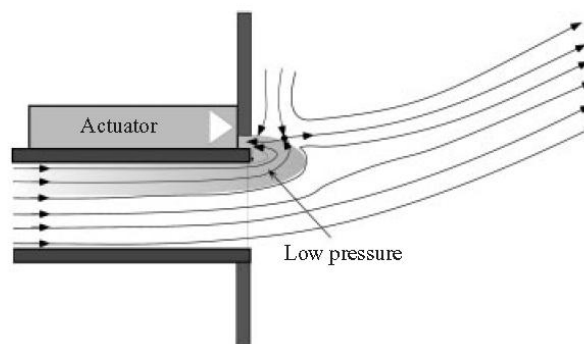


Figure 1.37 - Jet vectoring (Smith and Glezer, 2002)

1.5 Drag Reduction Techniques; Further Investigation

From the work discussed above some of the least intrusive techniques that show the greatest potential for drag reduction are constant blowing and suction, pulsed blowing and suction, and synthetic jets. The apparent low power and weight demands of the synthetic jet actuator as a means of flow control makes it stand out as an area to investigate further for road vehicle applications.

The different modes of operation and control open a wide scope for research work; in the work reported here the focus is on vehicle afterbody flow regimes. This work will study the use of blowing, pulsed blowing and synthetic jets to control flow separations from the rear upper roof edge of a vehicle. The modes of use of blowing or a synthetic jet located at this position to be investigated include; thrust vectoring, directed synthetic jets, virtual shape change devices, active vortex generators and vortex suppression.

It is also recognised that synthetic jet flow control techniques could prove useful in controlling separations in other locations on a vehicle such as, A-pillars, C-pillars, wheel arches, front edge radii, sunroofs and diffusers. The upper roof edge was chosen for investigation because it is an area where the flow structures will be least three dimensional, especially at and around the model centreline. The majority of previous work using SJ actuators has been conducted using 2D configurations such as wings and cylinders, and so it was decided to avoid attempts to control 3D structures as far as is possible on automotive bluff bodies. However, before an active control technique can be used to control the flow around a vehicle it is important that the flow structures intended to be controlled are understood as fully as possible.

The main objectives for the thesis include:

- Identify flow regimes in the wake of square back vehicles which can be targeted using active flow control
- Design and develop actuators and means of creating active flow control devices, such as synthetic jets, pulsed jets or blowing
- Apply the actuators to a 3D bluff body configuration representative of a squareback vehicle model in an attempt to control the wake flow and reduce drag
- Conduct tests at appropriately large freestream Reynolds numbers that could be considered to be matched with full scale configurations
- Identify the mechanisms which contribute to changes in drag and lift as a result of the applied actuation method

In order to satisfy the objectives, tests are conducted in the Loughborough University $\frac{1}{4}$ scale wind tunnel using a number of different data acquisition techniques. These techniques are discussed in Chapter 2 followed by an experimental investigation into the flow structures behind a simplified squareback vehicle model which is discussed in Chapter 3.

Chapter 2

EXPERIMENTAL METHOD

2.0 Experimental Method

Specific configurations for each experiment described in this thesis varied depending on the aims of the individual investigation, however the test facility used and some data acquisition techniques remained mainly consistent. Where techniques are varied they are explained alongside their relevant experimental introduction, where techniques and equipment was a constant they are described in this chapter.

2.1 Experimental Uncertainty

Throughout the thesis accuracy, error, uncertainty, bias error and precision will follow the definitions outlined in Coleman, H.W. and Steele, W.G., (1999). These definitions are summarised below:

- Accuracy of a measurement indicates the closeness of agreement between an experimentally determined value of a quantity and its true value
- Error is the difference between the experimentally determined value and the true value, the total error will be composed of two elements; bias error and precision error
- Uncertainty is the estimate of error in a measurement and is required because the ‘true value’ is often not known
- An error is classified as precision error if it contributes to the scatter of the data; otherwise, it is bias error.

Where a measurement uncertainty for a specific piece of equipment is available it is stated in the sections below. Where time averaged measurements are calculated from instantaneous data stamps uncertainty is quoted to a given level of confidence. The uncertainty of a measurement is calculated using Equation 2.1 where N is the number of samples acquired, σ is the standard deviation of the instantaneous results and t^* is a distribution factor associated with the confidence level stated. Values of t used for a given confidence level are shown in the Table 2.1. Throughout the thesis confidence of 95% is used unless otherwise stated.

Equation 2.1

$$\epsilon_{\mu} = \frac{t\sigma}{\sqrt{N}}$$

Table 2.1 - t value used in accuracy calculations

Confidence	68%	90%	95%	99%	99.5%
t^*	1	1.645	1.960	2.576	2.807

2.2 Wind Tunnel and Force Balance

All tests were conducted in the Loughborough University closed working section, open circuit wind tunnel (Figure 2.1). The working section of the tunnel is 1.92mx1.32m and it is capable of operating between speeds of 5-45m/s. At test speeds of 40m/s the freestream turbulence intensity is less than 0.2% and the boundary layer is typically 50-60mm thick at the model centreline position. Tunnel velocity is calculated from measurements of tunnel air temperature, ambient pressure, and freestream total and static pressure.

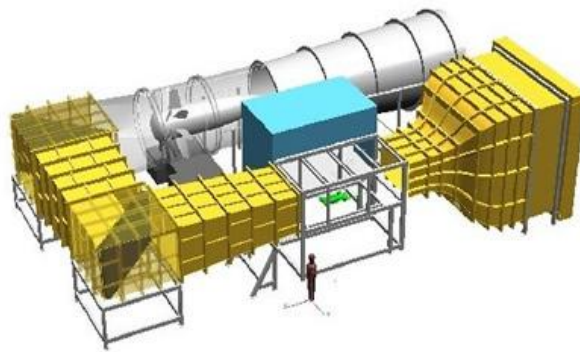


Figure 2.1 - Loughborough University Wind Tunnel

The pitot tube is mounted from the roof of the working section 2m upstream of the model centreline position. Total and static pressures are recorded via a Furness Controls FC0332 differential pressure transducer accurate to $\pm 2.5\text{mmH}_2\text{O}$ of the full range of $\pm 250\text{mmH}_2\text{O}$. Temperature is recorded using a thermocouple mounted inside a pitot tube and ambient pressure is measured using a barometer located in the wind tunnel control room.

The tunnel is equipped with a six component under floor balance capable of logging force data at speeds of up to 250Hz. The high acquisition speeds can be used to perform temporal analysis of the aerodynamic forces applied to a model, however within this thesis data is acquired at 5Hz and averaged over a 30 second sampling time. However the data stamps taken at 5Hz are themselves block averaged from a raw voltage signal running at 4.6KHz. Once the balance has been calibrated data in each axis is accurate to the values shown in Table 2.2.

Force/Moment Component	Load Range	Uncertainty (%FSD)
Drag	±120N	0.01
Side Force	±420N	0.005
Lift	±500N	0.01
Roll Moment	±150Nm	0.01
Pitch Moment	±60Nm	0.01
Yaw Moment	±45Nm	0.015

Table 2.2 - Balance Accuracy

Force measurements from the balance are used in conjunction with temperature and ambient pressure data to calculate a coefficient of drag (C_d) or coefficients of lift (C_l). C_d values are calculated using Equation 2.2 where F_{DRAG} is the force measured at the balance, V is the tunnel freestream velocity, A is the model frontal area and ρ is the air density.

Equation 2.2
$$C_d = \frac{F_{DRAG}}{\frac{1}{2}\rho V^2 A}$$

The air density for each measurement is calculated using Equation 2.3, where P is the ambient pressure, R is the specific gas constant and T is the air temperature.

Equation 2.3
$$\rho = \frac{P}{RT}$$

All coefficients (C_F) calculated from any force measurements taken are corrected for blockage effects using Equation 2.4 where E is the ratio of model frontal area to working section cross sectional area.

Equation 2.4
$$C_{Fcorrected} = \frac{C_{Fmeasured}}{(1+2E)}$$

All balance measurements were taken over a 30 second sampling time which allows C_d changes of $\pm 0.001C_d$ (1 count) to be measured with a 99% confidence. Figure 2.2 shows an example plot of a series of measurements taken in the wind tunnel using a generic car shaped bluff body at 40m/s freestream velocity. The plot shows positive and negative standard error bands for a 99% confidence measurement and where the measurements for drag coefficient fall if acquired for different sampling times.

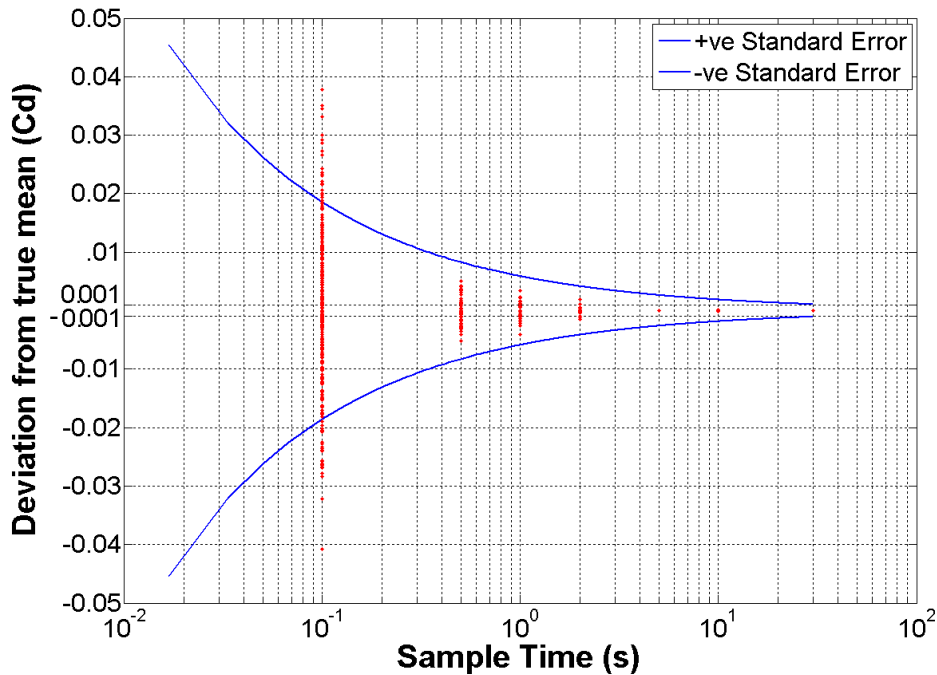


Figure 2.2 - Example of drag coefficient measurement for a road car bluff body model configuration with different sampling periods

2.3 Surface Pressure Measurement

Model surface pressure measurements are recorded using 1mm bore pressure tapings connected via flexible tube to two 64 channel PSI DTC pressure scanners mounted inside the model (Figure 2.3). Data was acquired at 312Hz from pressure transducers and written to a data logging computer via CAN technology. The static accuracy of the scanners ranges between $\pm 0.06\%$ to $\pm 0.1\%$ of the full scale of $\pm 232\text{mmH}_2\text{O}$ depending on the operating conditions. The data from pressure scanners was used to calculate coefficients of pressure using Equation 2.5.



Figure 2.3 - Pressure scanner and CanDaq

Equation 2.5

$$C_p = \frac{p - p_\infty}{\frac{1}{2}\rho V^2}$$

All pressure readings were corrected for blockage using Equation 2.6.

Equation 2.6
$$C_{Pcorrected} = \frac{C_{Pmeasured} + 2E}{(1 + 2E)}$$

2.4 Hot Wire Anemometry

For steady jets, pulsed jets and synthetic jet characterisation a hot wire anemometer was used to measure the jet exit velocity. The hot wire system consists of a Dantec Streamline frame with internal hardware signal conditioners capable of applying voltage gains and signal filters. Voltage data is written to a data logging computer via an internal A/D convertor capable of logging resolutions up to 250kHz.

Jet exit velocities were measured by positioning a 1D straight (55P11) hot wire probe at a nominal distance of 1mm from the jet exit (see Figure 2.4). The fluctuation in wire voltage is then converted to a velocity from a calibration curve.

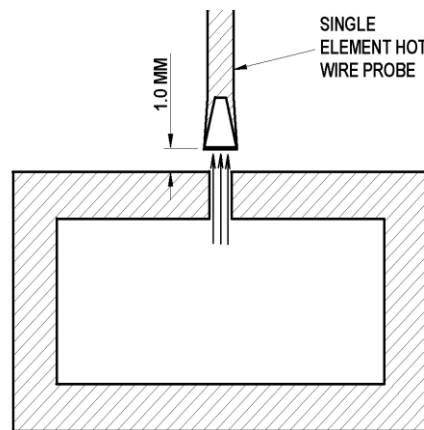


Figure 2.4 - Jet velocity measurement using hot wire

Velocity calibrations are performed for the relevant test velocities using a Dantec velocity calibrator which itself has an uncertainty of 0.02%. Temperature fluctuations are measured using an ambient temperature probe and accounted for by applying the temperature correction shown in Equation 2.7.

Equation 2.7
$$E_{corr} = \left(\frac{T_w - T_0}{T_w - T_a} \right)^{0.5} \cdot E_a$$

Where E_{corr} is corrected voltage, T_w is the sensor operating temperature, T_0 is the ambient temperature at the time of setting the overheat properties and T_a is the ambient temperature at the time the sample

is taken. T_w is calculated from Equation 2.8 where α_0 is the sensor temperature coefficient and a is the overheat ratio (typically 0.8).

Equation 2.8
$$T_w = \frac{\alpha_0}{a} + T_0$$

The hot wire probe is mounted on a 2D traverse system which can be manoeuvred within the jet outlet region to quantify the jet shape of the jet or to traverse along the length of a 2D jet and spatially average the measured velocities. In conditions where the velocities are to be averaged spatially the angular alignment of the slot relative to the axis of the jet is configured such that amount that the hot wire is spaced away from the outlet does not vary by more than $\pm 0.2\text{mm}$.

2.5 Particle Image Velocimetry

Particle Image Velocimetry (PIV) is an image measurement technique that can spatially resolve flow velocities within an area of interest whilst remaining relatively non-intrusive to the flow field. The technique uses a dual pulsed laser to create a planar light sheet which illuminates neutrally buoyant tracer particles that have been ‘seeded’ into the flow medium, upstream of the area of interest (See Figure 2.5). The generation of a pair of light sheets at a short temporal displacement is synchronised with the camera frame acquisition times of a dual exposure, CCD camera. This generates a pair of images with a known time step between them, referred to as the inter-frame time.

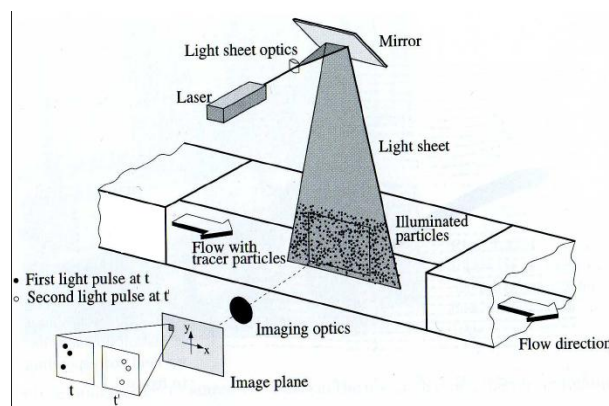


Figure 2.5 – Typical PIV configuration (Raffel et al., 2007)

For each configuration, data is processed by breaking down the first and second images of each pair into interrogation cells. A cross-correlation is then performed between the particles in each cell in the first and second image. From this correlation particle displacements and velocity vectors can be resolved.

Instantaneous velocity flow fields for each image pair can be used to display statistical information such as mean and RMS velocities, or further derivation can be used to generate information regarding vorticity, swirl strength, turbulence intensity and typical length scales.

At each stage of the PIV process a number of parameters can be tuned in order to produce high quality data. These various parameters are often not complementary so tradeoffs must be made. Some rules and processing settings that have been consistently applied at the various stages of PIV experimentation within this thesis are outlined below, whilst specific test setups will be described in their relevant sections.

2.5.1 Seeding and Camera Field of View

Both oil and water seeding systems have been used during the PIV experimentation reported here, where the average particle diameters are 2-5 μm and 2-6 μm respectively. Particle size, or more specifically the diameter of the reflected laser light from the particle imaged by the CCD chip in conjunction with the resolution and field of view of the camera(s) used are important factors to consider if ‘peak locking’ is to be avoided.

Peak locking occurs when the reflection from a particle is less than or equal to one pixel in diameter. If this is the case any shift in particle position from image one to image two can only be resolved to ± 1 pixel. Ideally a particle reflection diameter should occupy 2-6 pixels (Hollis, 2004), in order that a fitting function may be applied to the correlation data and particle displacement can be resolved at sub pixel levels. Because particle diameters, and camera resolutions cannot easily be modified, peak locking can be reduced during testing by reducing the field of view.

Peak locking can be detected by looking at a probability density function of the shifts detected in the vector field. Figure 2.6 shows a PDF for vector field where velocities tend towards integer values of pixel shifts, and it can be argued some of the particle images in this data are too small. Figure 2.7 shows a non-peak locked measurement where calculated shifts are distributed evenly between 0 and 1 fractions of pixel shift.

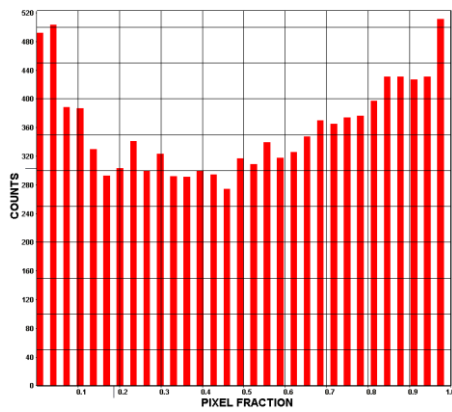


Figure 2.6 – Onset of peak locking

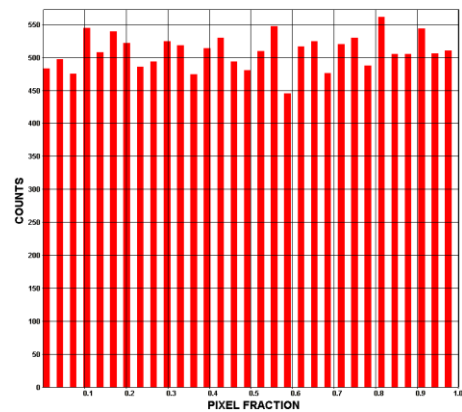


Figure 2.7 - Non-peak locked PDF

2.5.2 Image Acquisition

During a new experimental setup it is key to ensure that images being captured are of a high enough quality. For this reason a short sample of around 50 image pairs is normally taken and processed to check the quality of the images before full data sets are collected. These checks can be used to avoid peak locking and create a good level and quality of seeding. Low levels of seeding can lead to a low number of first choice vectors being available to generate a velocity field. A minimum of 95% first choice vectors was set as a standard throughout all tests; more details on vector choice will be covered in section 2.5.4.

For image acquisition dual frame shift register type CCD cameras were used. The laser is timed to work in phase with the frames recorded by the camera as shown in Figure 2.8. Figure 2.8 also shows the inter-frame time which must be set depending on experimental setup. The optimum inter frame time is a function of the seeding particle velocity through the laser light sheet, and the interrogation window size to be used in the processing of the image. Particle pixel displacements between frames must be large enough to be measurable, but ideally no larger than $\frac{1}{4}$ the interrogation window size (Hollis, 2004). Large inter frame times may also result in particles moving out of the light sheet before the second frame is acquired, which can occur in cases with high velocity in plane flow, or swirling flows with large out of plane velocity components.

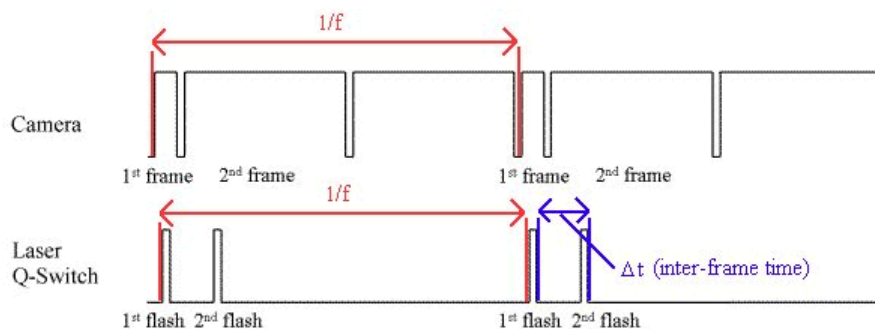


Figure 2.8 - Camera and laser timing sequence (Hollis, 2004)

The camera lens should be used to focus the CCD chip onto the plane of the light sheet such that seeding particles are clearly identifiable. Ideally an F-stop setting would be used that creates the same depth of field as the thickness of the light sheet. However due to the required trade off between identification/illumination of particles and avoiding overexposure of the camera, depth of focus can be larger than the light sheet thickness. This means that it is possible for particles outside of the plane of interest to be included in calculations of velocity vector fields. Laser Intensity along with the lens and f-stop setting must be tuned to arrive at the best configuration available.

Reflections of light from the model and tunnel walls can also have an influence on the correlations performed to generate a vector field. To reduce the effect background reflections and bright spots have on the data a background image is taken of each configuration without seeding. Before processing the vector fields the background image is subtracted from every image pair.

2.5.3 Data Processing

In order to generate a velocity vector field from each instantaneous image pair the pixels within the field of view are divided into ‘interrogation cells/windows’. A cross-correlation is performed between the interrogation cells in the first image and the interrogation cells in the second image. Where high levels of correlation occur a large spike can be seen in a correlation plot such as in Figure 2.9. This spike can be used to generate a velocity vector for the interrogation window in question. When a cross correlation has been performed for every interrogation window, a velocity vector plot for the whole field of view can be generated.

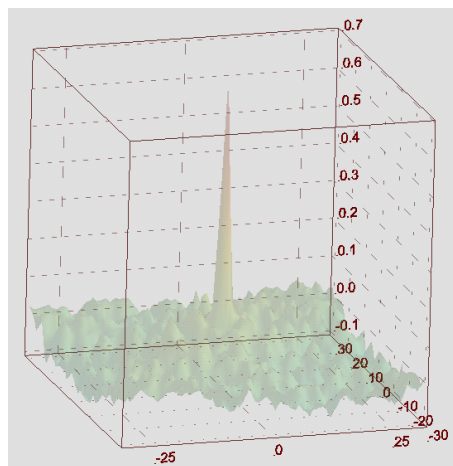


Figure 2.9 - Example interrogation cell correlation plot

Multiple correlation passes with decreasing interrogation window sizes can be used to gradually shift the position of the cells in the second frame to follow the expected path of the particles. This is

illustrated in Figure 2.10 and ensures that particles are not leaving the interrogation window in between frames.

An amount of cell overlap can be applied in order to increase the data yield by increasing the vector grid density. Obviously the larger the number of correlation passes and the larger the percentage overlap the longer the processing time. In general, in the processing used in this thesis 3 passes of correlation were used. The first two passes used a 128X128 window size, while the final pass used a 32X32 window size. The final two passes allowed cell shift to follow the estimated movement of the particles, with a 50% overlap. Depending on the camera that was used and the field of view selected the amount of overlap and the final window size will determine the resolution of the vector grid produced.

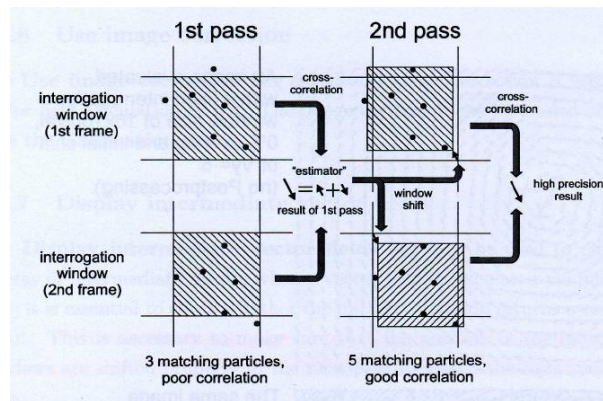


Figure 2.10 - PIV interrogation cell passes

2.5.4 Post Processing

Vector fields are initially processed without any post processing applied and the results are checked to ensure that the data is of an acceptable quality. It is inevitable that in some circumstances instantaneous vector fields may contain small amounts occurrences of spurious vectors. In this case vector post processing can be used to ensure these values are not used in the calculation of averages and are excluded from the instantaneous results. A simple 'allowable vector range' can be set to remove any vector values that have unexpected magnitudes or directions. These values will be set based the expected behaviour of the flow field in question.

A clear correlation peak such as the one in Figure 2.9 is the ideal aim for every interrogation window. However, as the quality of the seeding reduces, the ratio of primary peak magnitude to that of the next identifiable peak in the correlation can be low. This ratio is the signal to noise ratio and is referred to as the Q ratio. If this is the case a decision needs to be made about whether or not to keep this data point or assume it is only noise so remove the vector calculated from the resultant vector field. Additionally if there is more than one large correlation peak to choose from, a decision needs to be

made about which one to use. This can be done using a median filter. The median filter will calculate the mean and RMS of the neighbouring cells around the cell in question. It will then check that the chosen peak produces a vector that is less than a specified multiple of RMS from the mean of its neighbours. If not a second, third or fourth peak can be selected that is closer to the mean, before the data is removed. These vectors would then be referred to as second, third or fourth choice vectors respectively.

Throughout the data processing in this thesis any data with a Q ratio of less than 1.3 was discarded. A median filter was set to 'strongly remove and strongly replace' vectors more than 2.5 times the RMS from the mean. If possible these vectors would be replaced with lower choice vectors with values less than 3.5 times the RMS from the mean.

Obviously these post processing steps are the least favourable option to produce a reliable vector field, which emphasises the need to get good quality raw data to avoid having to implement significant amount of post processing. Throughout this work the minimum number of first choice vectors acceptable for a configuration was 95%.

2.5.5 PIV Resolution, Accuracy and Precision

PIV calculates velocity vectors on a regular grid by dividing the image from the CCD chip of the camera down into interrogation windows as described in section 2.5.3. The size of the measurement area, the size of the interrogation windows used and the amount that the interrogation windows are overlapped are the factors that determine the spatial resolution of the vectors produced. In the current work it is desirable to image as much of the model wake region as possible whilst still being able to identify small fluctuations that may develop into large shed structures. Different PIV hardware was available for use at different stages of the research and as such different resolutions and areas of interest were possible.

Initially a single camera system was available with chip architecture of 1376x1040 pixels. Typically this camera would be used to view a field of view (FoV) of 330mmx300mm giving a worst case scaling of 0.289mm/pixel. For a processing scheme using 32x32 pixel windows with 50% overlap this results in a vector grid resolution of 4.6mm. This resolution means that it would not be easy to see any very small scale fluctuations that may be of interest, for example shear layer roll up, however it is still possible to see larger scale fluctuations in the shear layer.

For the later work in this thesis 2 cameras were used side by side with a scaling of 0.146mm/pixel which gave a vector grid resolution of 2.3mm for the typical processing parameters used. This

configuration allows a significant measurement area whilst increasing on the vector grid resolution from the initial setup. It can still be argued that the vector grid resolution is too large to pick up small scale shear layer fluctuations or roll up but the data yield from this measurement is very large and a number of small scale fluctuations can still be identified in instantaneous images. Figure 2.11 shows an example instantaneous PIV vector field of a stream wise centre line plane in the wake of a square back bluff body model. (see Figure 5.8 for specific measurement location, the back of the model is shown on the right hand side of the plot as a black area). The plot is shown on a full page so that it is not necessary to reduce the displayed vector resolution. This figure illustrates excellent level of detail achievable in such a large field of view with a high grid resolution.

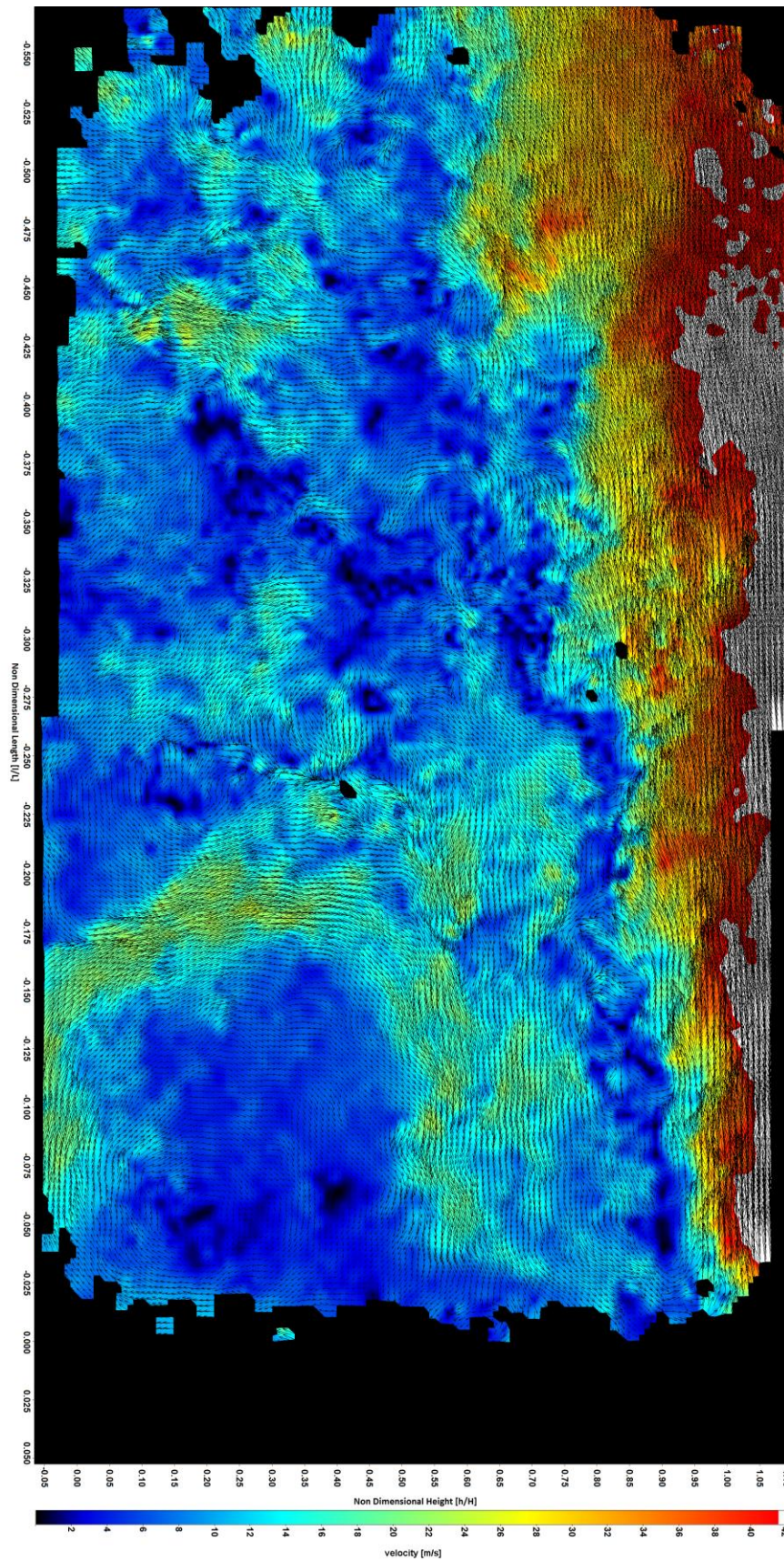


Figure 2.11 – Instantaneous PIV velocity field of squareback vehicle model showing vector resolution achieved

A number of factors can influence the uncertainty of an instantaneous PIV measurement and the overriding concern is that the raw images acquired are of a good quality. The steps taken to maximise accuracy during the processing of the instantaneous images has been outlined in Section 2.5.3 and 2.5.4. However a finite measure of the total error at any one velocity vector can only be calculated if the ‘true’ velocity is known.

The only way of starting from a known value is to generate synthetic images with a known ‘shift’ or particle displacement. From these images the error associated with the ability of the correlation algorithm to calculate the known shift can be determined. Figure 2.12 shows an example of synthetic data with a low level of shift and a step change in shift in the centre, compared to the calculated values of shift. For the calculated values, a level of fluctuation in the calculated values can be seen and the spatially averaged RMS error can be regarded as the total error associated with the correlation at a specified shift.

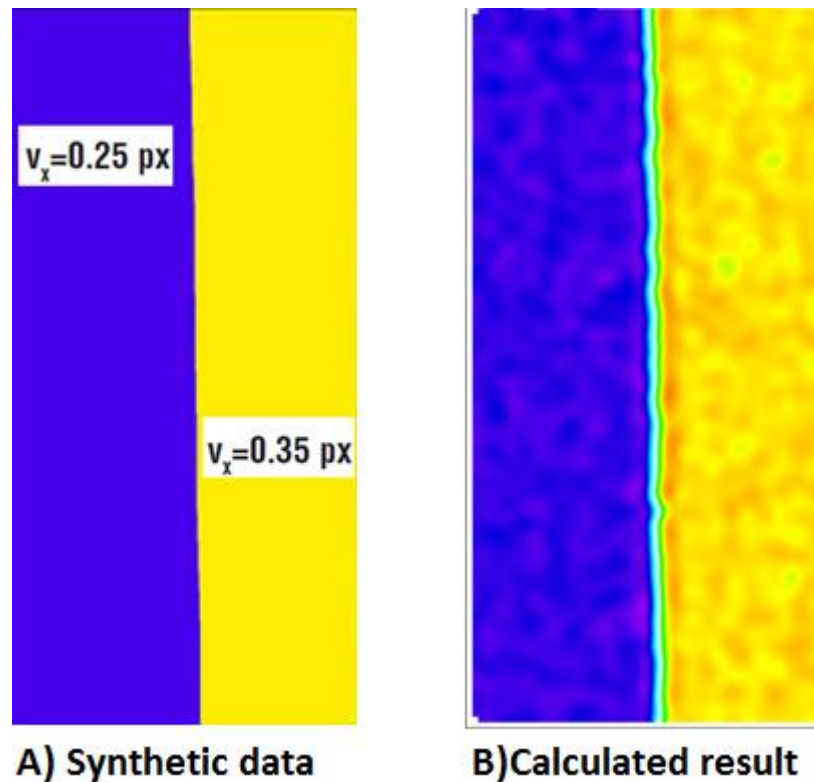


Figure 2.12 - a) Synthetic and b) calculated data

The RMS error will vary with the level of shift and the processing setting used, however typically the algorithm used will resolve shifts of 0.1-10 pixels with an RMS error of 0.01 pixels. This error can be converted to a displacement depending on the scaling used in the experiment, i.e. the Field of View (FoV) and chip architecture.

Although this gives an error in displacement the term of interest is velocity which is calculated from Equation 2.9 and the other term which can contain error is the time signal. The programmable timing unit used has a maximum signal jitter of 5ns which can be considered as the time error. Errors in t and d will propagate to the standard deviation of V via Equation 2.10. In most cases time averaged results will be calculated from a number of samples. In this case the calculated error associated with the PIV system will contribute to total experimental uncertainty of the experiment. This uncertainty is calculated for a given confidence level and number the number of samples used and it can be calculated using Equation 2.6.

Equation 2.9
$$V = \frac{d}{t}$$

Equation 2.10
$$\sigma_V = \sqrt{\sigma_d^2 \left(\frac{1}{t}\right)^2 + \sigma_t^2 \left(\frac{d}{t^2}\right)^2}$$

The error in V will vary with the magnitude of V , therefore the variation has been plotted in Figure 2.13. This plot is calculated for a configuration typical to the measurements to be made in the current work; the FoV used is 300mm² with a 4 megapixel chip (2048x2048 pixels) giving a scaling of 0.146mm/pixel. It has been assumed that the typical shift will be 5 pixels. The propagated error in V has then been used to calculate it's contribution to the measurement uncertainty within specific confidence bands if 1000 samples had been taken. Figure 2.13 shows that even for a confidence level of 99.5% the uncertainty in the measured velocity is very low with the worst case uncertainty of $\pm 1.6 \times 10^{-3}$ m/s for a 40m/s velocity.

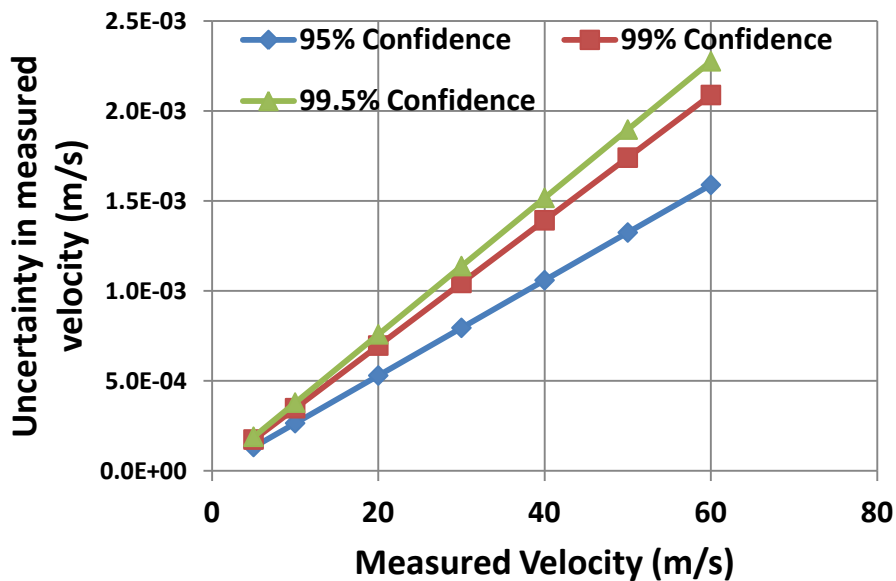


Figure 2.13 - Uncertainty in velocity measurement

However the uncertainty of the measured velocity in an averaged flow field will also be a function of the RMS of the velocity caused by the turbulence in the flow field. Because the current work is investigating wake flows it is fair to assume that the RMS due to the turbulence will be at least an order of magnitude higher than the RMS caused by measurement error. For this reason it makes sense to investigate what the uncertainty of an averaged flow field will be by investigating real experimental data where the 'true' velocities may not actually be known.

An example data set has been used in Figure 2.14 to illustrate the effect of the number of samples used in the calculation of an averaged flow field on the quoted uncertainty of calculated flow field. The data set shows the wake of a ¼ scale car model (Figure 3.1) and uses Equation 2.1 and Table 2.1 to calculate the uncertainty for a given 99% confidence level. The uncertainty of the velocity magnitudes at the different spatial locations is shown as a contour plot.

The link between the precision error and RMS in the flow field due to turbulent fluctuations is highlighted in the plots shown in Figure 2.14. In regions where turbulence intensity is high such as the separated shear layer the largest measure of precision error is found. When fluctuations and turbulent intensities are low, such as at the centre of a stable vortex structure or in the freestream (which can almost be seen at the top of the vector fields) the precision error, is reduced.

The effect of increased sample size is also illustrated by the global reduction in statistical uncertainty the velocity fields. For a small sample size of only 200 image pairs the uncertainty in the shear layer is as large $\pm 2\text{m/s}$ and in most of the wake region it is between $\pm 0.5\text{m/s}$ and $\pm 1.5\text{m/s}$. By increasing the sample size to 500 image pairs the uncertainty in the shear layer region is reduced to $\sim \pm 1.3\text{m/s}$ and the uncertainty in the wake flow region ranges between $\pm 0.25\text{m/s}$ to $\pm 1\text{m/s}$. Using 1000 instantaneous image pairs to create the averaged flow field significantly reduces the uncertainty whereby the maximum is less than $\pm 1\text{m/s}$ and in the majority of the wake region the uncertainties are $\pm 0.2\text{m/s}$ and $\pm 0.6\text{m/s}$.

If the PIV results are to be used to calculate further criteria rather than just as a specialised means of flow visualisation it is important that the measurement uncertainty is known and quantified. If velocity values found in the shear layer are to be used this is especially important, as it can be seen that the statistical uncertainty can be significant in this region if a small sample size is used. For this reason all future averaged flow fields are made up of a minimum of 1000 instantaneous sample vector fields.

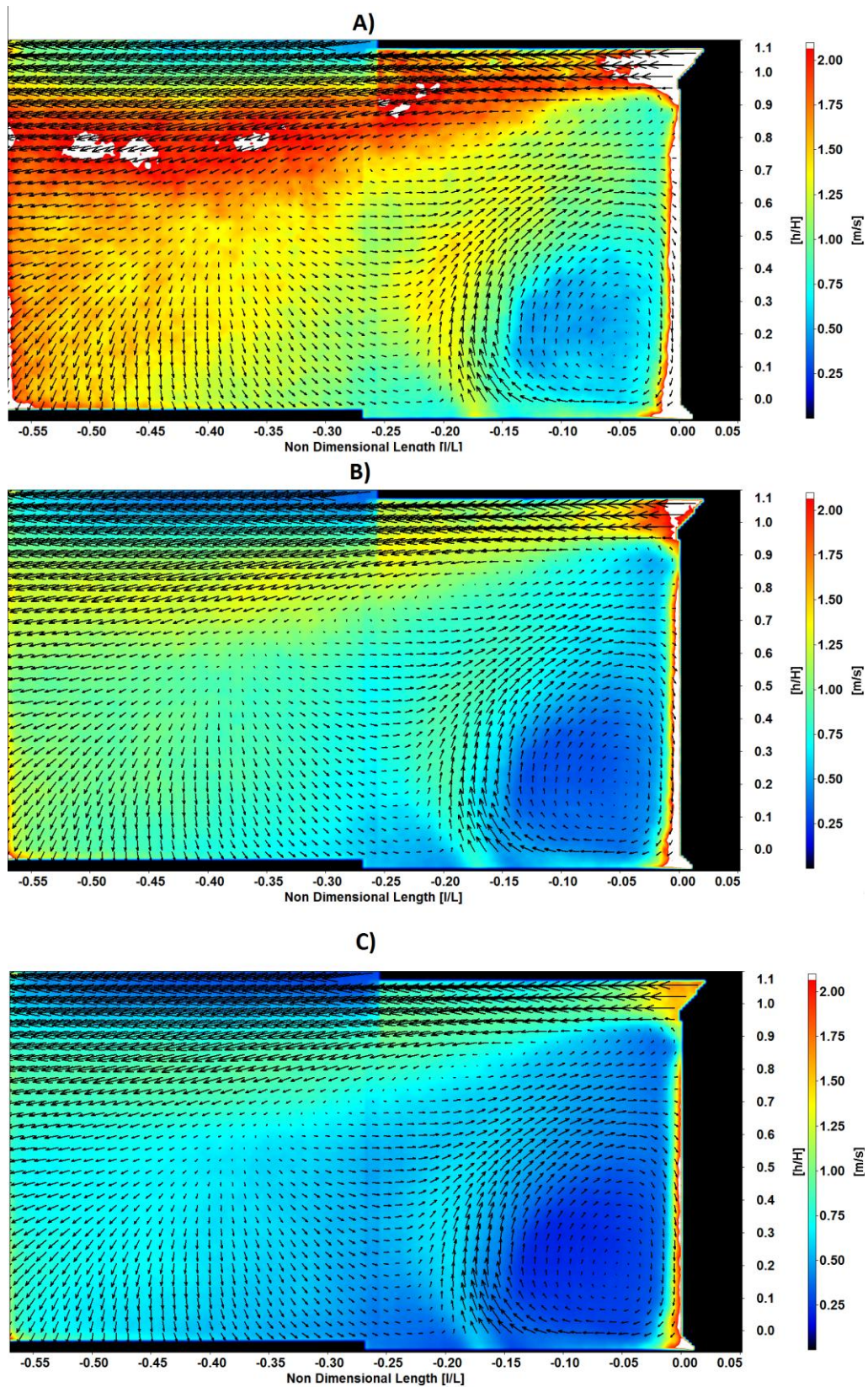


Figure 2.14 - Measurement uncertainty in velocity magnitude for example wake flow data. Contour plots show statistical uncertainty using averages of A)200 B) 500 and C) 1000 instantaneous image samples

2.5.6 PIV Summary

As may be deduced from the previous paragraphs, PIV is a technique that requires attention to detail in order to create a good statistical accuracy of the results. It is the authors' observation that some previous published work may have been called into question by the lack of sample sizes used. The general setup and configurations discussed above are summarised in the table below to highlight the emphasis that has been placed on gathering high quality data.

Category	Comments
Tracer particles	Both Oil and Water Used, 2-5 μ m and 2-6 μ m diameters respectively.
Laser	Dual Pulsed ND-YAG lasers used, sheet thickness ~1mm.
Particle image diameter	Aimed for 2-5 pixels in diameter.
Peak Locking	Avoided via inspection of $V_x V_y$ PDF plots, and adjusting field of view.
Acquisition timing	4.5Hz
Inter-frame time	Optimised to keep particles in light sheet, yet still allow pixel shift of $\frac{1}{4}$ interrogation cell size, typically 5-8 pixels.
Vector Choice	Minimum of 95% first choice vectors.
Processing – Correlation passes	Two passes at 128X128 window size, final pass at 32X32. Final two passes allowed cell shift with a 50% overlap.
Processing – Median Filter	Remove if difference to neighbour average is > 2.5 RMS. Replce with alternative choice if alternative choice is < 3.5 RMS from average of neighbours.

Chapter 3

**BASELINE VEHICLE CONFIGURATION
AND PASSIVE OPTIMISATION**

3.0 Baseline Vehicle Configuration and Passive Optimisation

3.1 Introduction

Before developing active control actuators or systems it is of benefit to understand how a form of active control may be able to influence the flow structures around a vehicle such that a reduction in drag is observed. It is often the case that published work where active flow control has been successful, has been implemented on configurations that exhibit mainly 2D, low Reynolds number flow behaviour. The goal of this thesis is to push these investigations further such that active flow control may be applied to more 3D and higher Reynolds number flow topologies typical of that found in road vehicle aerodynamics. However, model configurations such as the Ahmed body (Ahmed, Ramm and Falin, 1984) have not been selected for investigation, because of its highly 3D, and turbulent wake structure. Instead a squareback style vehicle model has been selected in the hope that its wake structure might exhibit more 2D behaviour that could in turn be more easily targeted by a certain control technique.

In order to identify the flow structures in squareback vehicle wakes that may be influenced by active control actuators, and also to benchmark any drag savings that may be available from a passive optimisation of the roof trailing edge, an investigation was conducted using a simplified $\frac{1}{4}$ scale vehicle wind tunnel model, referred to as the Windsor model.

The Windsor model used is shown in Figure 3.1. All the leading edges are well rounded to avoid separation with radii of 0.05m, with the exception of the roof leading edge which has a radius of 0.20m. The longitudinal and rear edges are sharp.

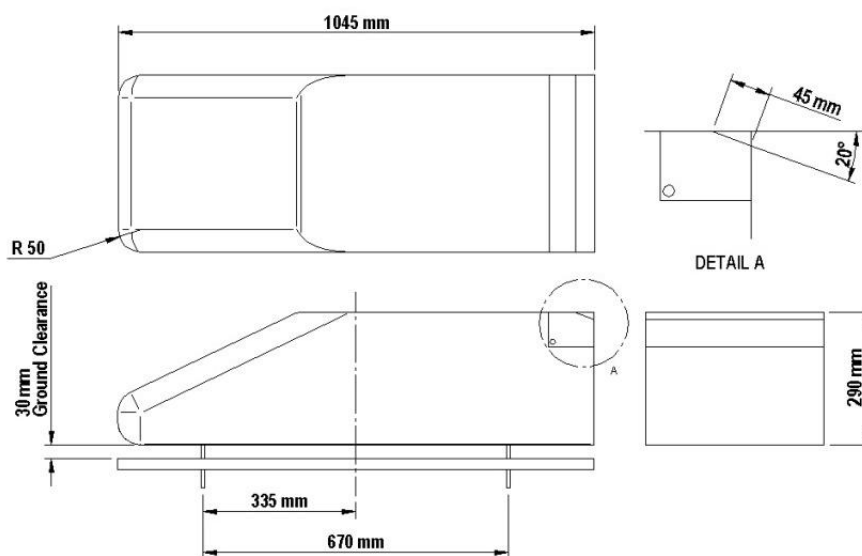


Figure 3.1 - Windsor model showing insert to facilitate different rear chamfer angles

In these initial investigations the model is equipped with interchangeable rear inserts to facilitate different chamfer angles at the roof trailing edge (Figure 3.2). Chamfer aspect ratio is defined as the ratio of model width to slant length, so in this experiment the aspect ratio of the chamfer is kept constant when using different angles by using a constant slant length. Previous investigations (Howell and Le Good, 2008) have used a similar setup to investigate the effect of fastback rear slant aspect ratio using aspect ratios of 1.25, 1.75 and 2.25. The current work uses a 45mm slant length giving a significantly higher aspect ratio of 8.66, with the aim of being representative of a small roof trailing edge optimization applied to full scale vehicles, and approximately 2D. The slant angles tested range from 0° (corresponding to a square-back configuration) to 20° in 4° increments.

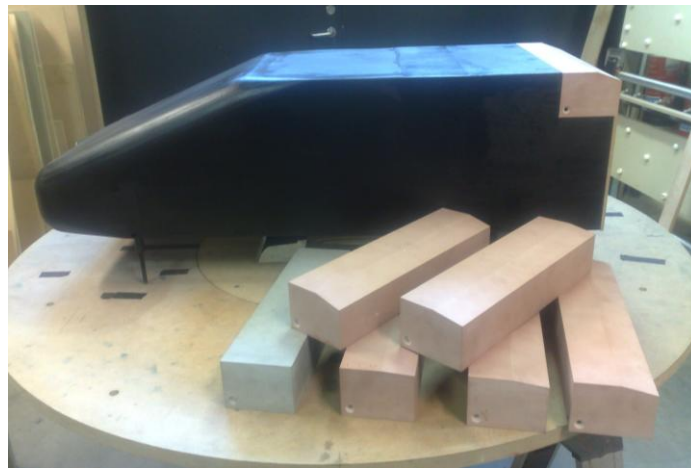


Figure 3.2 - Windsor model and interchangeable rear chamfer components

It was conjectured that the chamfer would reduce drag by turning the flow downwards, and increasing the base pressure, but also by reducing the overall base area. Much of the published literature discussing the application of active control to similar geometries talks of a similar turning of the flow to create base pressure recovery (Rouméas, Gilliéron and Kourta, 2006). However when using active flow control with no physical shape change, gains due to a base surface area reduction will not be available. Static pressure measurements were used in conjunction with balance measurements to quantify the various contributions to drag and the balance between the drag reductions as a result of changes to pressure on the base surface vs changes in base surface area. PIV was also used to gain an insight into the wake structure and the potential presence of any periodic structures that may be useful for active excitation.

In the tests discussed here the model was equipped with 113 pressure tappings, with the majority located in the base, and some on the roof and slant sections. The exact positions of the uppermost tappings varied slightly with the chamfer angle configuration but the general arrangement can be seen in Figure 3.3 which illustrates the positions for the square-back and 20° chamfer configurations.

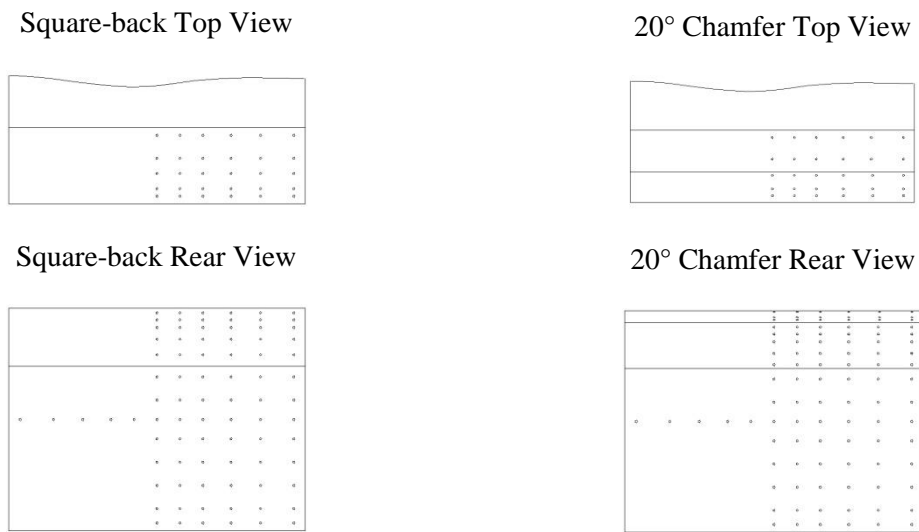


Figure 3.3 - Pressure tapping locations

A single camera PIV system was setup as shown in Figure 3.4 using a dual pulsed Nd:YAG laser to produce a light sheet in the stream-wise plane along the centre line of the model. Image pairs were acquired at 4.5Hz and a sample of 1000 image pairs was taken for each setup. The image inter-frame time was tuned to $25\mu\text{s}$, and a 25mm lens was used to give the wide field of view required behind the model. Parallax effects were compensated for in the calibration by applying a pinhole calibration model to the raw images and the raw images were also de-warped onto the flat measurement plane. Seeding was generated by a water seeder located approximately $0.5L$ upstream of the model front.

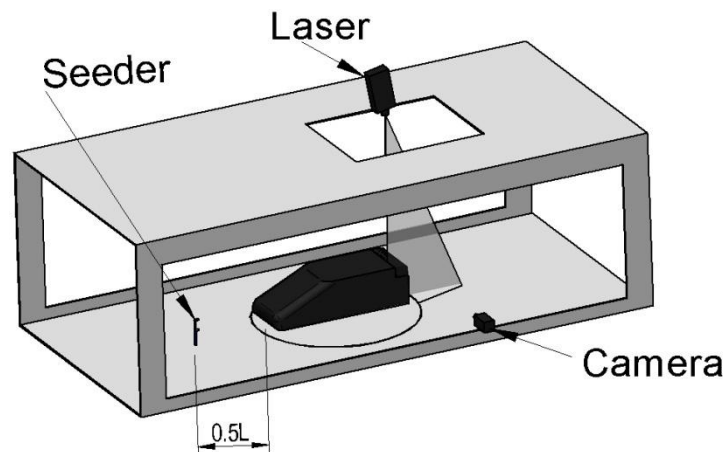


Figure 3.4 - Isometric view of PIV system configuration

3.2 Force and Pressure Measurement Results

Any scale model testing needs to take account of scaling effects. The main consideration in the current investigation is going to be ensuring that the ratio of inertial forces to viscous forces is representative of that found at full scale and that the dimensional scaling that is applied (25%) does not create any unsteady influence on the measured bluff body forces. This ratio can be characterised using a non dimensional coefficient called the Reynolds number, shown in Equation 3.1, where ρ is the fluid density, V is the fluid velocity, L is the characteristic length and μ is the dynamic viscosity.

Equation 3.1

$$Re = \frac{\rho VL}{\mu}$$

As freestream velocity is increased so too is the Reynolds number if all else stays equal. At low Reynolds numbers the force coefficients for the model may be ‘Reynolds number sensitive’. In order to ascertain what minimum freestream velocities could be legitimately used for the testing a Reynolds number sweep was performed for all the configurations. Within this sweep balance measurements were taken for the model between 10m/s and 45m/s in steps of 2.5m/s. Figure 3.5 shows that the C_d for the model in different configurations is Reynolds sensitive below a Reynolds number of 1.94×10^6 which corresponds to 27.5m/s tunnel freestream velocity. After a Reynolds number of 1.94×10^6 the C_d values begin to stabilise. This indicates that any future testing with the Windsor model should only be carried out at freestream velocities above 27m/s in order to avoid influence from Reynolds number effects

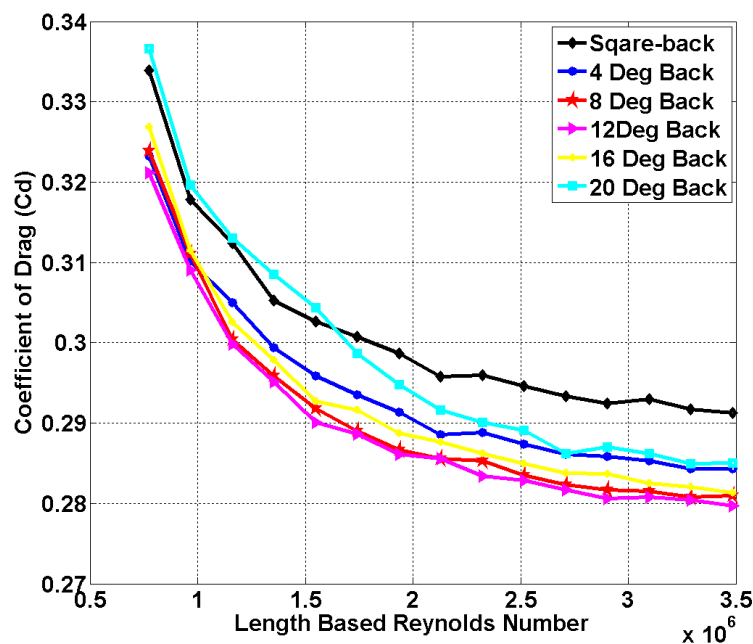


Figure 3.5 – Coefficient of drag vs Reynolds number for Windsor model

A higher resolution plot for balance measured drag coefficient against chamfer angle is shown in Figure 3.6 for a Reynolds number of 3.01×10^6 . All further plots in this chapter correspond to a test Reynolds number of 3.01×10^6 . The results follow the trends found by other authors (Ahmed, Ramm and Faltin, 1984),(Howell and Le Good, 2008), whereby the drag coefficient decreases to a minimum as the chamfer angle is increased from 0° to around 12° before beginning to rise again after that point. The shape of the curve in Figure 3.6 is dictated by the balance of mechanisms contributing to drag and mechanisms acting to reduce drag within each individual configuration. Typically for after-body flows, the drag reduction mechanisms will include an increase in base pressure or a decrease in rearward facing model base area and the drag contributions will arise from the formation of 3D trailing vortices and suction peaks on the rear slant.

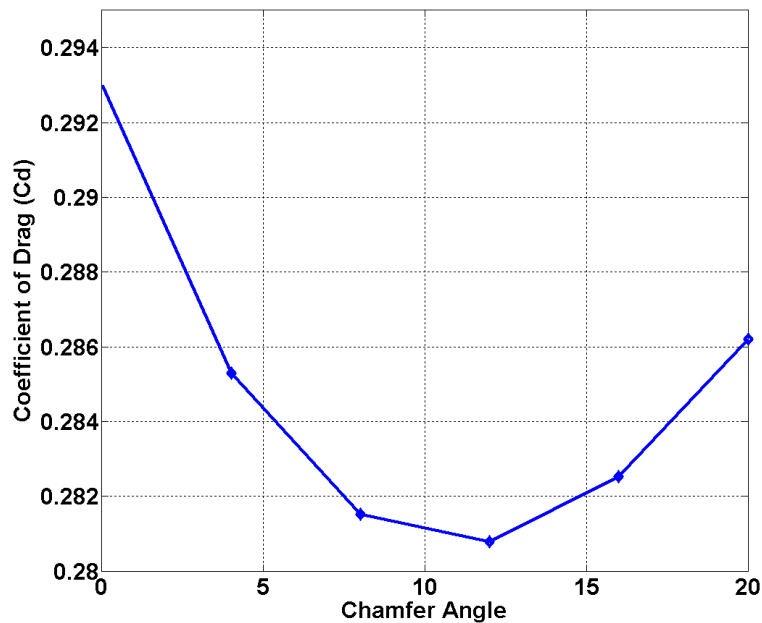


Figure 3.6 - Coefficient of drag vs chamfer angle

It is interesting that the shape of the curve is very similar for this very high aspect ratio slant as with lower aspect ratios. This is demonstrated in Figure 3.7 where the current data is plotted over data from Howell and Le Good (2008). With lower aspect ratio slants a lot of the initial reduction in drag has previously been attributed to the significant reduction in base area. If this is the case in the current high aspect ratio investigation then the application of active technology to create similar effects will be limited because there would then be no physical reduction in base area.

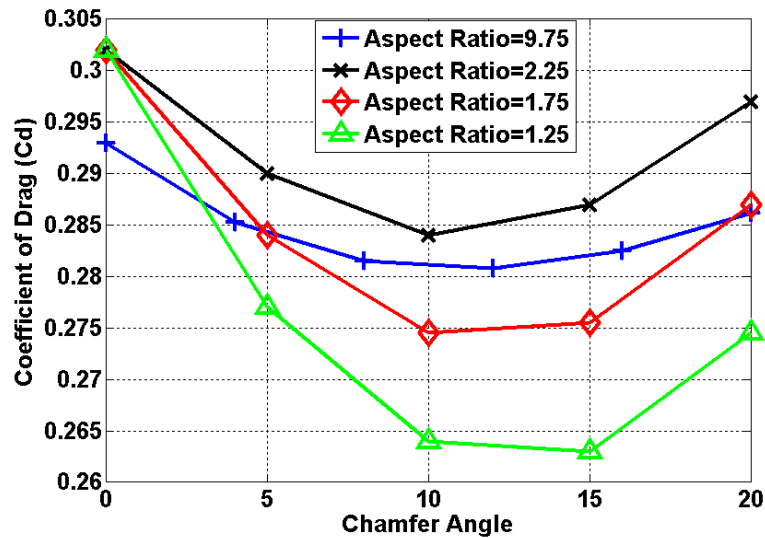


Figure 3.7 - Comparison of current aspect ratio slant with previous higher aspect ratio investigations (Howell and Le Good, 2008)

For the current work and the results seen in Figure 3.6 the initial decrease in drag with increasing chamfer angle is also attributed to an increase in base pressure, arising from the turning of flow downwards by the increasing chamfer angle, and a reduction in base area. However the majority of the drag reduction in the 4° configuration is attributed to the base pressure recovery. This is illustrated by the fact that C_d is reduced by 2.7% but base area is only reduced by 1.1%. The relatively large reductions that occur with a 4° slant angle can largely be considered as a 2D turning of the flow across the span of the model (excluding the outer extremities). In this configuration the contributions to drag arising from the formation of trailing vortices at the model edges and the area weighted contributions of the slant coefficients of pressure can be considered minimal.

As slant angle increases base pressure recovery, area weighted slant angle suction, and 3D vortex strength all increase, however their relative contributions vary. After 12° the drag begins to increase again because the influence from suction peaks on the slant and 3D trailing vortices outweigh any improvements in base pressure. It is worthy of note that C_d reductions of 2.7% (8 counts) and 4.1% (12 counts) relative to the Square-back configuration are achieved with only a 4° and 8° chamfer respectively.

This result is encouraging for the future implementation of active technologies which may be able to achieve turning of flow and base pressure recovery without a slant configuration, resulting in less drag penalty arising from slant suction peaks. Additionally, if a drag reduction of approximately 10 counts is achievable with minimal turning of the flow, the power draw of actuators used in the operation of active technologies may be less than aerodynamic power gain achievable.

The lift data shown in Figure 3.8 shows that the standard Square-back configuration produces negative lift; this is mainly as a result of its proximity to the ground plane and the onset of ground effect. As chamfer angle is increased lift increases almost linearly, with the gradient of the line correlating with the trends found by previous authors (Howell and Le Good, 2008). The increase in lift with increasing chamfer angle is associated with the rotation imparted on the upper wake as it is turned downwards. This creates a low pressure region on the upper rear surfaces, but also effects the flow speeds over and under the model leading to the increase in lift. It is again surprising that such a small shape change produces such a large change in lift with the difference between the baseline and the 20 degree chamfer configuration approximately $\Delta C_l = 0.225$.

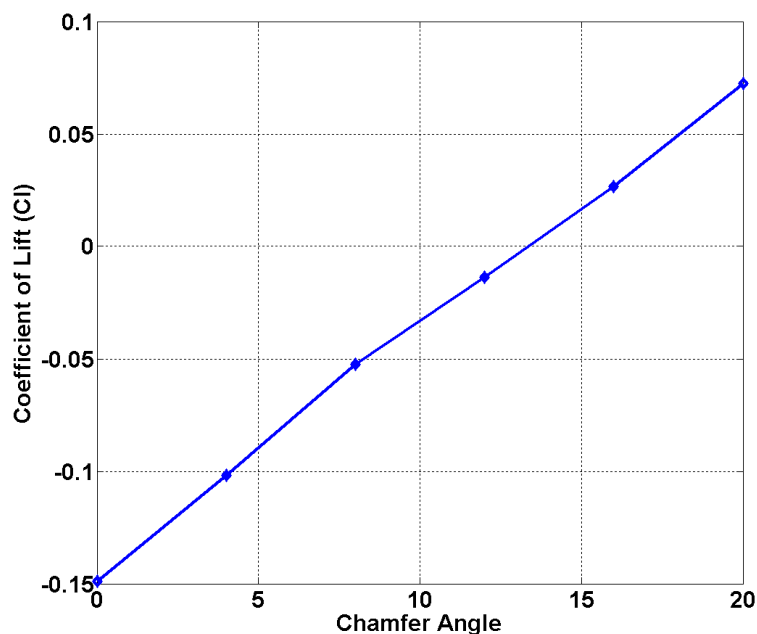


Figure 3.8 - Coefficient of lift vs chamfer angle

Figure 3.9 shows contour plots of pressure for one half of the base area (not including slant areas), as viewed from behind the model. $Y=0$ is at the model centre line, $Z=0$ is at the model floor plane and the axes extend to the outer edges of the model. The pressure data does not extend to the outer edges of the model because of the physical limitations during the installation of the pressure tappings. The small decrease in base area with increasing chamfer angle can be seen as a reduction in the area of the contour plot in the z axis. A value of $z=1.0$ is the top of the model and the edge at which the base meets the rear of the slant is shown as a dotted black line.

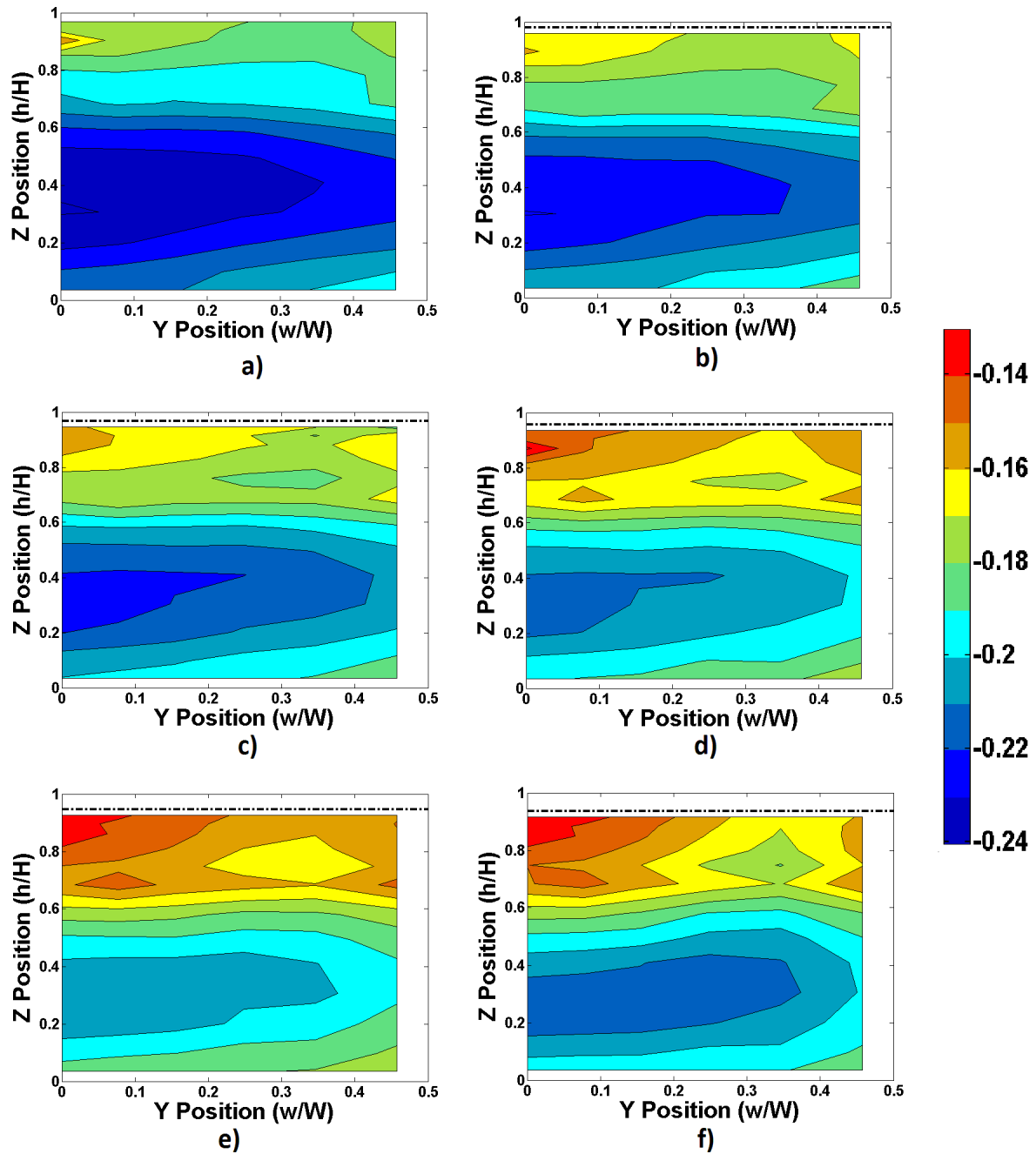


Figure 3.9 - Contour plots of coefficient of pressure on the base area of the model for: a) Square-back; b) 4° chamfer; c) 8° chamfer; d) 12° chamfer; e) 16° chamfer and f) 20° chamfer configurations. Dotted black line illustrates slant-base intersection point

In the Square-back configuration a large low pressure region is present across the majority of the span of the model between $h/H \approx 0.01$ and $h/H \approx 0.6$. This low pressure region is associated with a large separation bubble formed by the lower re-circulating wake region Ahmed and Baumert (1979). There is some indication of 3D structure at the outer corners of the model base that increases with increasing chamfer angle, but the separation region is largely 2D. As chamfer angle increases the

coefficient of pressure (C_p) within this separated region gradually increases from around -0.23 to -0.20, and its Z axis centre point shifts downwards from $h/H \approx 0.38$ to $h/H \approx 0.25$ in the Square-back and 20° chamfer configurations respectively.

To examine the relative contributions from the base and slant regions, an area weighted pressure coefficient was calculated using Equation 3.2.

Equation 3.2
$$\bar{C}_p = \frac{1}{A} \int_A C_p dA$$

Figure 3.10 shows the variation of C_d with increasing chamfer angle, measured using the balance, repeated from Figure 3.6, and the normal pressure contributions from the slant and base area as calculated using Equation 3.2. The difference between the balance measured C_d and the Base (C_b) and Slant (C_s) contributions is assumed to be made up of front end pressure contributions (C_k) and skin friction (C_f). As observed by previous authors (Ahmed, Ramm and Faltn, 1984) the contributions from C_k and C_f remain relatively constant with increasing chamfer angle, and the sum of the contributions from the rearward facing surfaces drives the total variation in C_d . Figure 3.10 also shows how the drag contributions increase and decrease with increasing chamfer angle for the slant and base areas respectively. The magnitudes of variation in C_s and C_b are much smaller than those found in previous work (Ahmed, Ramm and Faltn, 1984), however this is expected due to the high aspect ratio of the chamfer employed here.

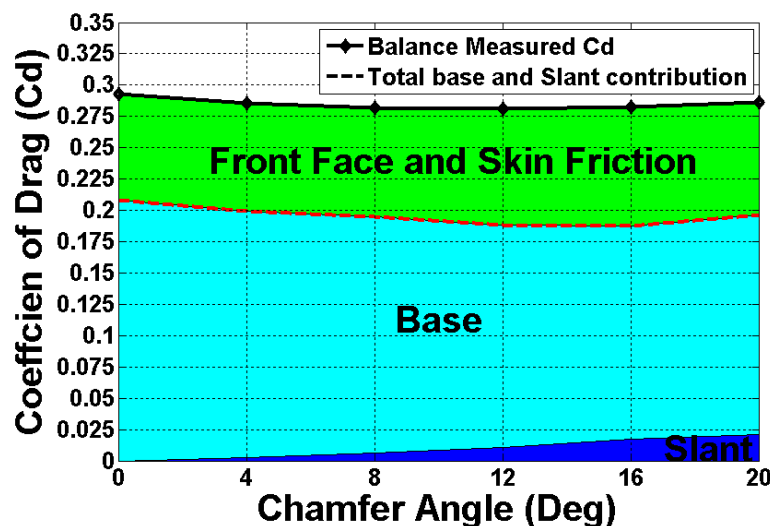


Figure 3.10 - Coefficient of drag vs chamfer angle from balance measurements and calculated area weighted pressure measurements

The distribution of pressures on the rearward facing surfaces dominate the changes in C_d for the configurations here and these pressures are influenced by how the wake flow develops and is

manipulated by the turning surface of the chamfer. Some authors (Roum  as, Gilli  eron and Kourta, 2006) have suggested that the induced angle of deflection of the flow downwards and into the wake has a direct and positive relationship with the amount of pressure recovery achievable in the wake. However, it can alternatively be argued that if downward rotation is added and wake length is shortened the resulting pressure in the wake will be lower, creating a greater suction on the base area (Bearman P.W., 1983) and consequently increase drag. Other published work (Pastoor et al., 2008) has tried to use active flow control to manipulate ‘in wake’ structures with the aim of influencing the global base pressure. Specifically this technique manipulates the proximity of vortical structures relative to the base surface by trying to move them away from the base surface, increasing the overall wake length as a result. To investigate the link between the wake structure, surface pressures and aerodynamic forces a PIV investigation was conducted in the wake of the model.

3.3 PIV Results

A common difficulty in PIV measurement techniques when using an open circuit wind tunnel is generating sufficient levels of homogeneous seeding; especially in wake regions. In this experiment this was achieved by positioning the seeding source in relatively close proximity to the front of the model (see Figure 3.4). To ensure that this did not unduly affect the results a simple test was conducted to compare the force measurements with and without the PIV equipment present. Figure 3.11 shows that while the seeder causes a displacement of the drag curve by around 2-3 counts, the trend observed is unaffected.

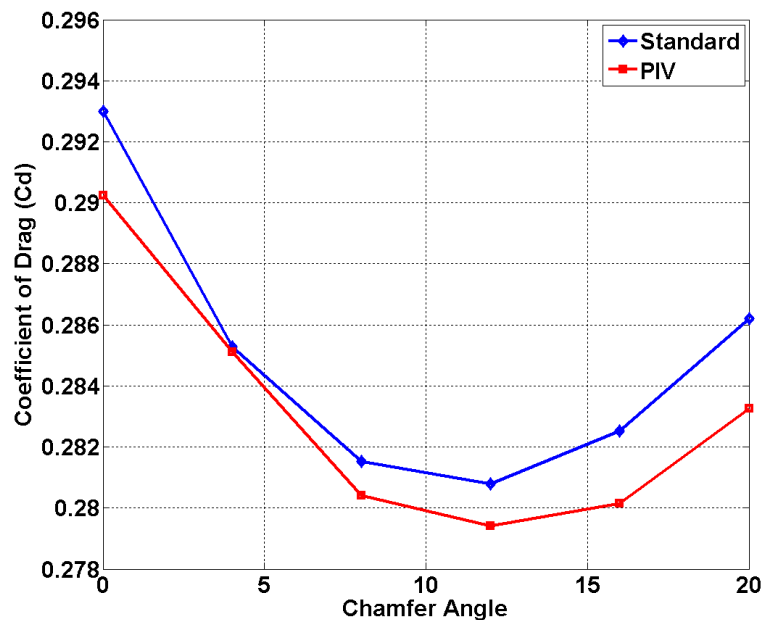
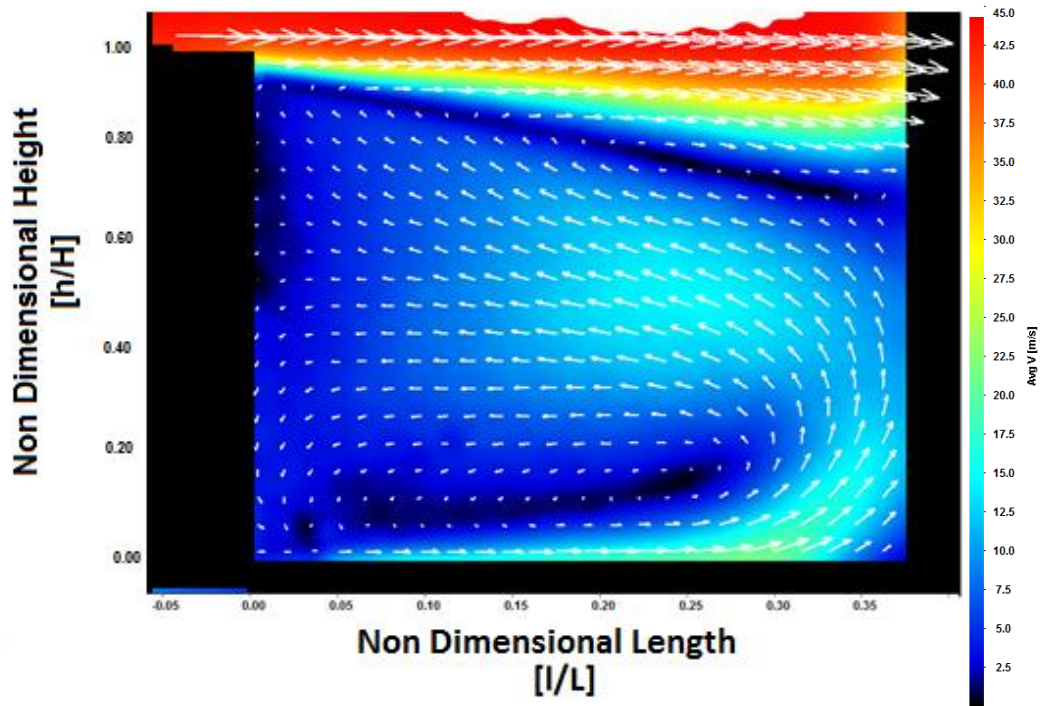
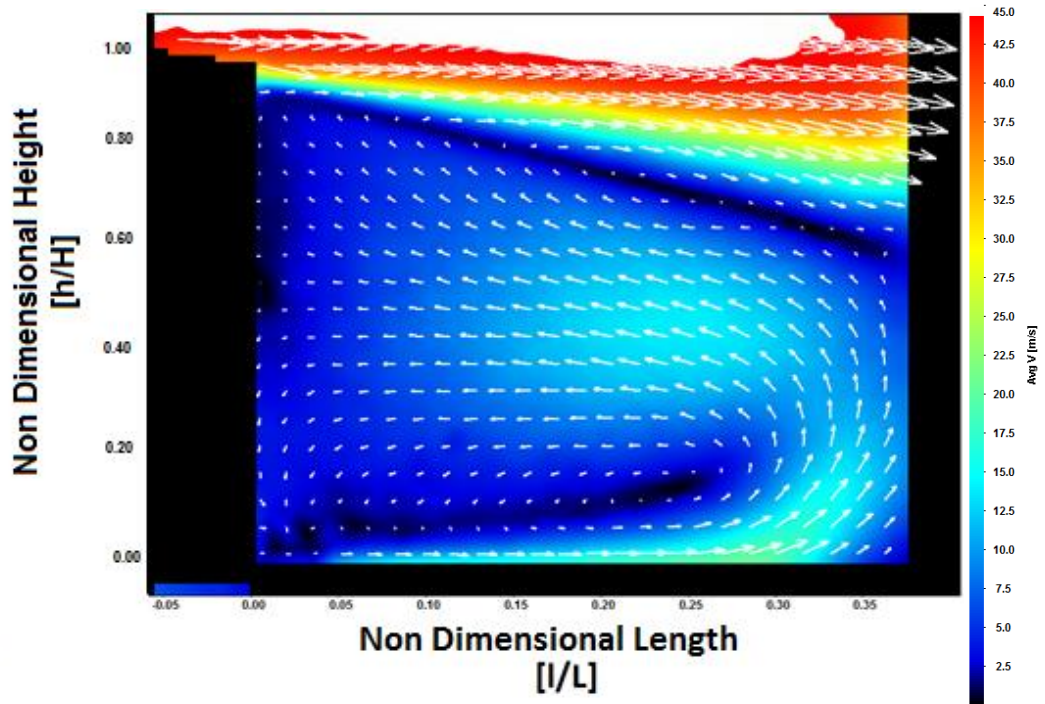


Figure 3.11 - Coefficient of drag vs chamfer angle with and without PIV equipment in place

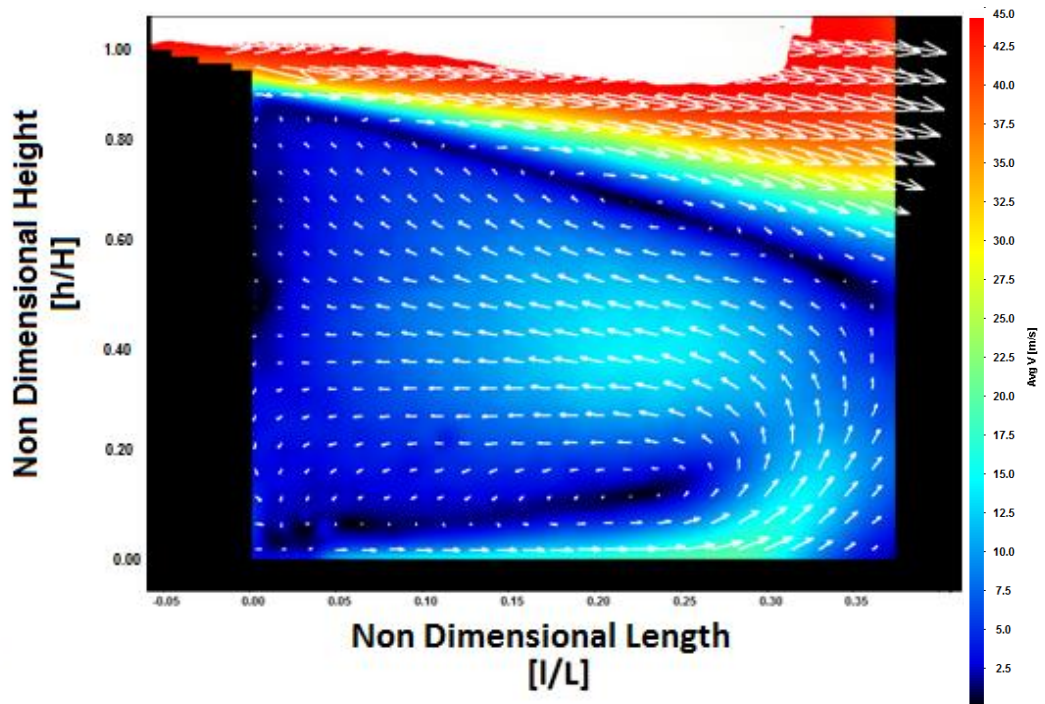
Figure 3.12 and Figure 3.13 show the time averaged vector array and streamline plots for the Squareback, 4°, 12° and 20° chamfer configurations. The vector and streamline concentrations have been reduced by 1/4 in the stream-wise axis and 1/2 in the vertical axis compared to the computed images. This reduction is to aid clarity in the format presented here, however detailed vector magnitudes may become more difficult to identify so velocity magnitude is plotted in the background in the form of a contour plot. The rear section of the model is shown as a solid black silhouette and X=0 is at the model base plane.



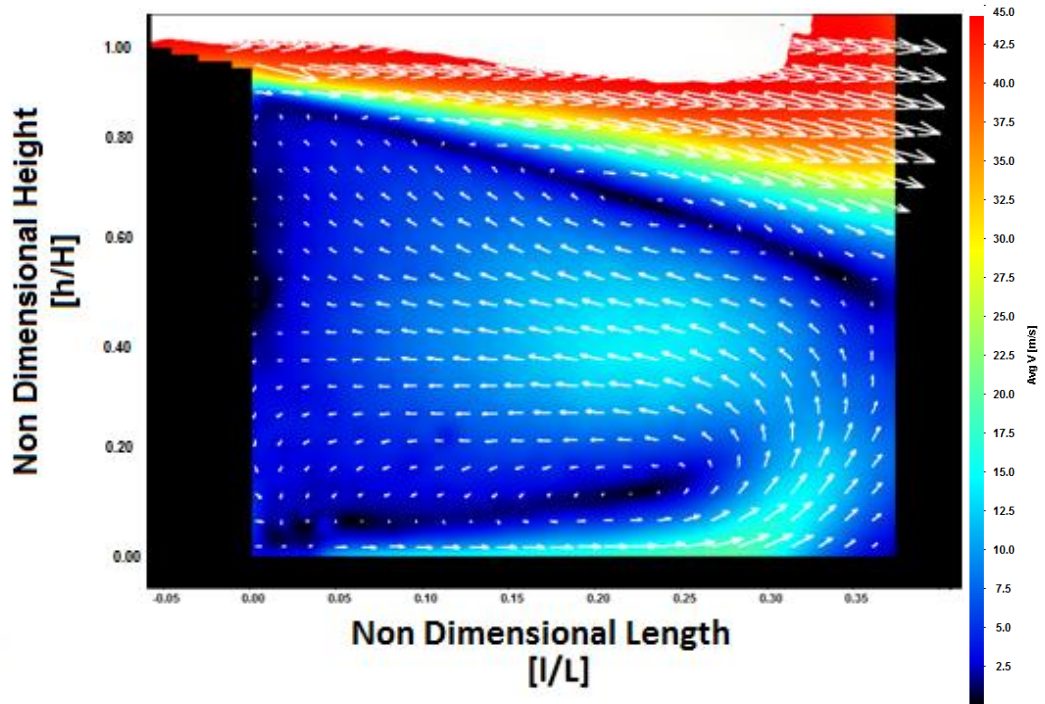
a) Squareback



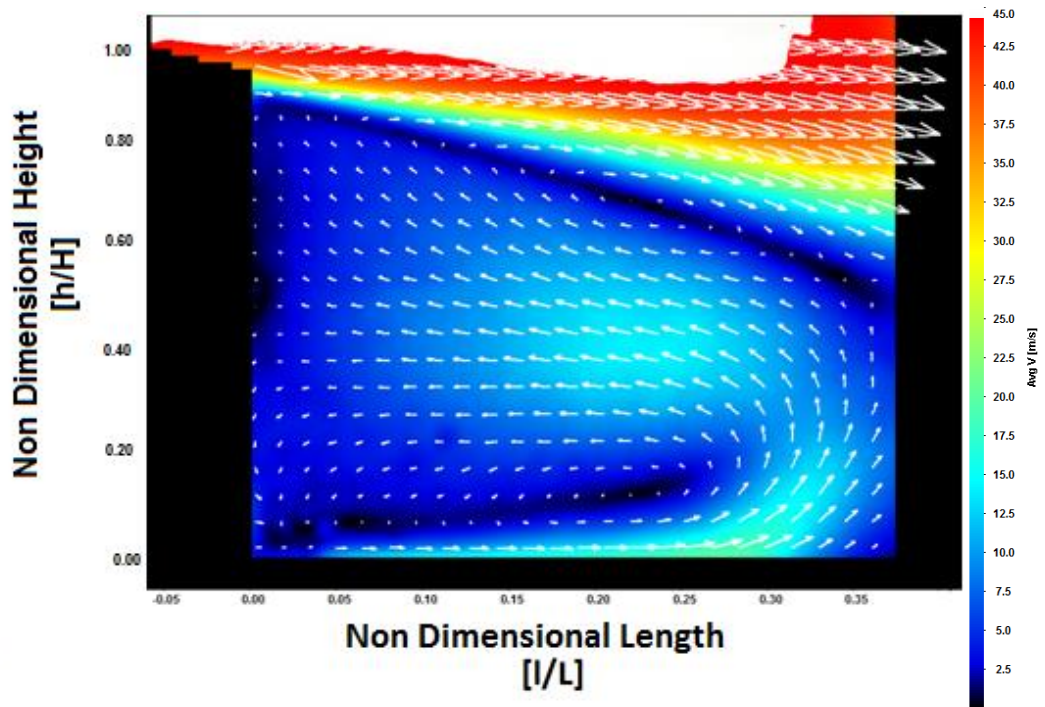
b) 4° chamfer



c) 8° chamfer



d) 12° chamfer



e) 20° chamfer

Figure 3.12 - Time averaged PIV vector plots for: a) square-back; b) 4° chamfer; c) 8° chamfer; d) 12° chamfer and e) 20° chamfer

In each configuration the direction and magnitude of flow in the wake region is dominated by an upwash flow from underneath the model. This upwash creates a large recirculation region in the lower wake. The high momentum overbody flow does not appear to recirculate and mix as significantly with the base region as is the case with the underbody flow. Instead the overbody flow separates and moves downstream away from the body, creating a large amount of shear between it and the upwash in the wake. The interaction of the upwash in the wake flow and shear layer created by the overbody flow appear to feed into an upper vortex located downstream from the base of model. This upper vortex and the overall structure of the wake can be more clearly identified in the streamline plots of Figure 3.13.

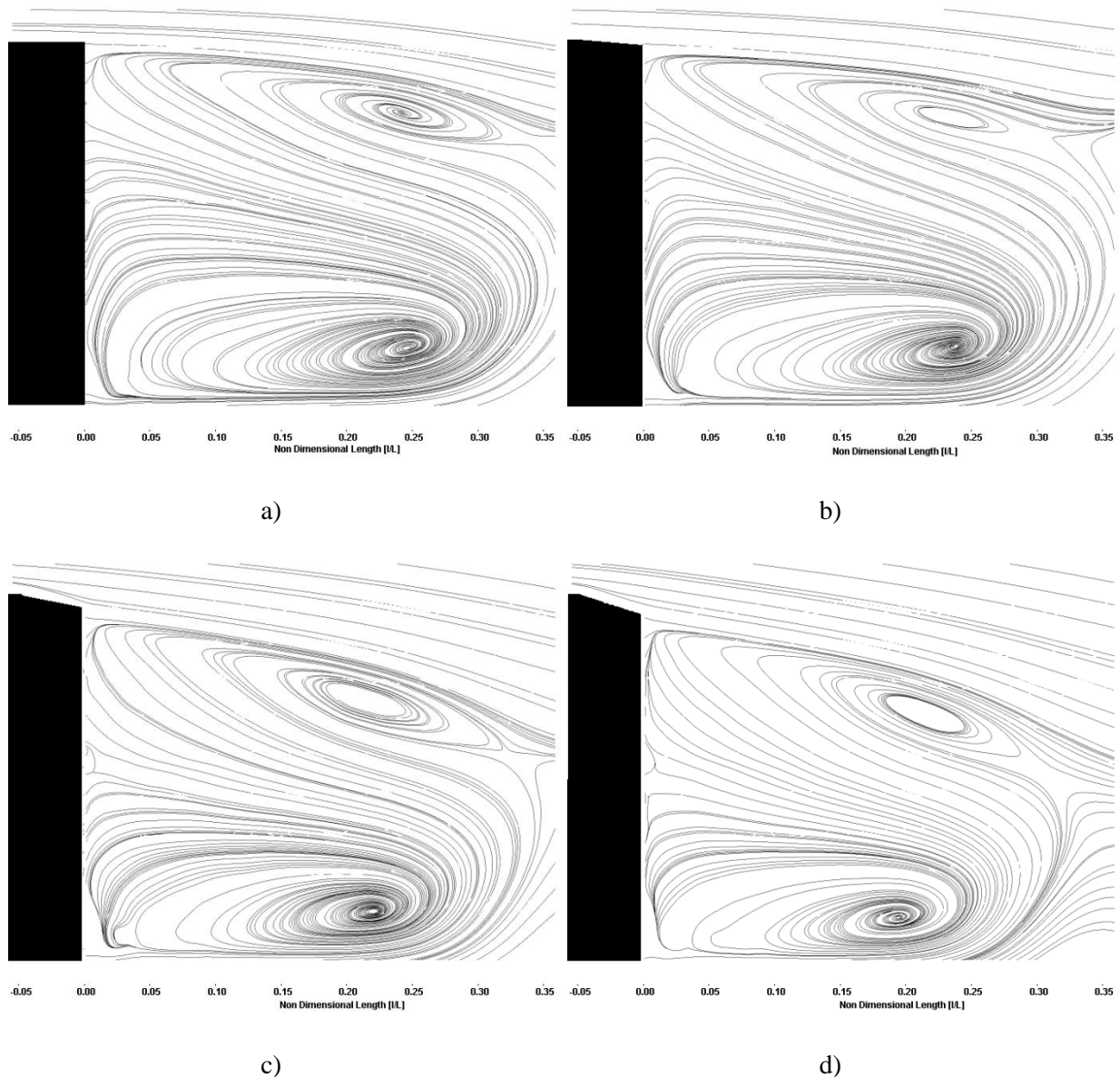


Figure 3.13 - Time averaged PIV streamline plots for: a) square-back; b) 4° chamfer; c) 12° chamfer and d) 20° chamfer

Figure 3.13 also clearly shows that the wake is dominated by the large recirculating region formed by the underbody flow. These images do not match with more symmetrical wake structures observed by previous authors using much more symmetrical box models at higher ride heights (Khalighi, Zhang and Koromilas, 2001). They do correlate well with the pressure contour plots seen in Figure 3.9, showing one large area of low pressure as a result of the large lower recirculation region, and other work using Square-back configurations at a proximity to the ground representative of real vehicle ride heights (Mason and Beebe, 1976). In addition to the low pressure region associated with the lower vortex it may have been expected to see a low pressure region where the upper vortex structure interacts with the base surface. However, further examination of the instantaneous PIV vector fields as well as the time averaged result may reveal why the corresponding low pressure region is not observed as clearly as the lower one.

The streamline plots also demonstrate the narrowing and shortening of the wake with increasing chamfer angle. In Figure 3.13a the centre point of the upper vortex is at $h/H \approx 0.9$, the stagnation point on the base of the model is at $h/H \approx 0.82$ and the end of the near wake region is not visible in shot but is estimated to be located at $l/L \approx 0.38$. As chamfer angle increases the upper vortex centre and base stagnation positions shift downwards, constricting the size of the lower recirculation region. This gradual constriction of the lower recirculation region with increasing chamfer angle can also be observed in the C_p contour plots of Figure 3.9 and the added rotation in the upper shear layer is consistent with the increasing lift seen in Figure 3.8. For the 20° chamfer the upper vortex centre and base stagnation positions have moved to $h/H \approx 0.78$ and 0.63 respectively, and the end of the near wake is visible at a position of $l/L \approx 0.32$. These images illustrate a surprisingly large modification of the overall wake size with a relatively small, high aspect ratio chamfer.

While the structures described above appear well defined in the time averaged flow fields it is much more difficult to identify them in the instantaneous images. Figure 3.14 shows some example instantaneous vector fields in the Square-back configuration, containing enlarged vector arrows with streamline plots in the background. In practice the upwash flow in the base can be clearly identified in approximately 50% of the instantaneous images but the upper vortex is far less regular. Instead non-discrete, time independent vortex shedding appears to occur, which may also contribute to the formation of the upper vortex seen in the time-averaged field. It is also clear that the upwash flow in the wake and overbody free stream shear layer interact to supply rotational energy for the formation of the time averaged upper vortex structure. However its strength cannot be seen in the instantaneous plots and the clearly defined vortex formation seen in the time averaged plots may simply be a feature of the averaging of the random shed structures in the instantaneous images. This may be why a

clearly defined low pressure region associated with the upper vortex cannot be easily identified in the upper base pressure measurements.

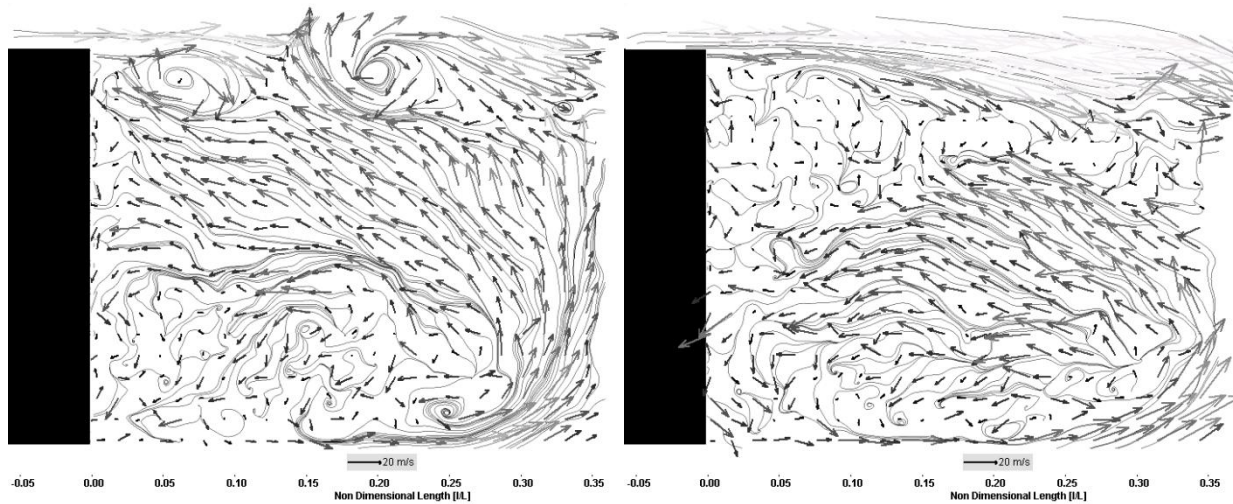


Image 15/1000

Image 40/1000

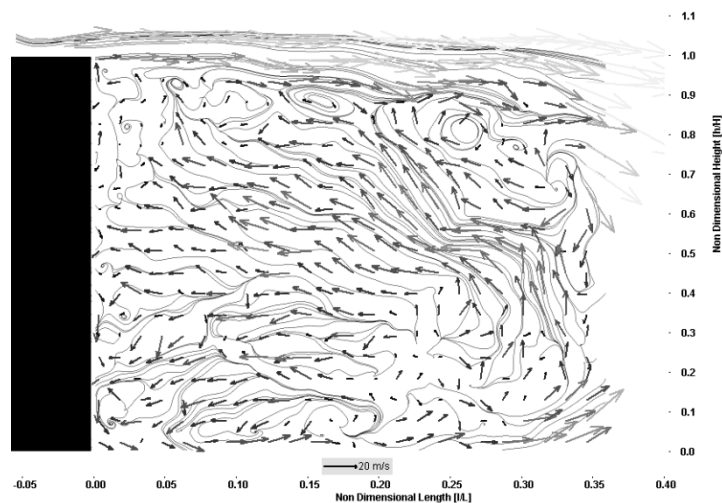


Image 59/1000

Figure 3.14 - Example instantaneous PIV images of the Square-back configuration showing vector arrows and streamlines in the background

The indiscriminate occurrence of these vortices in the instantaneous images leads to the description of the roof trailing edge shedding process as a Markov Chain. Markov chain theory suggests that future states (i.e. the next flow field or future instantaneous image, and the existence of shed vortex structures within them) depend only on the present state and not historic states. The transition from the current state to a subsequent state is determined by random chance and transition probability factors (Ching and Ng, 2006).

The implication is that in the roof trailing edge separation process, shedding may occur at a finite wavelength for a number of time steps, but then fade away, or even vanish for a subsequent, random number of time steps. Examples of potential transition probability factors that may have an influence on the formation of the shed vortices may be the shear layer and upwash interaction in the current state, or the transport of pressure fluctuations resulting from the shedding process propagating back upstream, generating vorticity fluctuations, and enhancing future shear layer roll-up.

If the flow is to be controlled via an active technology, such as synthetic jets, then the introduction of a regular additional energy source (in the form of an oscillating jet) may be considered as an additional transition probability factor. The repeated jet flow may lock onto a certain shed frequency, and drive a regular shedding pattern, which in turn would create a turning of the overbody flow downwards and into the wake.

However, Synthetic Jets along with most forms of active technologies require a power input, and so must create a sufficient drag reduction to outweigh their power demands and additional costs. It is also clear that if an active technology is to be applied to an un-optimized shape, the net drag reductions must be as big as that achieved with the simple application of a small chamfer such as the one used in the current work. Alternatively the application of active technologies and shape optimization could be combined to generate further savings.

3.4 Discussion and Implications for Further Work

A high aspect ratio roof trailing edge chamfer has been applied to a sharp edged, Square-back bluff body and balance, pressure and centreline PIV data acquired. The data provides a good benchmark case for the implementation of active flow control.

The optimum chamfer angle of 12° generates a significant drag savings of 4.4% (13 counts) and a reduction in C_d of 2.7% (8 counts) is achievable from only a 4° chamfer configuration.

The pressure data shows that the improvements in drag arise from the pressure changes on the rearward faces with the majority of the reduction attributed to base pressure recovery at low angles, with a progressively increasing drag contribution from the 3D effects as chamfer angle is increased. This is an encouraging result for the future implementation of active technologies with the aim of achieving similar base pressure recovery effects.

PIV results have highlighted the main structures within the wake of the model. The flow exiting the underbody forms a strong upwash and the overbody flow separates and moves downstream away

from the body, creating a large amount of shear that interacts with the wake to feed into an upper vortex set downstream from the base of the model. However this vortex is not clearly defined in instantaneous data and can be regarded as a very transient feature or perhaps even a statistical feature of the averaging process.

In general the instantaneous images of the flow field do not indicate a well defined time averaged wake structure. Instead flow structures that contribute to the formation of the time averaged pattern are present, but are not regular. The random roof trailing edge shedding is likened to a Markov chain. It is conjectured that probability of vortex structures occurring may be increased by the implementation of an active technology such as synthetic jet actuators.

The work so far has demonstrated how difficult it is to identify a regular set of shed structures from the rear edges of the model. However ‘shedding’ has been observed and it is conjectured that this process may be promoted or suppressed by active flow control to influence base pressures. In order to generate an active flow control experiment the actuators themselves must first be investigated. The next chapter will describe the investigatory work that was conducted to try and design an effective active flow control device, such as a Synthetic Jet or a pulsed jet.

Chapter 4

**ACTIVE CONTROL ACTUATOR
DESIGN AND TESTING**

4.0 Active Control Actuator Design and Testing

4.1 Introduction

A number of factors will determine how well and how efficiently an active flow control device (in this case some form of air jet) will be able to influence the external cross flow in question. Various investigations have described the requirements for formation of a jet, penetration length of jets, outlet velocity profiles and magnitudes of jets. In addition to how well a jet performs it must have the potential to be applied to a road vehicle, where additional criteria become introduced. Some of which are overall size and weight, energy conversion efficiency and cost. Due to the potential for compact sizes and low energy demands the Synthetic jet has been identified as a desirable technology to investigate.

Unfortunately a number of variables influence how well a synthetic jet will perform, and there is no such thing as a ‘common off the shelf’ solution. For this reason a bespoke synthetic jet arrangement must be designed and its performance in a simple test case assessed. This investigation will not only give an insight into the potential for synthetic jets to work in simple test cases but also highlight any potential problems if they are to be applied to more complex model testing or even scaled to full scale vehicles.

The oscillations that drive fluid in and out of a synthetic jet orifice are usually driven in one of three ways.

- Piezoelectrically driven diaphragms
- Electromagnetically driven pistons
- Acoustically driven cavities

Additionally the orifice that forms the outlet/inlet for the jet can be designed as either a slot or a circular hole. In each of the three drive methods, through either a slot or a hole, the formation of a jet is characterised by the separation and roll up of vortices which advect away from the orifice. If the so called ‘Acoustic Streaming Criterion’ (McKormick, 2000) (ASC) shown in Figure 4.1 is met the vortices will separate away from the orifice without significant interaction with the in-stroke phase of the process, and eventually decay to smaller length scales.

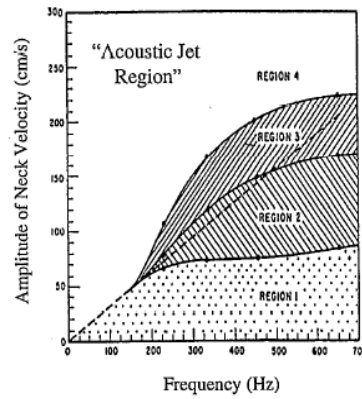


Figure 4.1 - Acoustic streaming criterion (McKormick, 2000)

The ASC illustrates that for low levels of excitation, fluid particles will move in and out of the orifice a small amount without mixing with particles outside of the orifice (regions 1 and 2). In region 3 significant turbulence is generated around the orifice and some acoustic energy is converted into mean fluid motion. In region 4, the “Acoustic Jet Region”, particle displacement extends well outside the orifice, allowing separation from the orifice exit and the roll up of vortices which advect away to form a jet (Figure 4.2). The vortex formation can create a pair of axisymmetric vortices (2D jet) in the case of a slot, or a circular axisymmetric ring vortex (3D jet) in the case of a circular hole.



Figure 4.2 - Synthetic jet with characteristic vortices (Glezer and Amitay, 2002)

Many authors (Holman and Utturkar, 2005), (Sharma, 2006), (Guo and Zhong, 2006), (Lockerby and Carpenter, 2004), (Kim and Gary, 2006) have conducted experiments and tried to create models of jet performance and vortex formation based on physical parameters of the orifice and cavity. The focus of most of the work is to ensure vortex formation occurs and the maximum amount of momentum is expelled in the outstroke for a given amount of input energy. For a jet in a quiescent medium a Reynolds number based on the momentum from the jet can be expressed in the form shown in Equation 4.1.

Equation 4.1
$$Re_{I_0} = \frac{I_0}{\mu b}$$

Where b is the jet orifice diameter or orifice width μ is the dynamic viscosity of the fluid and I_0 is defined by Equation 4.2.

Equation 4.2
$$I_0 = \rho \int_0^\tau \int_A u_j^2(\bar{x}, t) dAdt$$

where $\tau = T/2$, T is the time period of one phase of actuation and u_j is jet exit velocity at the orifice exit plane.

When using synthetic jets in crossflow it is of interest to define the momentum available from the jet in relation to the momentum in the crossflow. This can be defined by Equation 4.3 where L is a characteristic length scale of the model used, U_∞ is the freestream flow velocity and U_j is either the RMS or peak jet exit velocity.

Equation 4.3
$$C_\mu = 2 \frac{b}{L} \left(\frac{U_j}{U_\infty} \right)^2$$

When characterising a jet in this way the jet exit velocity U_j must be measured, and for jets with small orifice sizes it is usually measured using a CTA hot wire probe. In previous publications (Kim and Gary, 2006) synthetic jet actuators are found to have two peaks in performance, initially at the resonance point of the actuator, and then at the resonance point of the cavity. In order to design a synthetic jet for use in wind tunnel experiments on the afterbody of a simplified car model, initial tests using different synthetic jet designs were conducted.

4.2 Initial Testing

Two methods of driving a synthetic jet cavity were selected to carry out initial testing and investigations; loud speaker driven, and piezoelectric disc driven. A number of iterations of the design of the jets for high and low frequency actuation were produced. The majority of the initial designs used a 2 dimensional 1mm wide slot, as opposed to an individual hole or a row of holes. A slot was first selected to produce the simplest possible structures, as it forms a 2D jet and there is no need to consider inter-orifice interactions as may be the case with a row of holes.

4.2.1 Low Frequency Jet

The first tests were conducted using a high speed camera and smoke visualisation of a jet exiting from a 1mm wide slot, nominally 200mm long with a slot depth of 3mm. The slot was machined into a tube, and the cavity within the tube was driven by a 160mm speaker at one end. At low frequencies (30-75Hz) the roll up and advection of a pair of vortex rings could be clearly identified illustrating that the ASC had been met, and the setup could be legitimately defined as a Synthetic Jet. Figure 4.3 shows a single frame from the high speed footage with the rings highlighted.

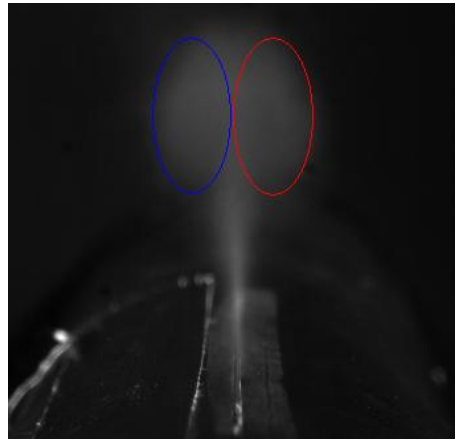


Figure 4.3 - Single frame from high speed camera images of synthetic jet at 50Hz

Additional images were taken with the camera at 90 degrees to the slot axis to investigate how homogeneous the jet exit profile along the length of the slot was. Interestingly at a drive frequency of 90Hz a standing wave was set up within the tube. This was observed whereby vortex rings could clearly be seen when the slot was viewed along its axis, but off axis a sinusoidal wave of smoke was observed.

Whether or not this wave would be detrimental to the flow control ability of a synthetic jet is unknown, however it would introduce an additional variable to any testing. Therefore it is noted that standing waves should be avoided in any actual tests on a wind tunnel model. The configuration described above used a single speaker at one end of the cylinder, and this would have increased the likelihood that this behaviour was created. For future designs asymmetry in the actuator positioning was avoided.

Exit velocity data was recorded using a CTA hot wire probe, placed at the slot exit plane as described in section 2.4 however the hot wire was calibrated in the Loughborough University wind tunnel for velocities between 5-40m/s as the Dantec calibrator was not available at this point. Figure 4.4, shows an extract from the measured velocity data for a jet driven at 50 Hz. The data shows that peak velocities were clipped at 40m/s, indicating that they were out of the calibration range. Future calibrations were made using a Dantec calibrator from 0-60 m/s to avoid this effect.

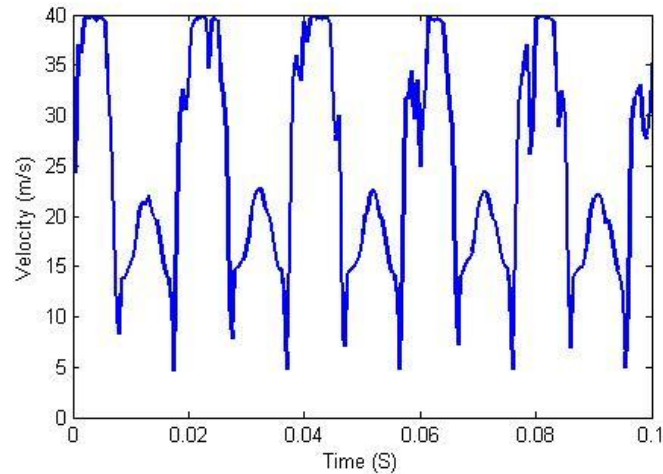


Figure 4.4 - 50 Hz small diameter cylinder

With the intention of being able to place the cylinder in a cross flow at a later date consideration was given to the Reynolds numbers that would be achievable in these later tests. It was decided that to attain larger Reynolds numbers at lower freestream velocities the outer diameter of the cylinder would need to be increased. Being able to achieve higher Reynolds numbers at lower freestream velocities would potentially offer the ability to generate higher momentum coefficients for a given jet outlet velocity.

In addition to the overall size increase a second speaker was added at the opposite end of cylinder to avoid the standing waves discussed earlier. Figure 4.5 shows an extract of the new measured velocity profile at the outlet of the slot and it is noticeable that the peak velocities are lower than that of Figure 4.4. This is due to the fact that the cavity of air that was driven to produce Figure 4.5 was larger than in the initial setup. Unfortunately this means that the momentum coefficients achievable will now be reduced, and the benefits potentially gained from reduced freestream velocity have been negated.

It can also be seen that the graph is much smoother; this could be due to the fact that there were secondary harmonics present in the first setup.

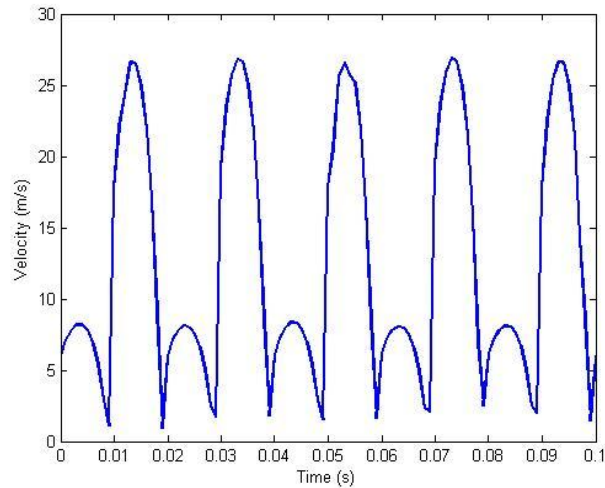


Figure 4.5 - 50Hz 200mm OD cylinder

In both cases there is a large peak and a smaller peak; the large peak is the velocity measured on the outstroke and the smaller peak is the velocity on the in stroke. Both peaks are positive because of the insensitivity of the hot wire to direction. The difference in magnitudes for each stroke can be explained by the fact that on the outstroke the flow is very unidirectional, with a high velocity moving directly upwards past the hotwire. During the in stroke air is pulled down into the slot from different regions around the periphery of the slot, accounting for the reduction in measured velocity.

4.2.2 High Frequency Jet

In order to produce jets at higher frequencies much smaller cavities were designed and the cavities were tuned in order to be driven at resonance. Two sizes of cavity were produced (Figure 4.6) and two methods of drive were tested; piezoelectric discs, and miniature mylar speakers.

The peak velocities were achieved driving the larger of the two cavities at around 1800Hz using the piezoelectric discs, where velocities of up to 24m/s were recorded. An additional peak in performance was found at around 650Hz with recorded velocities of up to 19m/s. This trend is in agreement with the work of Kim and Gary (2006) where the lower peak is associated with actuator resonance and the larger peak is the cavity resonance. Although using resonant frequencies to achieve larger peak velocities is practical when in a quiescent medium, it becomes more difficult in a cross flow. The cross flow adds an additional neck length correction to the resonance calculations and shifts the resonance point up to a higher, freestream velocity dependant, unknown frequency. When using lower frequencies and a speaker as a driver, the cavities were not tuned for resonance and velocities of a similar magnitude were achieved.

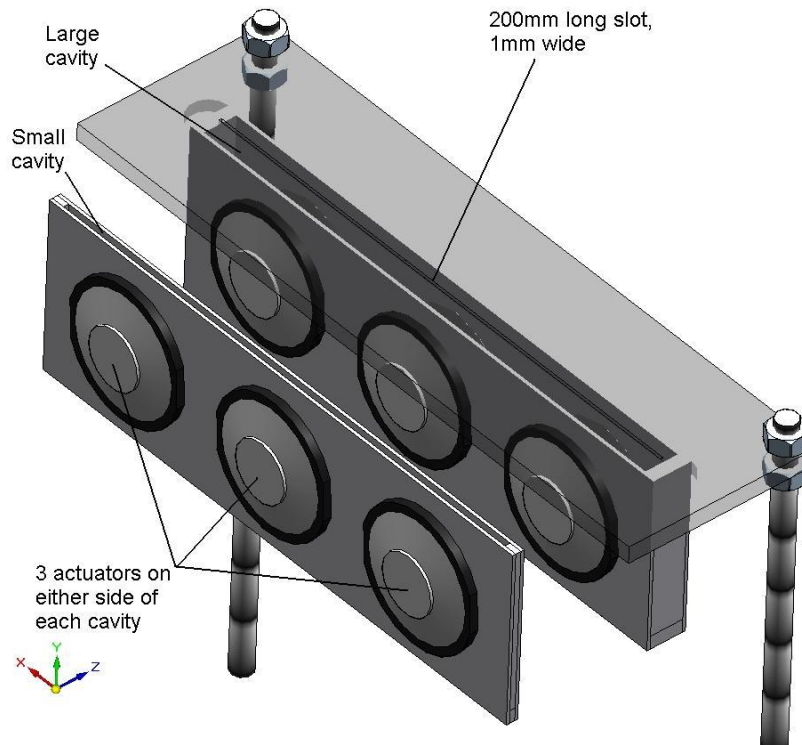


Figure 4.6 - Schematic of high frequency jets

After the initial testing it was decided to pursue the use of acoustic speakers to drive the synthetic jets, as higher peak exit velocities will be attainable, without the necessity to use resonant frequencies. A study was also conducted in conjunction with a Masters student (Laura Plackett) where high speed PIV and Laser Doppler Anemometry (LDA) measurements were taken on a ‘speaker driven’ synthetic jet setup and a pulsed jet.

4.2.3 PIV and LDA Analysis of ‘Speaker Driven’ Synthetic Jet and Pneumatic Pulsed Jet

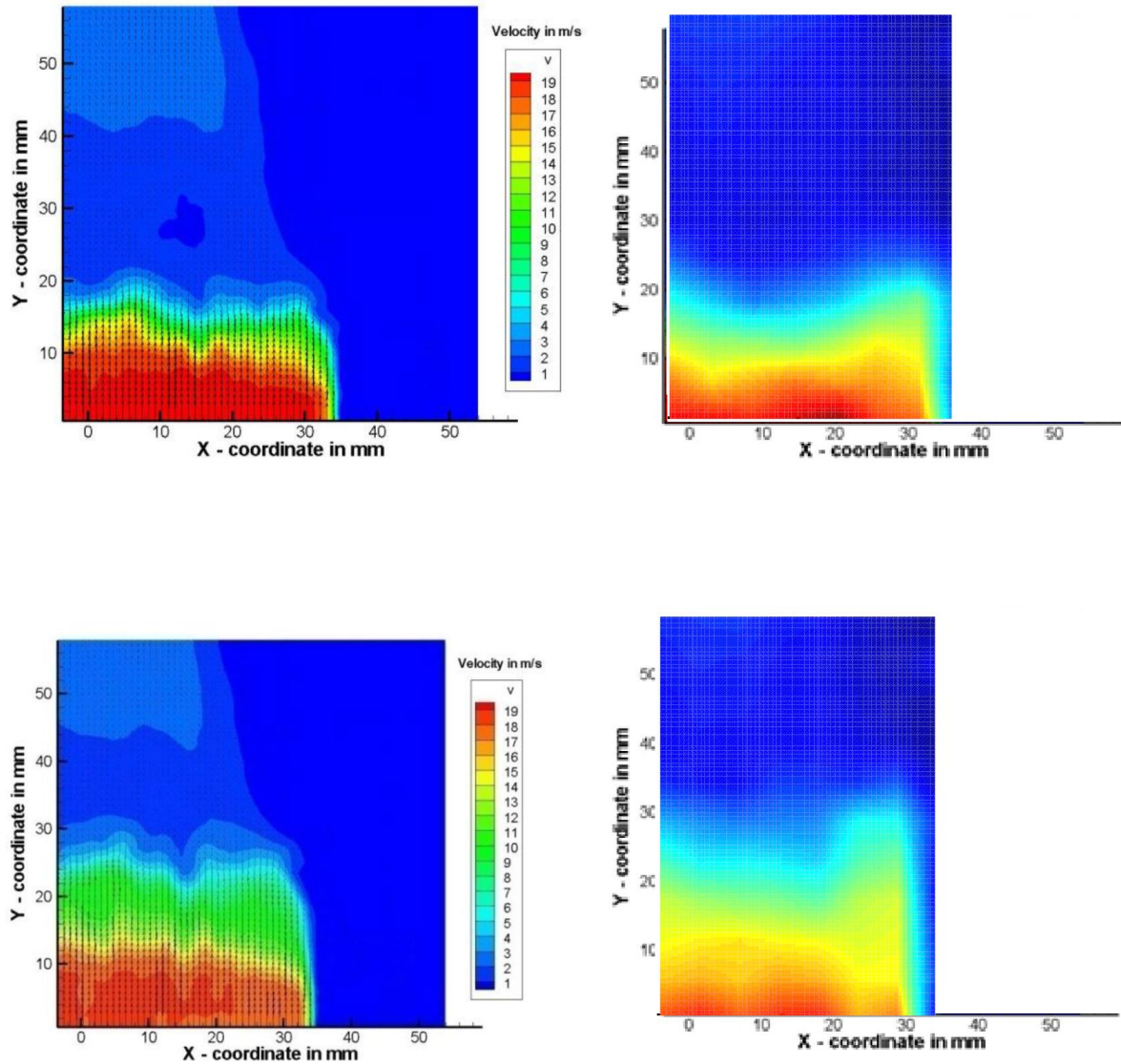
The aim of this work was to try to ensure that the 1mm wide slot configuration that has been designed would produce a uniform 2D jet that also produces the characteristic symmetric vortices seen in SJ flows. It was also of interest to investigate how the jet exit velocity decayed with time and distance from the jet orifice to try to estimate how well a jet might influence any cross flow that is intended to be controlled. A small stand alone rig was developed to be used in conjunction with a time resolved PIV setup (Figure 4.7) which incorporated a feed into the cavity to supply seeding (Figure 4.7). A similar rig was developed for a pulsed jet that was driven from a pneumatic supply and controlled by a valve.



Figure 4.7 - Speaker driven SJ rig for time resolved PIV studies

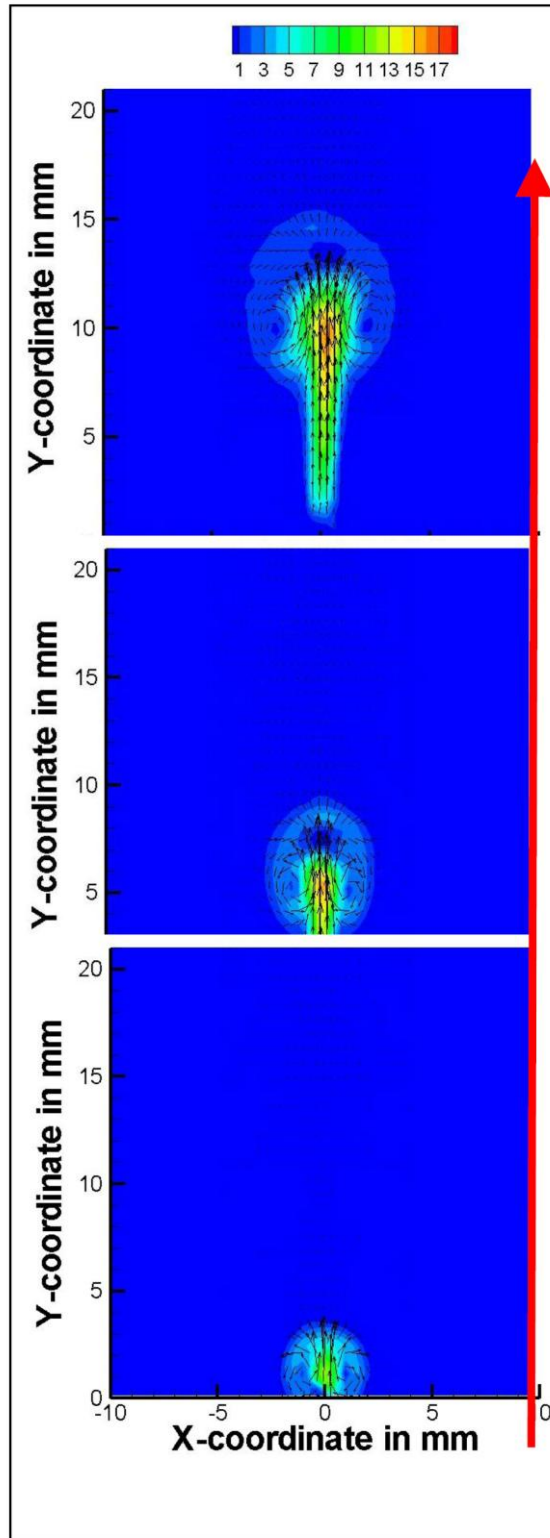
PIV and LDA measurements were taken viewing along the axis of the slot and also perpendicular to the slot axis. Because of the cyclic nature of a pulsed and synthetic jet the measurements were conducted by phase locking the acquisition to various time steps in the jet cycle. The data for each time step is then phase averaged and the phase averaged measurements at all the available time steps are combined to create a phase averaged flow cycle.

Figure 4.8 shows PIV and LDA plots of velocity magnitude for one half of the SJ viewing perpendicular to the slot exit. The two measurement techniques show good correlation at both the time steps shown and also show a relatively uniform velocity profile along the length of the jet. The phase averaging will smooth any instantaneous fluctuations of velocity along the slot length. It is the case that larger fluctuations can be observed at the end of the slot where edge effects become prominent however across the majority of the slot width the flow is uniform. In both cases it can be seen that the peak exit velocity reaches 19m/s, which is lower than that measured with the hotwire in the previous measurements, however the speaker and cavity configurations are also different which explains the reduced velocity.

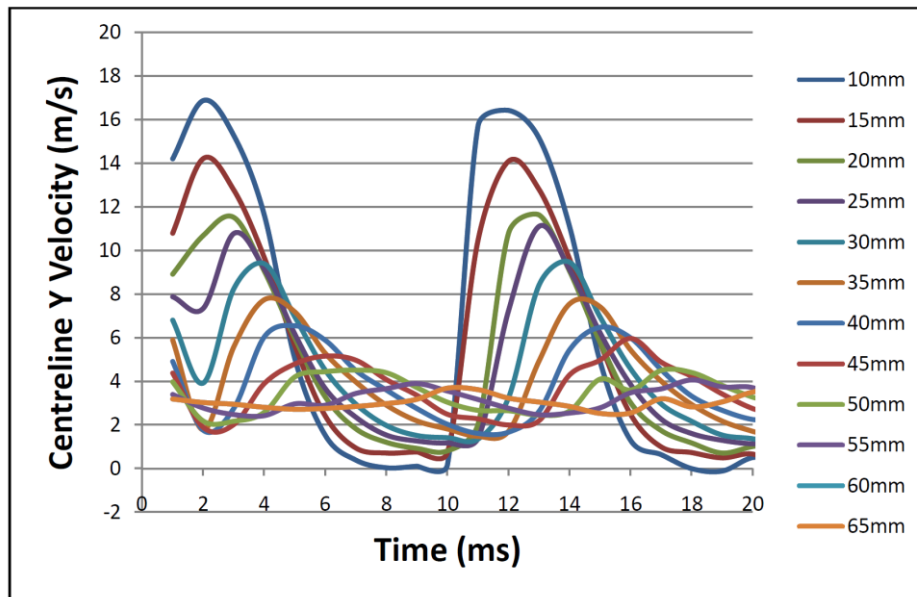


4.8 - Phase averaged PIV (left) and LDA (right) measurements of the 50Hz SJ centreline at time steps of 2ms (top) and 5ms (bottom) viewed perpendicular to the slot axis (Plackett, 2009)

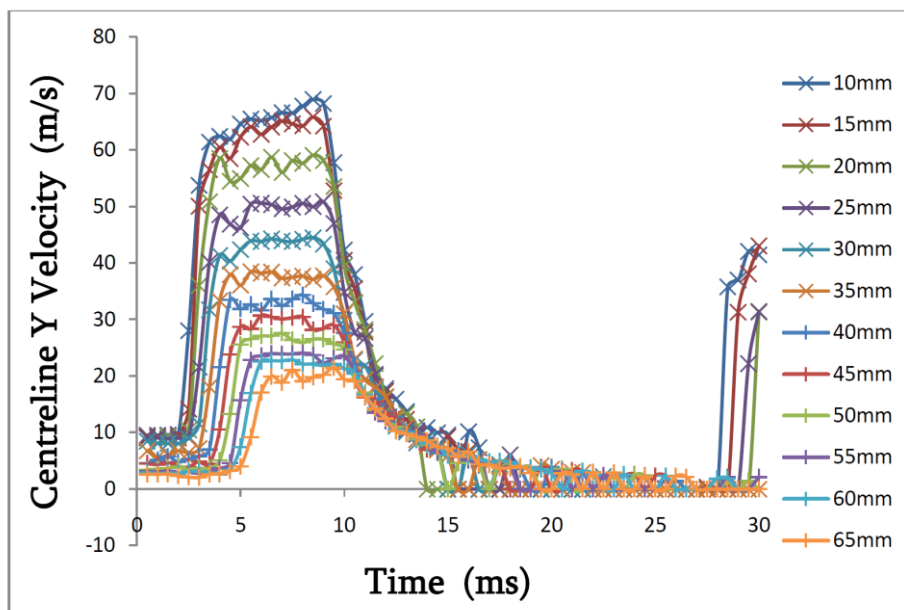
In order to observe the formation of vortices by the jet a view was taken down the axis of the slot and the evolution of the SJ from time 2ms to 6ms can be seen in Figure 4.9. Fluctuations in the symmetry of the jet about the $X=0$ centreline were again observed in the instantaneous images and this has been somewhat smoothed by the phase averaging of the measurement but the data still gives a good indication of how the pair of contra rotating vortices are formed and how the jet evolves and penetrates the quiescent air. It is believed that the penetration length of a jet or the rate at which it decays to smaller length scales can have an influence on how effectively it is able to control a cross flow. Figures 4.10 and 4.11 show centreline velocity profiles vs time for an SJ and a pulsed jet respectively and these plots can be used to investigate the penetration of the two jets into the quiescent air.



4.9 - Phase averaged PIV data of 50Hz SJ viewing along the slot axis at time steps of 2,4 and 6ms



4.10 - Velocity vs time plot for the centre line of the SJ running at 50Hz acquired using LDA (Plackett, 2009)



4.11 - Velocity vs time plot for the centre line of the pulsed jet running at 5Hz acquired using LDA (Plackett, 2009)

From Figure 4.10 and Figure 4.11 it can be seen that the peak velocities available from the pulsed jet are significantly higher and the velocity at a downstream location of 65mm is still ~20m/s. In the case of the SJ the peak velocities are much lower and at a downstream location of 65mm the velocity has decayed to ~4m/s. The fact that there is no in-stroke present in the impulsively started jet may have an influence on this but if the ASC has been met then this should be negligible. One of the main observations during testing was that the pulsed jet was a far more flexible device than a speaker

driven SJ. For example the actuation frequency of 5Hz used in the pulsed jet application could not be achieved by the speaker used in the testing because the speaker could not be driven at this frequency without risking damage to the coil. However it is not known if the in stroke is part of the mechanism that controls the flow and for this reason it was decided that testing using some form of SJ should be continued using as wide a range of momentum coefficients as possible on a simple flow case.

4.3 2D Cylinder Testing

4.3.1 Experimental Setup

Before any testing on an automotive bluff body is conducted it is important to verify that the synthetic jets are behaving as expected and performing as reported in previous work. The flow structures found around a 2D cylinder are well documented with shedding structures and their associated frequencies being relatively predictable. The natural shedding frequency of a cylinder can be predicted using the Strouhal number and is calculated using Equation 4.4 where f is a characteristic frequency, L is a length scale (such as cylinder diameter) and V is the freestream velocity.

Equation 4.4
$$St = \frac{fL}{V}$$

The new model that was manufactured used two 160mm speakers mounted in either end of a 200mm diameter tube. A 200mm long 1mm wide slot was machined into the wall of the tube perpendicular to its surface, and two endplates were fitted. Two end plates were fitted to try to limit influences from the floor boundary layer and the end of the cylinder itself. The cylinder was fitted with 60 surface mount pressure tappings in a spiral pattern around its circumference and connected to a high speed 64 channel DTC scanner and CANdaq control unit as described in Section 2.3. A gap of 50mm was left between the end plates and first tapping so that the data recorded was also in a region where the end plate would have less influence on the flow over the cylinder and it would be as two dimensional as possible.

The model was mounted to the six component balance in the Loughborough University wind tunnel with the slot at an azimuthal position of 107° relative to the free stream direction. A photograph of the experimental setup is shown in Figure 4.12 and a close up of the slot showing the tapping positions is shown in Figure 4.13. The acoustic cavity of the jet was not tuned to be driven at resonance.



Figure 4.12 - Cylinder rig setup in Loughborough University wind tunnel

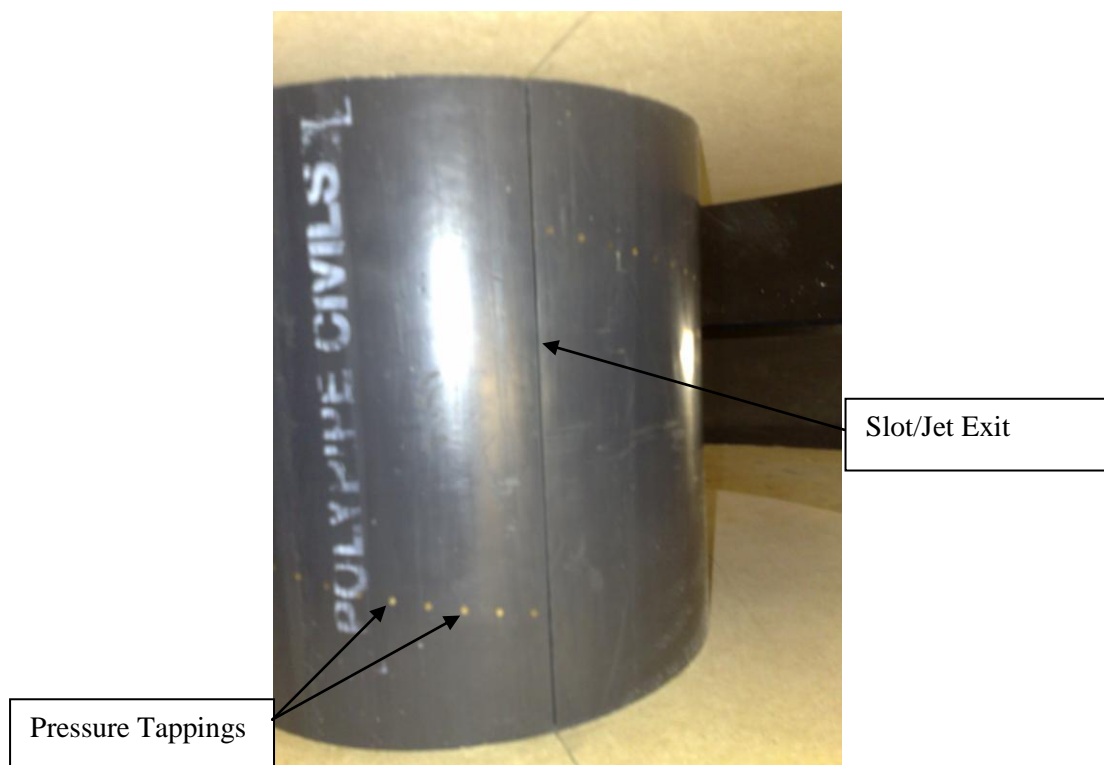


Figure 4.13 - Close up of jet exit and pressure tappings

The tunnel was run at speeds from 10m/s to 35m/s and measurement were taken at 5m/s intervals, giving diameter based Reynolds numbers of 1.48×10^5 to 5.19×10^5 . At each tunnel speed the jet actuator was run at 40Hz to 110Hz and measurements were taken at 5Hz intervals. The natural shedding frequency of the cylinder at the various freestream velocities, based on a Strouhal number (St) of 0.22, is given in Table 4.1. In reality the Strouhal number is not going to be absolutely 0.22 for all the test velocities, as it will vary with Reynolds number as per Figure 4.14. In addition to varying with Reynolds number it is known that the Strouhal number also varies with cylinder conditions such as, surface roughness and end conditions.

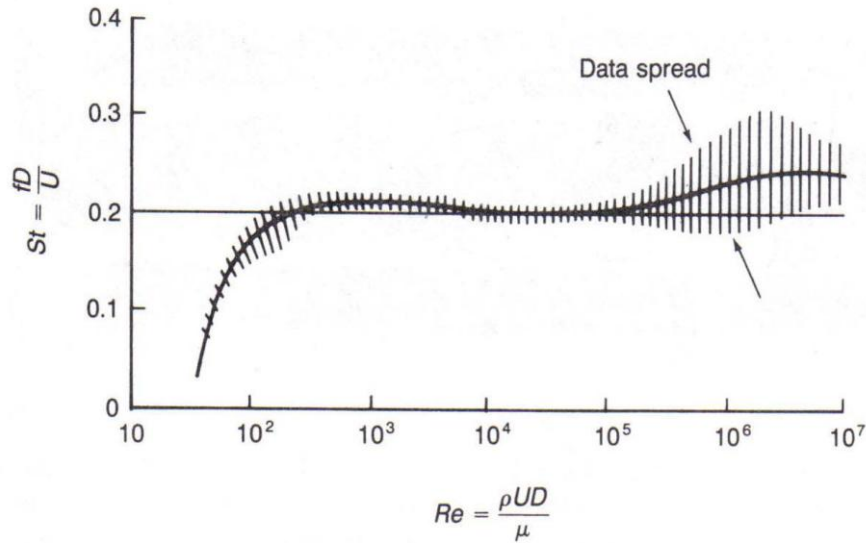


Figure 4.14 - Variation of Strouhal number with Reynolds number for flow around a cylinder (White, 1991)

Freestream Velocity (m/s)	5	10	15	20	25	30	35
Shedding Frequency (Hz)	5.5	11	16.5	22	27.5	33	38.5
Table 4.1 - Natural shedding frequencies of tube model at various freestream velocities							

4.3.2 Results; Pressure Measurements

Figure 4.15 to Figure 4.19 show the variation in pressure coefficient (C_p) around the cylinder for tunnel speeds of 10m/s, 15m/s, 20m/s and 25m/s corresponding to diameter based Reynolds numbers of 1.48×10^5 , 2.22×10^5 , 2.96×10^5 and 3.70×10^5 respectively. Each plot should be regarded as a different type of experiment with laminar, transitional, transitional/turbulent and fully turbulent boundary layer conditions. The Reynolds numbers where transition is thought to occur match well with published work on boundary layer transition around a cylinder (Brazaa, Perrina and Hoarau, 2006) (Roshko, 1961). Each plot shows the variation of pressure coefficient (C_p) without actuation and the slot open, without actuation but with tape covering the slot and with actuation at the various frequencies.

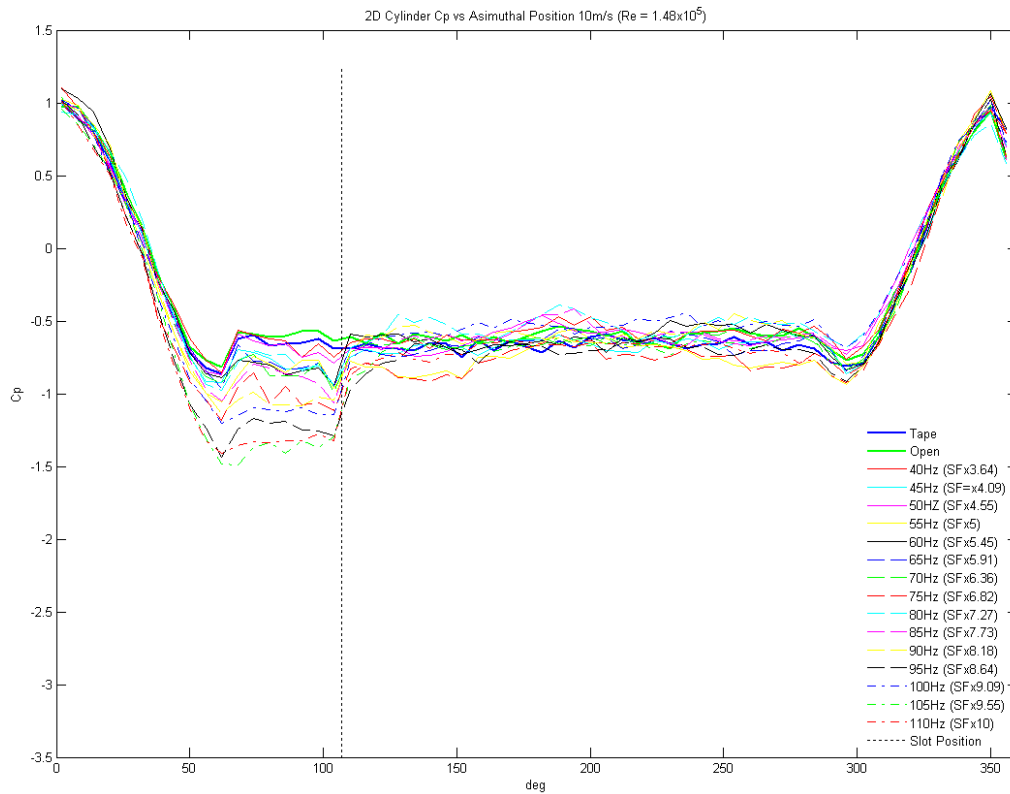


Figure 4.15 - Coefficient of pressure around 2D tube at $Re = 1.48 \times 10^5$ (Laminar)

For the un-actuated cases shown in Figure 4.15 and Figure 4.16 a suction peak can be seen at $\theta \approx 62^\circ$ with a separation at around $\theta \approx 72^\circ$. At a freestream Reynolds number of 1.48×10^5 (Figure 4.15) and with the jets running at 40-50Hz the separation point is largely unaffected, however when the jets are run at 55-110Hz the suction peak is widened significantly and separation is delayed until $\theta \approx 110^\circ$. This result agrees with the findings of (Glezer and Amitay (2002) where a jet placed at $\theta \approx 110^\circ$ on a cylinder in laminar flow delayed the point of separation until $\theta \approx 120^\circ$.

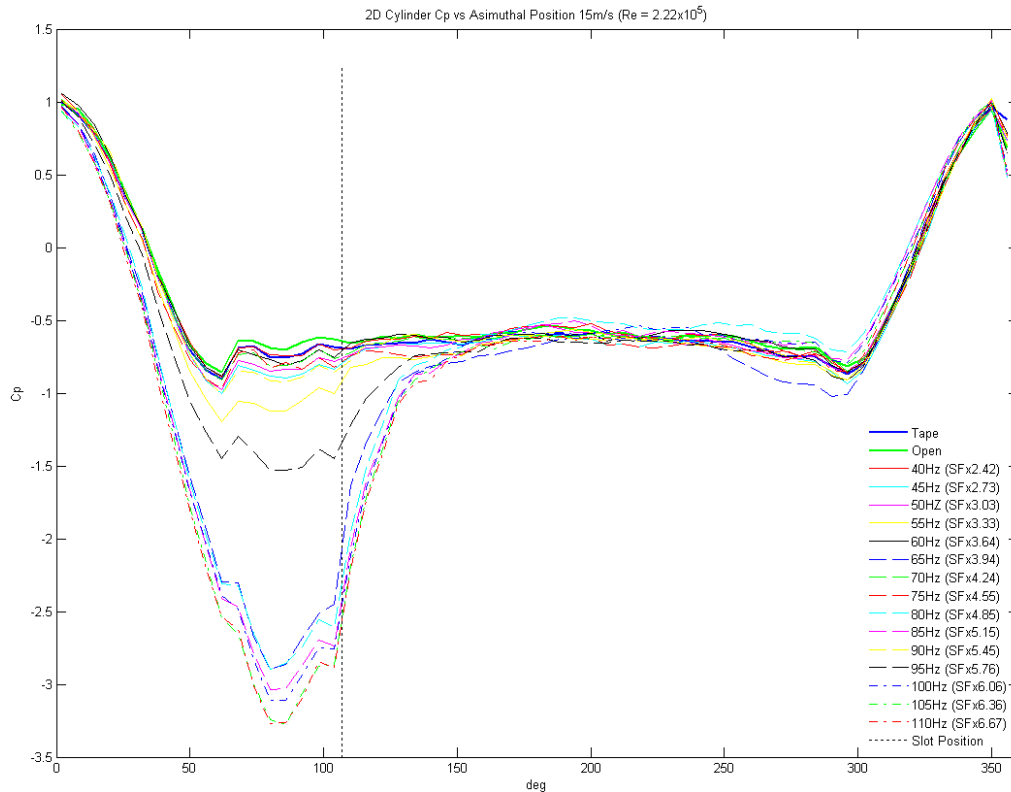


Figure 4.16 - Coefficient of pressure around 2D tube at $Re = 2.22 \times 10^5$ (Transitional)

For a freestream Reynolds number of 2.22×10^5 (Figure 4.16) and actuation frequencies of 40-50Hz the jet again has little effect on the flow, however at an actuation frequency of 55Hz a widening of the suction peak and a delay in separation until $\theta \approx 110^\circ$, as seen in Figure 4.15 occurs. Higher frequencies create a large increase in the depth of the suction peak from an unactuated peak at $C_p = -0.9$ to $C_p = -3.2$ at 105Hz and 110Hz, and separation is also delayed further to $\theta \approx 135^\circ$. Not all of the higher frequency range produces such good flow modification performance with frequencies of 70, 75 and 90Hz having little or no effect on the flow. The poor performance may be related to the jet frequency being matched with the natural shedding frequency of the cylinder or multiples thereof, however no correlation is seen. This anomaly is discussed further in section 4.4.

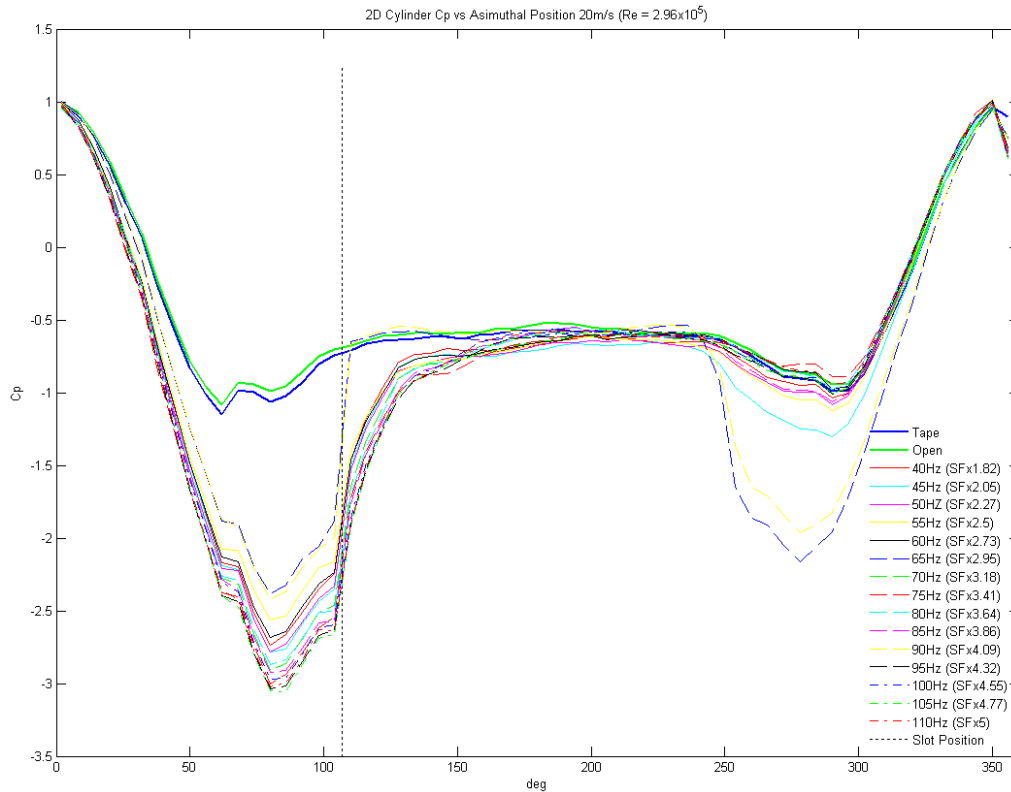


Figure 4.17 - Coefficient of pressure around 2D tube at $Re = 2.96 \times 10^5$ (Transitional/Turbulent)

The un-actuated flow at a Reynolds number of 2.96×10^5 (Figure 4.17) separates at $\theta \approx 110^\circ$, signifying a shift to a turbulent boundary layer separation regime. For all the actuated cases at all frequencies there is a large increase in the depth of the suction peak and separation is delayed until $\theta \approx 135^\circ$. This increase in performance may be attributed to the fact that the slot position now correlates with the point of the un-actuated flow separation, meaning that the specific actuation frequency used is not as important. In the previous cases the pressure distribution around the un-actuated side of the side of the cylinder has remained largely unaffected, but in Figure 4.17 for frequencies of 45, 65 and 90Hz a large suction peak is created on the un-actuated side of the cylinder. This effect on the un-actuated side of the tube may be a result of the suction stroke of the synthetic jet pulling flow around the back of the tube, as was found in previous publications (Glezer and Amitay, 2002) using a jet at $\theta \approx 120^\circ$ (Figure 4.18), and as discussed further by Béra et al. (2000).

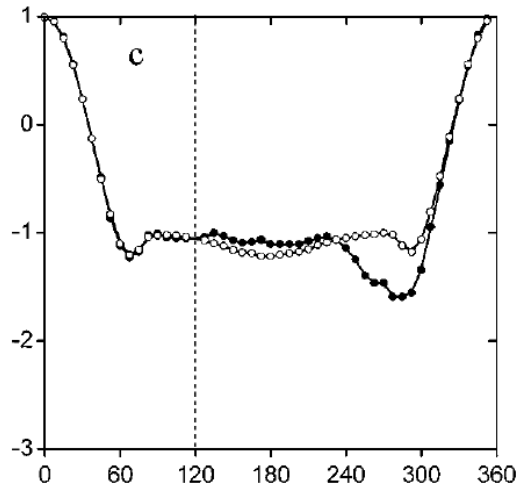


Figure 4.18- Variations of C_p on a tube with a synthetic jet at $\theta=120^\circ$
 (\circ) baseline and (\bullet) actuated (Glezer and Amitay, 2002)

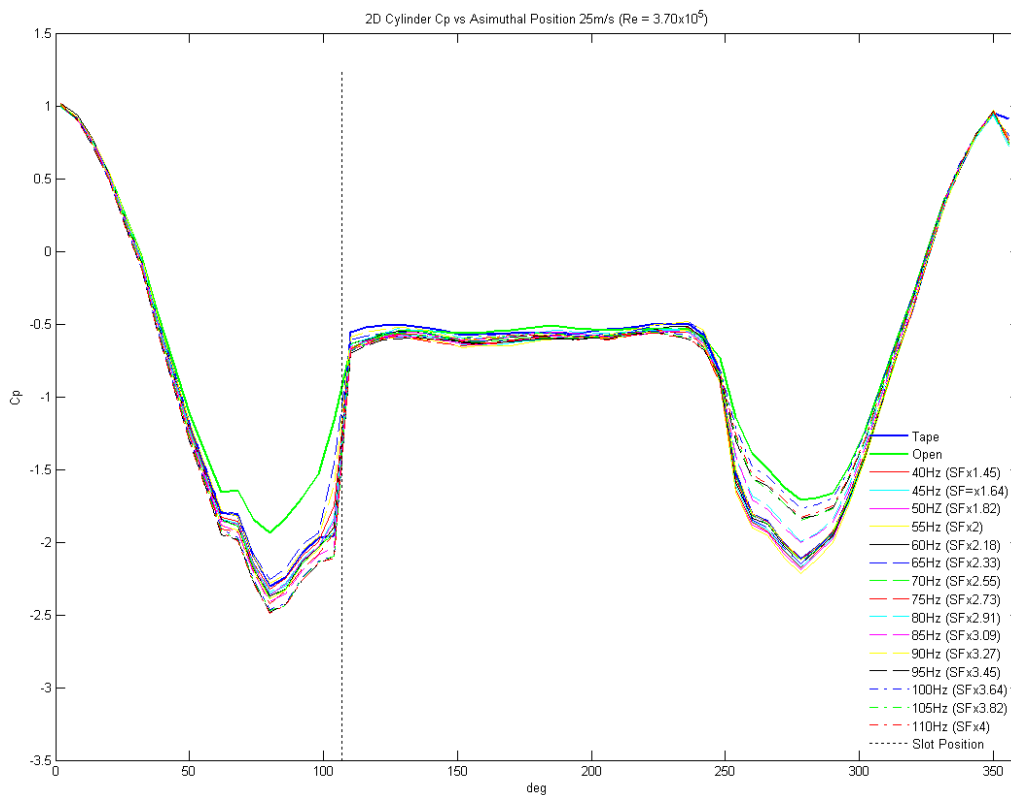


Figure 4.19 - Coefficient of pressure around 2D tube at $Re = 3.70 \times 10^5$ (Fully Turbulent)

For a Reynolds number of 3.70×10^5 (Figure 4.19) the un-actuated flows display a very clear turbulent separation at $\theta \approx 110^\circ$. When the synthetic jet is running none of the actuation frequencies displace the separation point further around the tube as found in Figure 4.16 and Figure 4.17. While it is possible that this result demonstrates that the synthetic jets are not effective at higher Reynolds numbers it may

also be that the result arises because the C_{μ} is insufficient at the higher tunnel speed. A change in tunnel speed from 20m/s to 25m/s gives rise to a 33% fall in C_{μ} . This later conclusion is supported by a comparison of Figure 4.19 with Figure 1.27 showing similarities to that of the low momentum jet performance discussed by Béra et al. (2000). Pressure plots at higher freestream speeds show no effect at all from actuation at any frequency.

4.4 Results; Balance Measurements

The force produced by the modification of the pressure distribution around the cylinder will create a lift (or side force if viewed in the orientation as setup in the wind tunnel (Figure 4.12)) on the side of the suction peak. A delay in separation will give a reduced wake size and increase in base pressure on the tube leading to a drag reduction.

Figure 4.20 and Figure 4.21 show the C_d and coefficient of lift (C_l) for freestream velocities of 15m/s, 20m/s and 25m/s. The overall magnitudes of the forces measured on the model were affected by the end conditions found at the periphery of the slot and outside of the endplates. This effect is unavoidable in order to package the actuators and endplates, however both C_l and C_d were non-dimensionalised by a reference area associated with the ‘actuator effected region’ of the model, (slot length x tube diameter).

C_d for the three cases all see a slight reduction as actuation is applied, but the 15m/s case (transitional boundary layer) shows very unreliable performance. The same behaviour was seen in the pressure distribution (Figure 4.16) and again no correlation is seen between performance at specific actuation frequencies relating to a shedding frequency. It is also noticeable that peaks and troughs in performance at the different actuation frequencies measured on the balance do not correlate with the peaks and troughs found in the pressure measurements (balance and pressure measurements were taken at separate points in time, during different wind tunnel runs).

It is believed that the reason for unreliable performance is because the boundary layer is in a transitional regime. In an un-actuated case the point of separation is shifting forwards and backwards in an unsteady nature. When actuation is applied sometimes the actuation can lock onto, or couple with the flow whereas at other times it may not. Observations made during testing support this, whereby when actuation was initiated force readouts would show no change initially and then suddenly produce a step change as if the actuation had suddenly coupled with some feature of the flow, possibly the point of separation. The same unsteadiness is shown in Figure 4.21 for the 15m/s case.

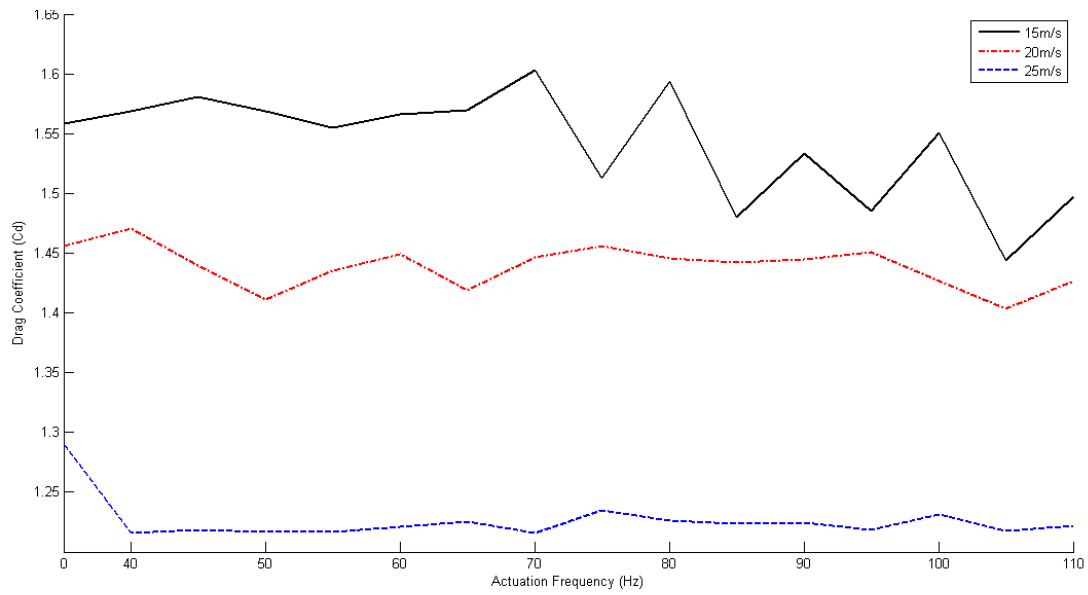


Figure 4.20 - Cd of tube with varying actuation frequency

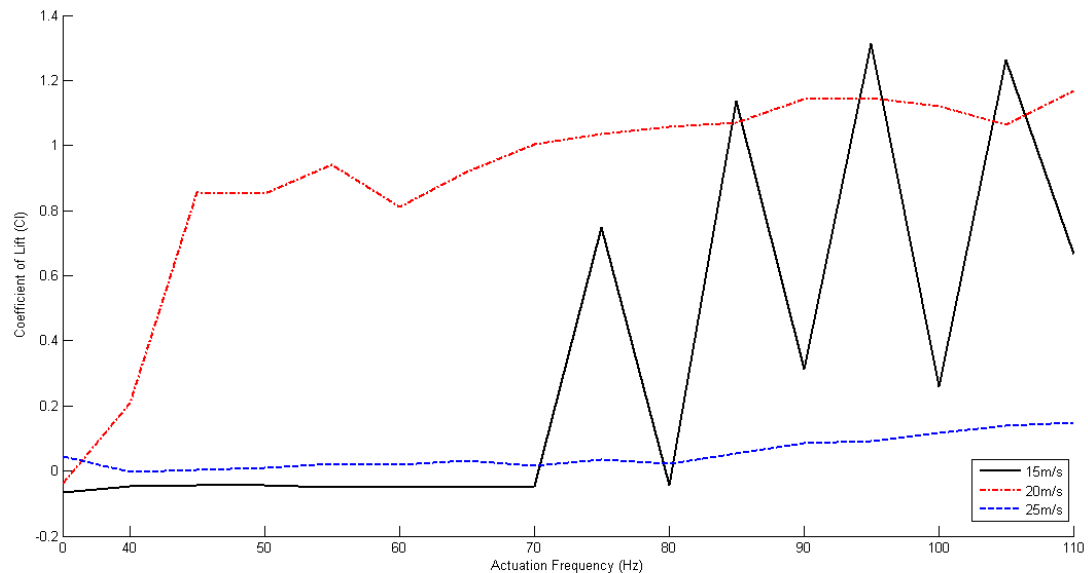


Figure 4.21 - Cl of tube with varying actuation frequency

Regardless of the behaviour seen at 15m/s, C_l increases with actuation frequency in each of the three cases shown in Figure 4.21. The 25m/s case only shows a slight increase in C_l , confirming the theory that the synthetic jet is having an effect but the jet momentum (C_{μ}) is too low, whereas the 20m/s case shows a significant increase in C_l . The increases in C_l at 20m/s match those found by Glezer, Amitay and Honahan (2005) (Figure 4.22), where by actuation frequencies of 110Hz shown in Figure 4.21 at 20m/s correspond to the Strouhal (St_{act}) number of 1 shown in Figure 4.22.

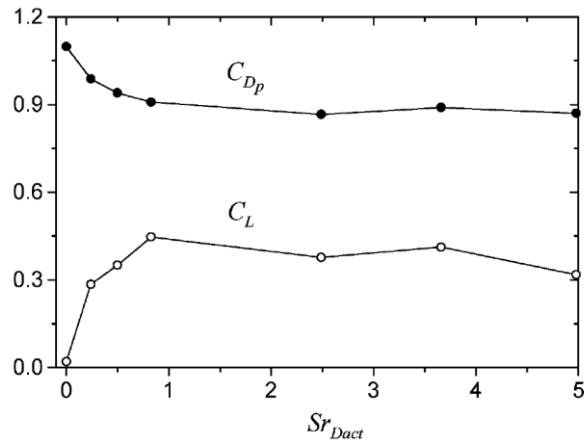


Figure 4.22 - Variation of the lift and the pressure drag coefficients with Sr_{Dact} (Glezer, Amitay and Honahan, 2005)

4.5 Discussion

From the testing carried out on a simple cylinder model it can be concluded that the synthetic jet actuation employed works to delay separation in laminar, transitional, and turbulent flow regimes. However the magnitude of C_μ is too low for use in flows with a higher freestream velocity.

In a presentation by Kourta (2008) magnetically actuated microvalves and plasma actuators were identified as systems offering jet outlet velocities of 80m/s and 500m/s respectively, where the current system is only anticipated to produce a maximum of 55m/s. However it is not known what scales these jets were produced at and it could be the case that although they can exhibit large peak velocities the scales are such that the penetration length of the Jet is small.

It may also be possible to tune the cavity to use resonance in order to achieve a higher C_μ however this is a difficult thing to achieve whilst maintaining a test setup that allows any sort of flexibility. If resonance is to be used as the main amplification factor for jet outlet velocity then only certain fixed actuation frequencies would be possible.

The behaviour seen in the transitional boundary layer cylinder flow is of interest because the separation point is unstable and transient. The fact that at times during testing the actuation frequency of the jet seemed to lock onto the separation point and create large changes in forces is encouraging for the future vehicle model testing. However it also causes concern that it did not reliably repeat this behaviour. The shedding process at the rear of the squareback model has already been described as a random Markovian process, where shedding behaviour is not consistent.

The difficulties in creating a large momentum coefficient and the concerns about the repeatability of success with synthetic jets, means that the probability of an experiment combining synthetic jets and a vehicle model being successful is significantly reduced.

The current testing has also highlighted the constraints associated with using acoustic drives to generate jets. If the jet is designed to run at resonance this restricts the operating frequencies to one or two choices, that may not be matched to the required frequency to control cross flow. The speakers that have been used also normally have a minimum drive frequency that they can be run at before the coil is damaged. This also restricts the lower frequency ranges available that may be of interest.

In the current testing the impulsively driven jets demonstrated that they can be operated with a great deal of flexibility and actuated at almost any frequency required. The use of a pressurised air source may not be desirable for the final application to road vehicles but in the context of experimental investigations seem to offer the most flexibility. In the first application of jets to control flow around the more complex Windsor model it was decided to simplify the actuators to allow greater control of the experiment. For this reason the first tests were conducted using steady blowing

Chapter 5

**ACTIVE CONTROL - CONSTANT BLOWING
EXPERIMENTS, RESULTS AND DISCUSSION**

5.0 Active Control Constant Blowing – Experiments, Results and Discussion

In the current chapter the standard Windsor model is modified to incorporate a system to apply constant blowing at the roof trailing edge of the model with the intention of modifying the overall size and shape of the wake. The system was developed such that multiple jet exit velocities could be investigated and various angles of jet outlet direction could be used. In addition to studying how body forces change with jet angles and exit velocities the vehicle ride height was also modified and measurements were taken at three ride height positions.

PIV investigations were used to study the effective configurations more closely to try to identify the mechanisms by which the body forces are being influenced.

5.1 Model

The Windsor model, used previously was modified to incorporate a NACA0021 wing profile, with 150mm chord, protruding from the centre of the model floor, to below the wind tunnel floor (Figure 5.1). This wing is fitted as shielding for pneumatic tubing and cabling that needs to be routed inside the model from underneath the working section.

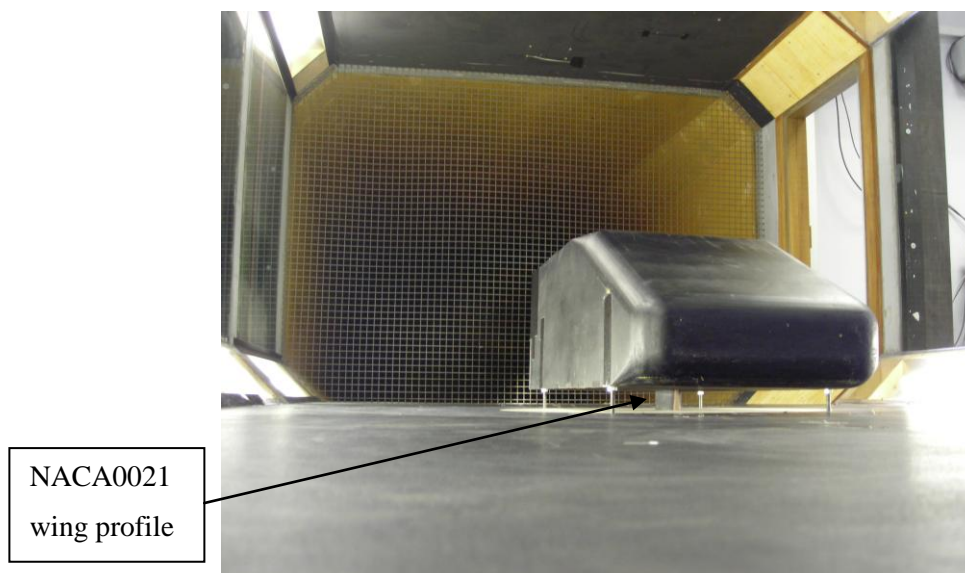


Figure 5.1 - Windsor model in working section showing NACA0021 wing profile

Four flexible tubes connect a machined cavity inside the model (Figure 5.3) to a pressure regulator and compressed air supply. Measurements of cavity pressure are taken via four pressure tappings in the cavity connected to a Furness Controls manometer with a minimum accuracy of ± 2.5 mmH₂O.

All cables and pneumatic tubes are hung vertically downwards from the model for a minimum length of 1 metre before being coupled to their corresponding connections to minimise effects on balance measurements of drag forces. A cradle was constructed around the tunnel balance to feed the pneumatics into the underside of the model without influencing the balance readings (Figure 5.2).

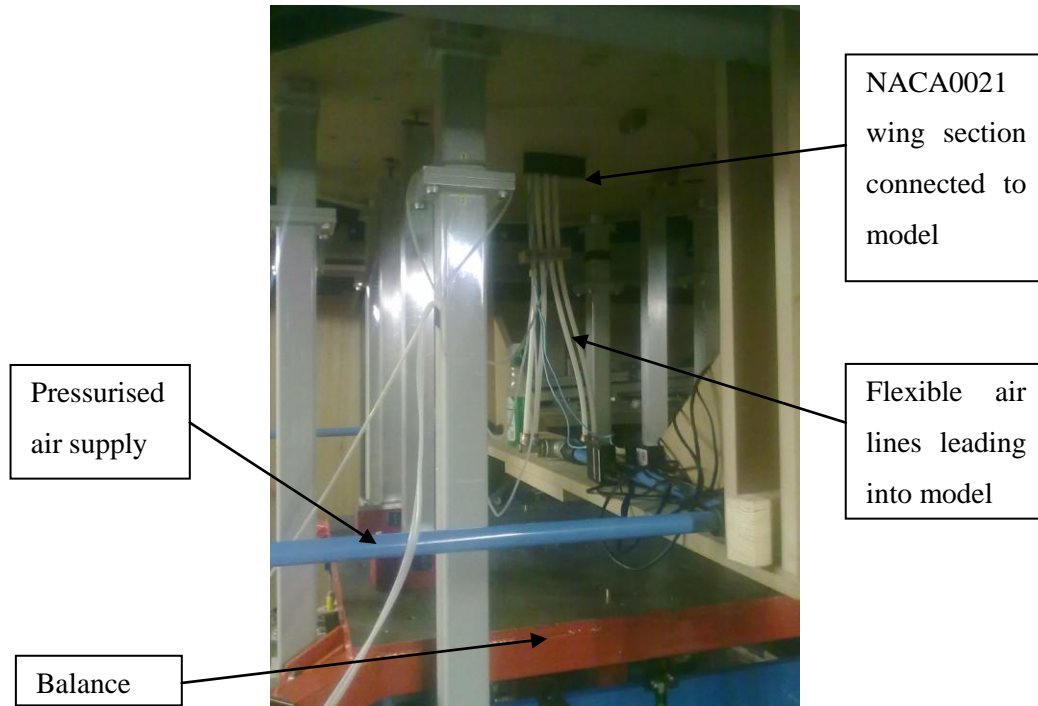


Figure 5.2 – Configuration under working section showing feed lines into model

The angle at which the jet exits the model is modified using removable ‘jet angle adaptors’ (Figure 5.3) manufactured from SLA resin, which also form the roof trailing edge of the model and incorporated routing for pressure tapings. The jet angle adaptors mount onto the cavity and contain internal ducting that directs the jet outlet in the different directions desired. The ducting is a consistent 1mm width and the shape of the cavity tapers down to create a smooth flow path into the duct. This small duct design is only practical to manufacture using rapid prototyping methods. The cavity is fed via 4 ports and contains a mesh to ensure a uniform pressure distribution along the width of the slot inlet.

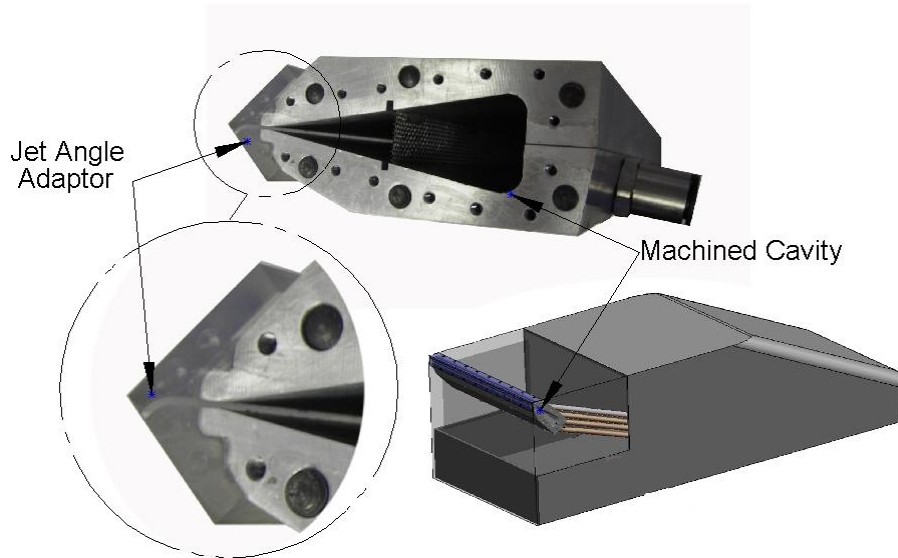


Figure 5.3 - Windsor model showing pressurised cavity and jet angle adaptor component

The jet angle adaptors maintain a sharp 90 degree roof trailing edge to ensure the model configuration stays as a squareback, whilst the jet exit angle is modified. The jet exit configurations tested were ‘vertically up’, ‘angled upwards and downstream (45°)’, ‘horizontally downstream’, and ‘angled downwards and downstream(45°)’ and will be referred to as configurations A, B, C, and D respectively (Figure 5.4).

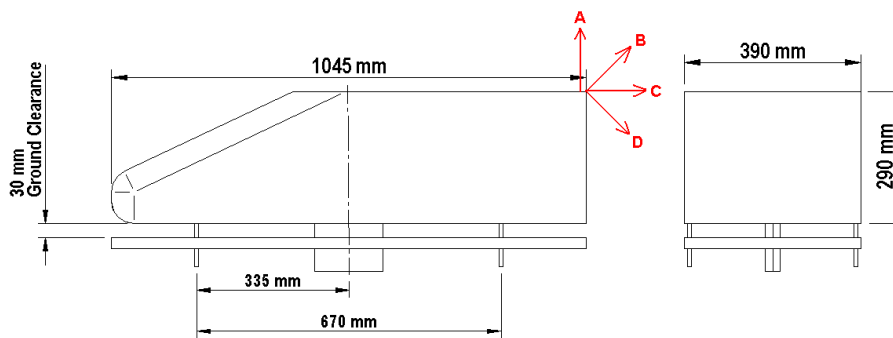


Figure 5.4 - Model dimensions and geometric jet exit configurations

The jet exit spans the full width of the model but is divided into nine equal sections by 0.5mm wide supports. The divisions are required to prevent the slot width increasing when air pressure is applied. The slot width is $1\text{mm} \pm 0.05\text{mm}$.

5.2 Slot Exit Velocity Measurements

In order to quantify the jet exit velocity a single wire hot-wire anemometer was positioned 1mm above the jet outlet, oriented in line with the jet exit axis. The hotwire was calibrated between 0m/s-

60m/s using a Dantec hotwire calibrator. At each location 5000 samples were acquired at a frequency of 1000Hz. The signal was hardware filtered using a low pass filter at 300Hz. The probe was traversed along the width of the model in 1mm steps to generate an average jet exit velocity. The average was used in the calculation of a jet momentum coefficient using Equation 5.1, where \dot{m} is the jet mass flow rate, V_j is the mean jet exit velocity, q is the freestream dynamic pressure and A is the model frontal area. This momentum coefficient non-dimensionalises the momentum of the air blown from the jet against the air in the freestream. This equation is similar to Equation 4.3 but here a reference area is used rather than a reference length scale, to incorporate the exit area of the jet outlet relative to the model dimensions.

Equation 5.1
$$C_\mu = \frac{\dot{m}V_j}{qA}$$

The presence of a V^2 term in the numerator for the jet and the denominator for the freestream flow means that manipulation of the relationship between the jet exit velocity and the freestream velocity creates more significant changes in C_μ than a manipulation of the physical size of the model to slot width ratio. Previous authors (Lin 1999) have placed an emphasis on the requirement for high C_μ . In the current work higher C_μ values could be achieved using lower freestream velocities, however freestream velocities were only reduced within a region where results were found to be insensitive to Reynolds number.

The presence of a V^2 term also creates additional factors to consider when deciding how best to scale the technology to full scale. An optimum choice of jet outlet width and jet outlet velocity for the minimum mass flow rate requirement and power input would give the optimum choice of C_μ .

5.2.1 Jet Characterisation

Figure 5.5 shows an example jet exit velocity profile across one half of the model width, and illustrates the need to use an averaged jet exit velocity. The width of the slot incorporates physical divisions for strength, and local minima can be seen where the structural divisions were located to strengthen the slot. The velocity measurements at these locations were removed from the calculation of the mean exit velocity, which was only calculated over the open slot area. These data points were removed because the calculation of C_μ should only be based on flow exiting the slot outlet and not any velocity created by entrainment of the surrounding medium.

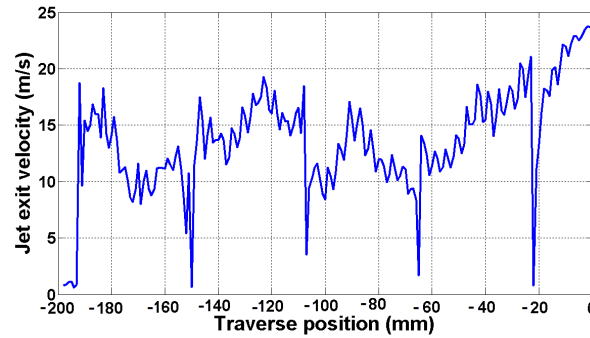


Figure 5.5 - Example hot wire measurement of jet exit velocity profile

The orientation of jet nozzle exit on the jet angle adaptors A, B, C and D were manufactured to be A;vertically up B; at 45 degrees between vertically up and horizontally downstream C; horizontally downstream and C; at 45 degrees between vertically downwards and horizontally downstream. In quiescent conditions the measured axis of the jet exit for configuration A, B and C were well aligned with the geometric jet exit axis. However in configuration D it was noted that the jet was vectored downwards towards the base wall of the model, This results in a measured jet axis angle of approximately 9.5 degrees. This is shown in Figure 5.6 where the jet exit position is at $x=0$ $y=0$, the black line shows the actual jet axis centre, and the red line shows the geometric axis at 45 degrees.

The change in jet exit angle relative to the geometric outlet angle is introduced in configuration D because of the need to use internal curved ducts to direct the jet out of the model at a downwards angle. The curved ducts introduce some circulation at the outlet of the jet meaning the air is vectored further downwards. Additionally the jet is angled downwards along the base surface and it is common that this type of jet will try to re-attach to the surface, which is seen as a deflection of the flow. This does not present a problem for the testing but is worthy of note for the design of future ‘jet angle adaptors’ that this topology exists and may need to be repeated if successful control is achieved.

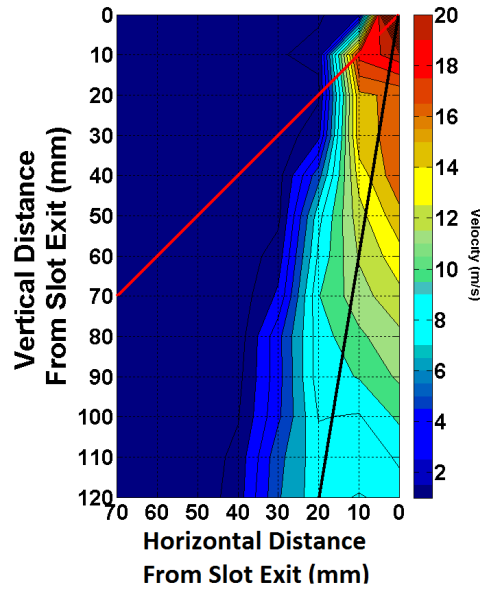


Figure 5.6 - Jet exit velocity contour plot at different spatial locations

5.3 Force Measurements

There was some concern that the pneumatic tubing required to be fed into the model could cause balance measurements to be compromised and create poor repeatability. Using an example set of data acquired at 40 m/s freestream velocity Figure 5.7 shows that measured drag coefficients recorded in a 30 second sample are still accurate to less than $\pm 0.001 C_d$ (1 count) with 99% confidence.

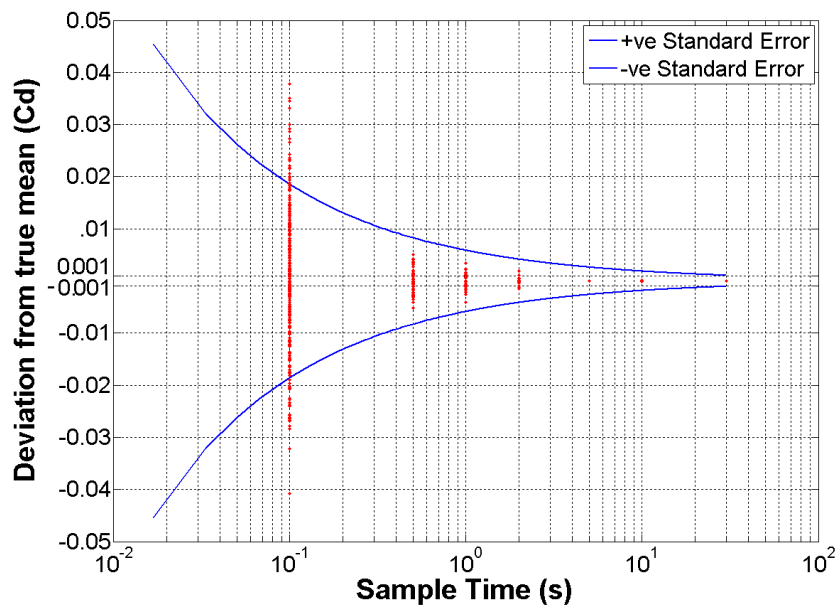


Figure 5.7 - Accuracy of Cd measurements

Measurements of baseline drag coefficient were repeated 18 times over a period of 3 days. During the 18 baseline tests the model was removed and re-installed on the balance twice, and measurements were taken with and without all tubing and cables connected. Within these repeats the fluctuation in measured drag coefficient for the model never exceeded 2 counts, indicating that the installation of the tubing had little influence on the measured balance data.

The thrust force produced by each jet configuration was measured in quiescent conditions using the wind tunnel balance. The baseline thrust forces were subtracted from measured drag forces on the model when in freestream flow with the jets active.

Measured C_d values were corrected for blockage using the MIRA area ratio method shown in Equation 2.4

5.4 Pressure Measurements

The base of the model was fitted with 111 surface pressure tappings which were connected via flexible tubing to two 64 channel pressure scanners mounted inside the model. Data was acquired from the scanners via CAN technology which required two ethernet cables to be routed through the wind tunnel floor and through the model floor at its centre-line. All pressure measurements used to calculate coefficients of pressure were corrected for blockage using Equation 2.6.

5.5 PIV

A LaVision dual camera 2D PIV system using a dual pulsed Nd:YAG laser to produce a light sheet in the stream-wise plane along the centre line of the model was set up as shown in Figure 5.8. For the current tests higher resolution cameras were available with 2048 x 2048 pixels giving a high vector grid resolution as described in section 2.5.5 and image pairs were acquired at 5Hz and a sample of 1000 image pairs was taken for each configuration tested. A sliding average of the minimum background light intensity in three consecutive image pairs was calculated for each set of 1000 images. This sequence of background light intensity was then subtracted from each image pair in sequence in order to reduce the effects of background light on the correlation process. A multi-pass decreasing window size correlation processing algorithm was used with a final window size of 32x32 pixels, with a 50% overlap.

The location of the seeding rake and the acquisition parameters were tuned until a minimum of 95% first choice vectors were present in the instantaneous images. Seeding was generated by a laskin nozzle oil seeder located approximately 1.5L upstream of the model front. This is the same position

as the previous tests where the seeding rake was shown not to influence the trends in the results (Figure 3.11).

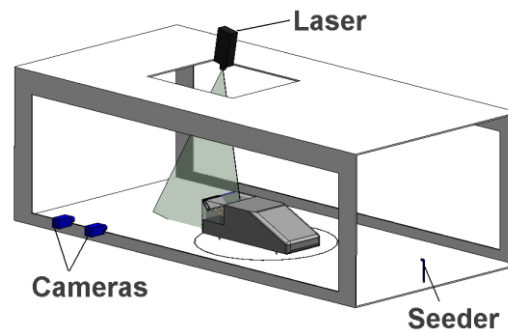


Figure 5.8 - PIV experimental setup

5.6 Results – Balance Measurements

Of the four configurations tested only configuration D produced a reduction in drag coefficient, whilst configuration A, B and C produced a gradual increase in drag coefficient with increasing jet momentum coefficient. Configurations B and D are selected for further discussion to try to investigate how they influence the body drag force.

Figure 5.9 shows the changes in drag coefficient for configuration B vs. increasing jet momentum coefficient. At all the ride heights tested the drag gradually increased with increasing momentum coefficient and the results showed the same trends at different model length based Reynolds numbers. In configuration B, with the jet acting at 45 degrees upwards, at the point of separation it is suggested that the size of the wake is increased by deflecting the shear layer upwards. Some theories regarding the influence of wake size on resultant body forces predict that a stretched wake will create increased base pressures by moving vortex structures away from the base surface and so reduced body drag forces (Pastoor 2008; Bearman 1983). Other published work (Rounmeas 2008) suggests that a reduction in wake size will increase base pressures and create lower drag forces. Fig. 7 supports the theory that a larger wake will create larger drag forces.

It is known from section 3.3 that the time averaged vortex structure seen at the top half of the wake flow is much weaker than the lower vortex structure. In fact it could be argued that this structure does not really exist as a steady phenomenon. If so it makes sense that applying blowing which deflects the shear layer upwards at the upper separating edge would increase drag.

In this case the blowing increases the overall size of the wake, leading to lower pressures on the base. Any gains (increases in base pressure) that may have arisen from moving vortices away from the base

surface (Bearman P.W., 1983) (Pastoor et al., 2008) cannot be achieved here, because there is no strong steady vortex structure present in the baseline configuration in the upper wake.

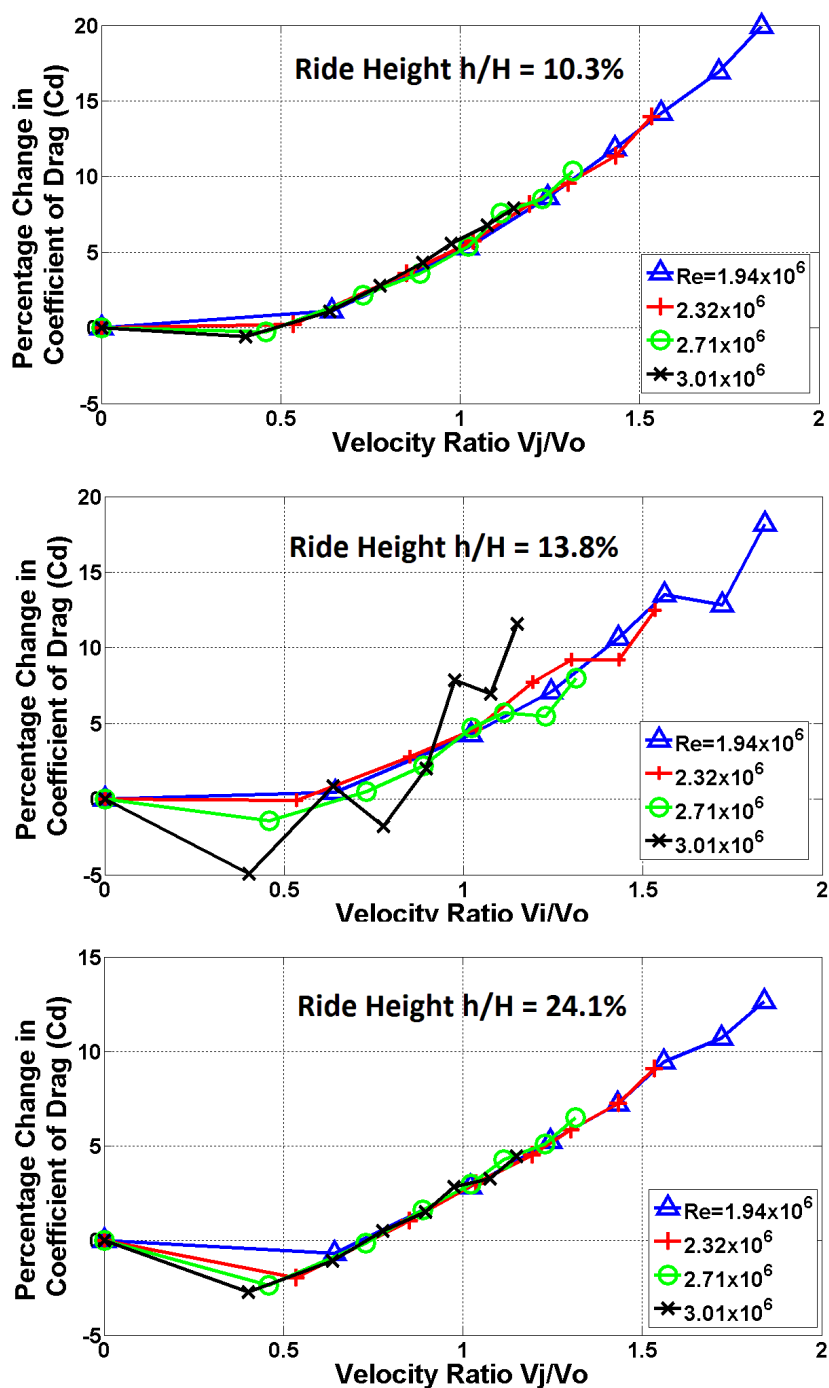


Figure 5.9 - Changes in balance measured C_d for configuration B at ride heights of 10.3%, 13.8% and 24.1%

The absolute change in C_d for a given momentum coefficient is increased as the ride height is decreased. If the drag force changes are linked to wake size and it is the dominant factor involved, it

would suggest that at lower ride heights the wake size is increased more for a given momentum coefficient. However the change in drag reduction as ride height is reduced from the extreme case of $h/H= 24.1\%$ to $h/H= 10.3\%$ is an average of 1.7 times greater. If the change in wake size was anything close to proportional to the changes in drag forces then the wake size increase required to create the measured force changes would also be significant. For this reason it is believed that additional factors within the wake have an influence on base pressures and hence body drag forces. This would suggest that as ride height is decreased the influence of blowing on the ‘in-wake’ vortex structures becomes more significant.

Figure 5.10 shows the changes in drag coefficient as a result of blowing using configuration D, at a ride height of $h/H = 10.3\%$. Significant reductions in C_d are observed which gradually increase as momentum coefficient is increased. As seen in other configurations the trends are not sensitive to Reynolds number, which allows larger C_μ values to be tested by reducing the freestream velocity.

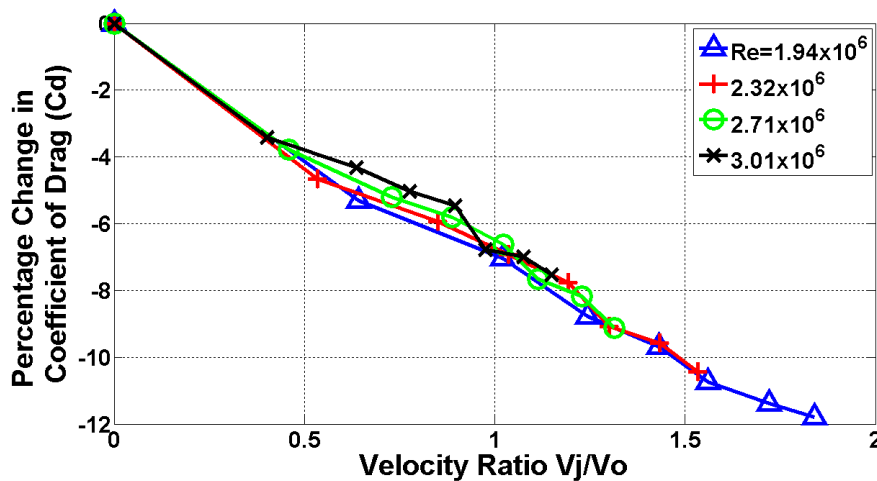


Figure 5.10 - Changes in balance measured C_d for the Configuration D at a ride height of 10.3%

As per Figure 5.9 it would be reasonable to attribute the drag reductions seen in Figure 5.10 to a deflection of the shear layer downwards creating a reduction in the overall wake size. However the drag reductions are sufficiently large (3%-12%) that if wake size alone is the dominant influence on base pressure and body forces the wake size reduction would be significant. The magnitudes of drag changes observed support the theory that additional ‘in wake’ factors may have an influence on drag forces in addition to the modification of wake size alone. In order to investigate the changes further, base surface pressures and in wake PIV measurement techniques were used.

With Figure 5.9 and Figure 5.10 exhibiting a lack of Reynolds number sensitivity the following sections will focus on a test Reynolds number of 3.01×10^6 which has been chosen for further analysis.

This Reynolds number has been selected as it creates the least favourable C_{μ} values tested but also the most representative values if the technology were to be scaled up to production vehicle magnitudes.

5.7 Results - Pressure Measurements

In the baseline configuration the base surface pressures exhibit a similar pattern observed for this configuration, as seen in Figure 3.9, but with slightly more 3D effects being introduced at the lower corners. The main feature observed in the base pressure contours is still a large region of suction on the lower half of the base surface between $h/H=0$ and $h/H=0.4$. On the upper half of the base the pressures gradually increase towards the roof trailing edge, and are more uniform across the base width, indicating the two dimensional nature of the flow in this region. The slight modification to the base pressures at the lower corners can be attributed to the introduction of the NACA0021 wing profile in the under floor region, which will certainly be having an effect on the underbody flow which feeds into the large lower vortex structure. Immediately below the roof trailing edge a reduction in pressure is observed where separation occurs.

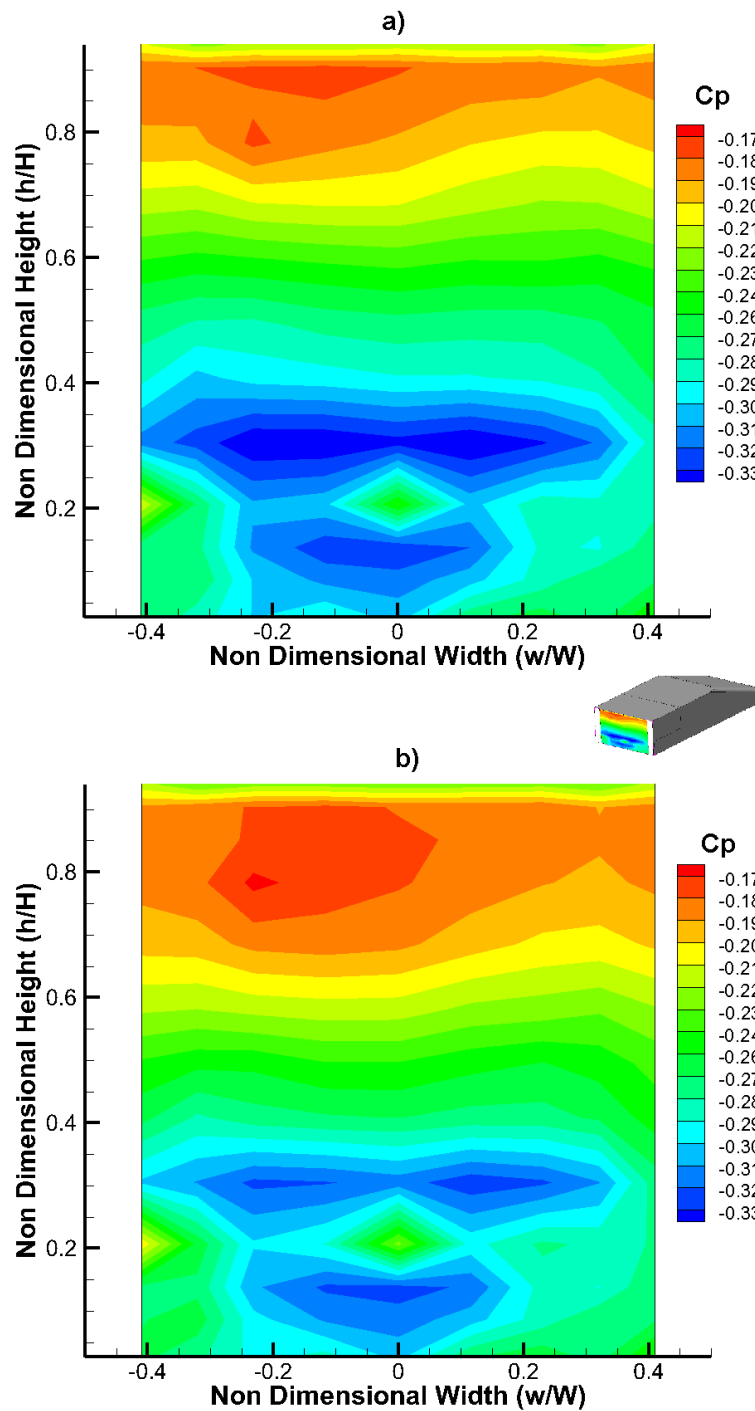


Figure 5.11 - Base pressure contours for: a)baseline and b) blowing configuration D at $C_\mu = 0.013$ and $Re = 3.01 \times 10^6$

When blowing is applied in Configuration D at a momentum coefficient of 0.013 a global increase in base pressures is observed (Figure 5.11b). The pressure contour patterns observed in Figure 5.11a remain present in Figure 5.11b however the low pressures observed in the lower half of the base for the baseline configuration have increased with the application of blowing. This increase has resulted in a more uniform distribution of base pressures and a less pronounced suction region between $h/H=0$

and $h/H=0.4$. From this data alone in the base pressure results it could be argued that the application of downward blowing at the roof trailing edge is reducing the strength of the lower vortex, giving rise to the increased base pressures in the lower base half.

The pressure data is checked against the balance data by calculating the area weighted C_d changes using Equation 3.2. The calculated area weighted coefficients are plotted alongside the balance measured coefficients in Figure 5.12.

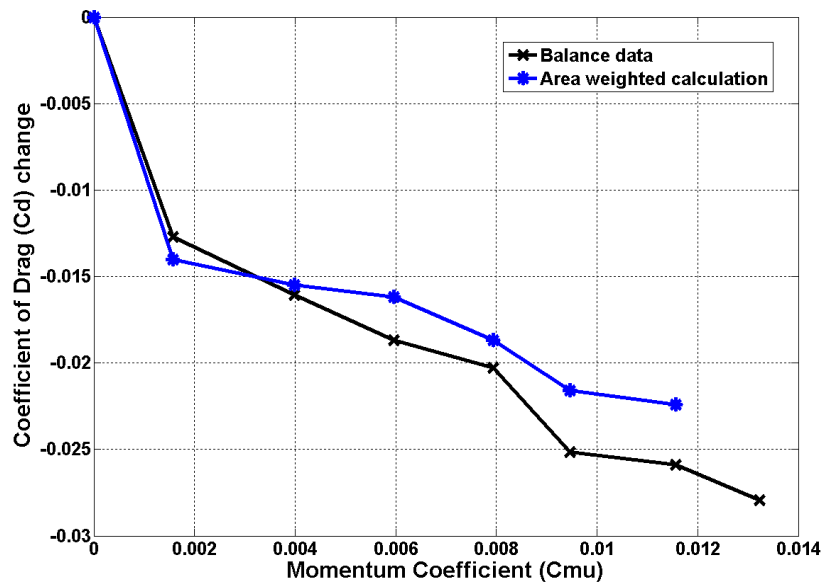


Figure 5.12 - Balance and area weighted calculations of changes of C_d Configuration D at $Re = 3.01 \times 10^6$

Figure 5.12 also illustrates that the changes in total model drag measured by the balance are primarily as a result of changing pressures on the base surface, as opposed to changes in pressures on forward facing surfaces at the front of the model. As momentum coefficient increases the pressure data trends show a good match with the balance data and highlight the significant initial reduction of 13-14 counts when $C_{\mu}=0.0016$.

5.8 Results - PIV

Figure 5.13 shows time averaged PIV streamline plots of the baseline un-blown case at a Reynolds number of 3.01×10^6 , acquired from the measurement plane shown in Figure 5.8. The rear portion of the model is shown as a solid dark region. The size of the wake produced by the model is significant and using an additional camera in the current PIV measurement helps to illustrate the scale of the far field wake. However, even with the additional camera the complete wake is still not captured in the FoV. Within the near wake between $L/l=0$ and $L/l=-0.25$ strong structures are again seen in close

proximity to the base. The dominant structure is the lower re-circulating vortex that interacts with the model base surface causing low base pressures as shown in Figure 5.11a and documented in section 3.0. Interestingly the lower re-circulating vortex appears to be shorter and taller than in the baseline case for section 3.3. This is attributed to the addition of the NACA0021 wing profile under the floor which will modify the underfloor flow, which is the main source of energy in creating this structure.

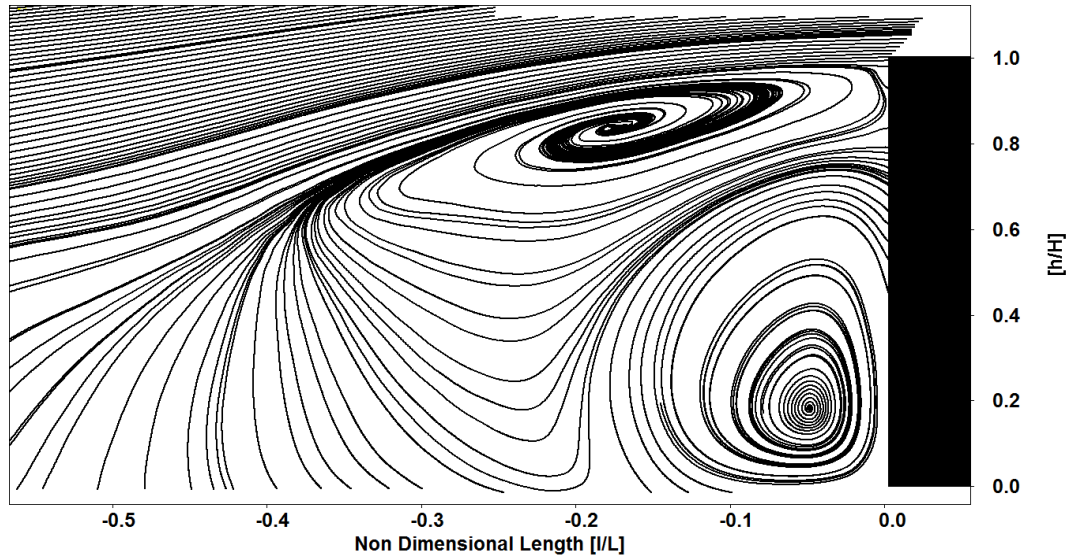


Figure 5.13 - Streamline plot in the wake of un-actuated baseline configuration at 10.3% ride height

Figure 5.14 shows the baseline wake structure for an increased ride height of 13.8% which shows the lower vortex structure more closely resembling the size and shape seen in section 3.3. The higher ride height also modifies the flow of air under the model which shows that the size, shape and strength of the lower vortex structure is obviously closely linked to underbody flow conditions.

The total size of the wakes produced at 10.3% and 13.8% ride heights are actually very similar, but the in wake structures are modified significantly. This difference in the baseline wake structures may explain why the application of blowing at a given momentum coefficient has a different magnitude of effect on C_d at different ride heights.

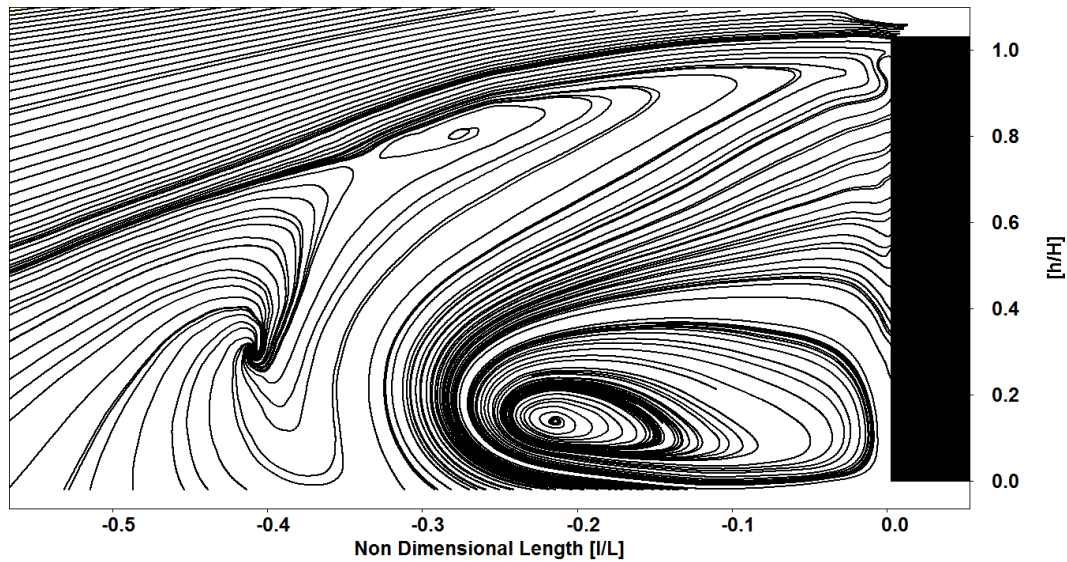


Figure 5.14 - Streamline plot in the wake of un-actuated baseline configuration at 13.8% ride height

Figure 5.15 shows the effect of steady blowing in configuration B, where streamlines that start at the rear separating edge as seen to rise upwards and out of the FoV, indicating that the separated flow is being deflected upwards, enlarging the wake. The deflected flow is shown in the deflection of a streamline at a location of $l/L \approx 0.45$ $h/H \approx 1.1$. The lower vortex structure has also grown in size and now interacts with almost the entire rear base surface up to $h/H=0.95$. This would allow low base pressures to arise from both the global growth of the wake but also the ability for the vortex to interact with more base area.

In addition to this the far wake has become much more three dimensional, with what appears to be a source flow at $l/L=0.45$, $h/H=0.55$. This 3D effect cannot properly be quantified in the current measurements because only 2D velocity information is available. Further investigation using a Stereo PIV setup would be of value in this configuration.

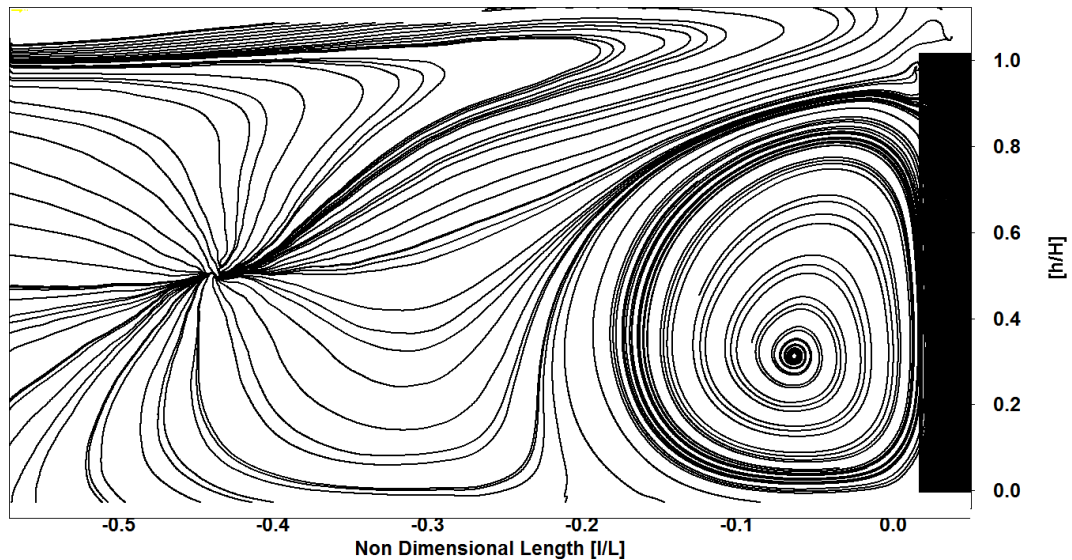


Figure 5.15 - Streamline plot in the wake of blown case at $C_{\mu}=0.012$ $h/H=10.34\%$; configuration B.

Figure 5.16 shows the same configuration as Figure 5.13 but shows the vorticity in the wake as a contour plot. Figure 5.17 shows the same measurement plane when blowing is applied in the ‘downward blowing configuration’ (D) at $C_{\mu} = 0.012$. An overall wake size reduction is observed but it is not as significant as expected from the drag reductions observed in Figure 5.10. To illustrate the change in wake size a single streamline was plotted at the point of separation at the rear trailing edge of the model in the blown and unblown case. This streamline is then used to indicate the outer edge of the model wake in both cases. Both streamlines are plotted in Figure 5.17 where the upper streamline shows the boundary of the wake in the unblown configuration, and the lower streamline shows boundary of the wake in the blown configuration. If these streamline boundary positions are used to calculate a 2D wake area change between the two configurations then the application of steady blowing creates a 14.2% wake size reduction for a 7.5% reduction in drag (Figure 5.10). When this method is applied to previous work in section 3.3 using passive optimisation, the small chamfer that led to a 4.4% drag reduction is associated with a 11.1% wake size reduction.

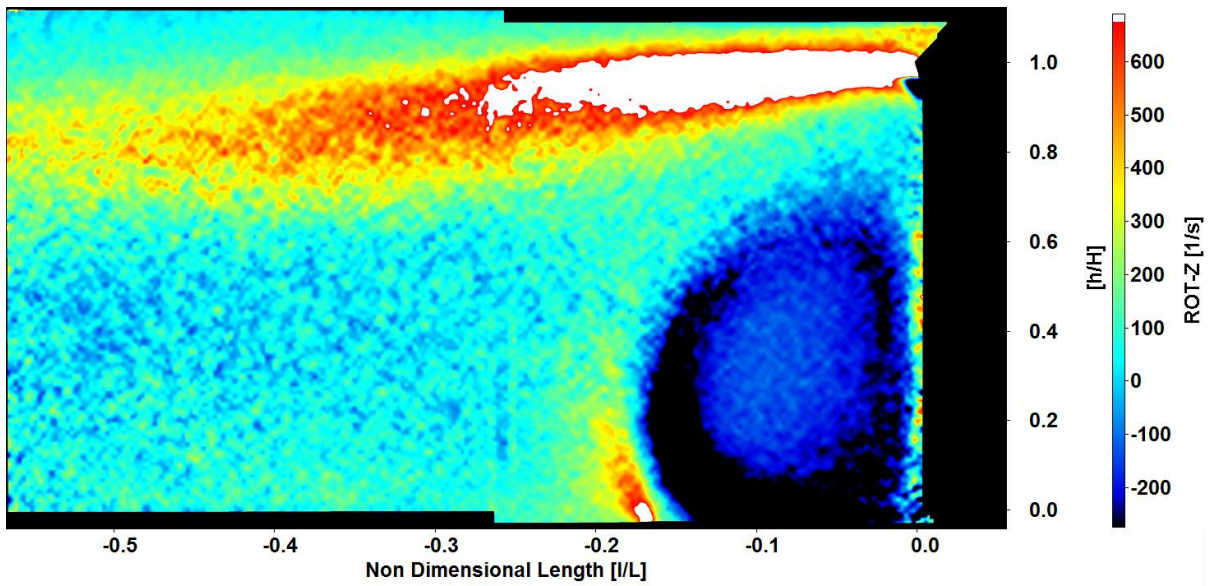


Figure 5.16 - Time averaged PIV image for unblown baseline configuration $h/H=10.3\%$, $Re = 3.01 \times 10^6$ showing vorticity

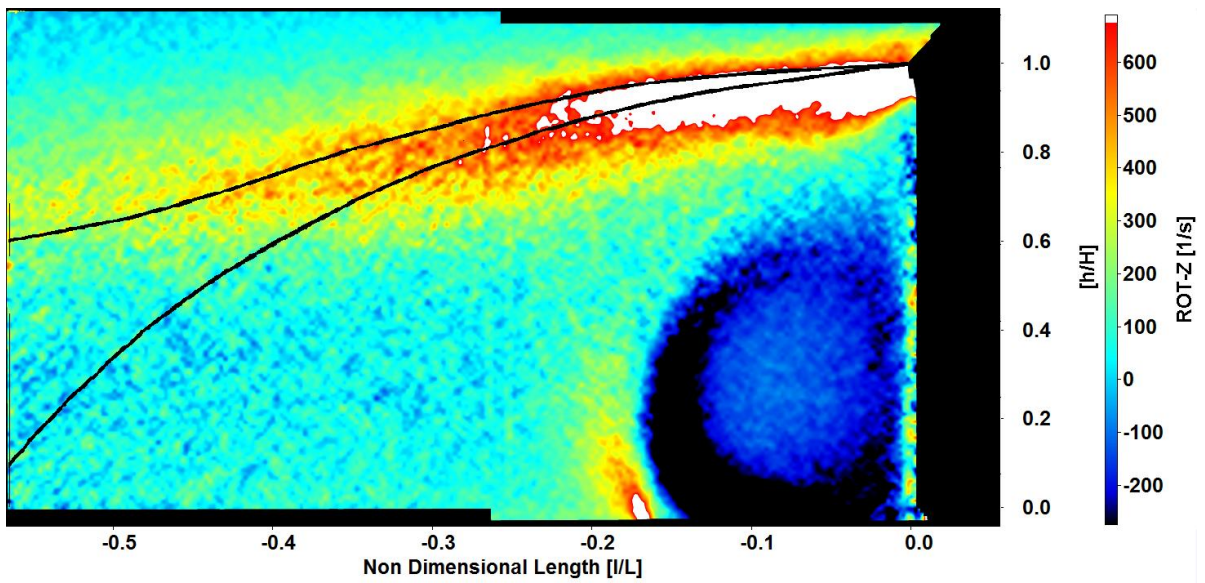


Figure 5.17 - Time averaged PIV image for downward blowing configuration D, $C_{\mu}=0.012$, $h/H=10.3\%$, $Re = 3.01 \times 10^6$ showing vorticity

It is recognised that some 3D trailing vortices may be appearing at the upper corners of the roof trailing edge in both the passive optimisation case and the actively blown case discussed here. Any large scale 3D structures would mean that using the centreline PIV plane as an indication of wake size would become invalid. However in Figure 3.9 and Figure 3.10 base pressure contributions and slant angle contributions were analysed to conclude that the flow structure remains largely 2D across the span of the model base, with the application of small chamfer angles. Additionally, the majority of changes in body drag forces are as a result of base pressure recovery. In the current work, no slant angle is present and the application of downward blowing shows no onset of 3d vortices at the upper corners. This can be concluded by comparing the base pressure contour plots with and without blowing (Figure 5.11), and also comparing these against the contour plots in Figure 3.9 where 3d C-pillar vortices did begin to occur at the larger chamfer angles studied.

As the lower vortex structure is linked to a large region of suction, it is concluded that the significant reductions in drag observed in Figure 5.10 are mainly as a result of modification to this lower structure, and its interaction with the base surface in addition to the global reduction in wake size. In effect, the benefits of stretching the wake to move vortices further away from the base outlined by Bearman P.W. (1983) and Pastoor et al. (2008), are, in this instance, created by the downward blowing of the jet weakening the lower vortex structure. The weakening of this structure is shown in the reduction in the magnitude of vorticity of the structure. This effect can be seen by comparing the vorticity seen in Figure 5.16 with Figure 5.17. The discovery of this approach represent a significant breakthrough and the principles can be used to try to successfully implement forms of flow control and modification in future.

In the baseline case there is a large band of strong, negative, vorticity on the right hand side of the lower vortex close to the base surface (shown as black contour regions). In the baseline case this band of the contour plot covers a region between $l/L = 0.1$ to $l/L = 0.4$ and $h/H = 0$ to $h/H = 0.6$. When blowing is applied, this area of the wake close to the base surface that is in this vorticity band is reduced significantly and only small patches of black remain. This reduction in vorticity inevitable leads to a reduction in the local velocity interacting with the model base surface. In addition to the reduction of vorticity in the lower vortex the levels of vorticity in the shear layer are also reduced

It is well known that an increase in surface velocity over a flat plate will create a reduction in static surface pressure, and this theory has been used in assessing some of the effect on the lower vortex structure on the model base surface. Figure 5.18 shows the in-plane vertical velocity magnitudes, with and without blowing. The region covered in Figure 5.18 is a close up of the wake flow region close to the base surface taken in the PIV tests described above. In the region where the lower vortex structure interacts with the model base surface, velocity magnitudes are reduced by approximately 2 - 4m/s for

the blown case, relative to the un-blown case. In the current application the downward blowing jet reduces the rotational energy of the lower vortex structure leading to a reduction in the velocities measured at the model base surface, which then increases the surface pressures. This finding is interesting and could be used in future to target and disrupt vortices or high velocity flows close to rearward facing surfaces.

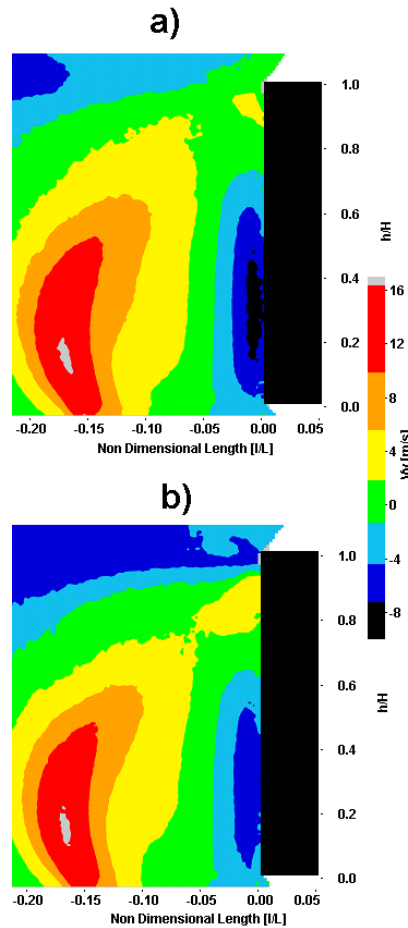


Figure 5.18 - Vertical velocity components for baseline (a) and blown case (b)

5.9 Net Drag Changes

A configuration has been found where active blowing creates a significant drag reduction, however the momentum coefficients required to produce the change are high and an overall gain can only be claimed once the jet power requirement is subtracted from the aerodynamic drag power saving. The net aerodynamic power saving is calculated using Equation 5.2 and the net power saving for Configuration D, at various momentum coefficients, and a test Reynolds number of 3.01×10^6 are shown in Figure 5.19.

Equation 5.2

$$AP_{NET} = (\Delta F_{DRAG} \times V) - (\dot{m}_j \times V_j^2 \times \eta_j)$$

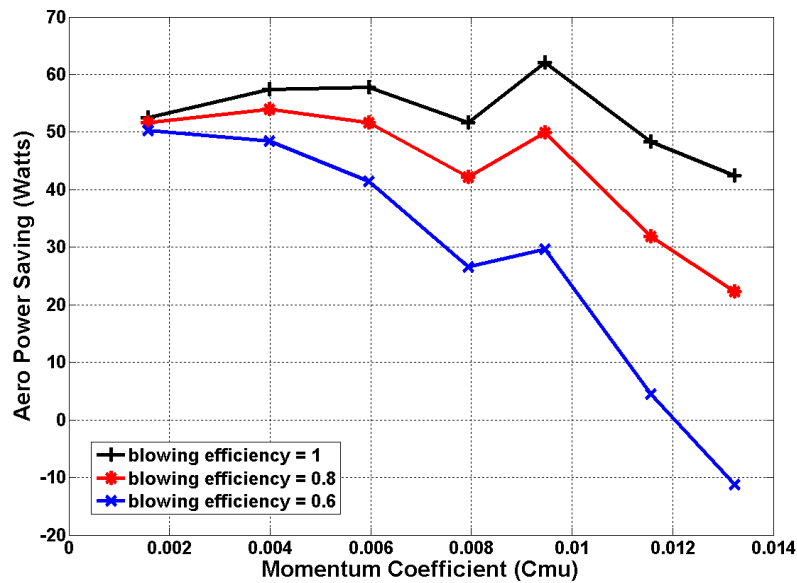


Figure 5.19 - Aerodynamic Power savings available at different blowing system efficiencies

If assumptions are made that the blowing system used is 100% efficient then net aerodynamic power savings are observed (Figure 5.19). The savings available for the wind tunnel model tested are relatively constant up to $C_{\mu} = 0.0095$, and range from 52.5W to 62.5W in this region. Above $C_{\mu} = 0.0095$ the aerodynamic power savings available are reduced.

If it is possible to maintain the same balance of input power to the system vs savings in aerodynamic drag power for a full scale vehicle rather than a $\frac{1}{4}$ scale model, the power savings could be up to 16 times greater (840W to 1kW). However, it is unknown whether the same net drag power savings would be achievable because of the complexity of the scaling problem, which not only involves the scaling of the physical size of the vehicle, but also the jet dimensions, and its effect on jet performance and power consumption.

Additionally any practical system that is used to create the blowing will have losses due to efficiency, whether from compressor efficiency or losses in pipework required to implement the system. The effect of this efficiency term is also included in Figure 5.19, and shows a significant reduction in net power saving as C_{μ} increases and η_j decreases. This illustrates that although the largest C_d reductions are achieved with the highest C_{μ} available, the potential for net power savings is highest when lower C_{μ} values are used. This is substantiated further when vehicle mass increases and packaging spaces are considered; even the lower C_{μ} values tested require the use of heavy and physically large

compressors and storage tanks. Vehicle mass increases will create an increase in the tractive effort required to move the vehicle, and as such the smaller and lighter the blowing system can be used.

Currently even with the potential net aerodynamic power savings demonstrated at low C_{μ} values a direct application of the technology using compressors and storage tanks is unlikely to be practical due to the high mass flow rate requirements and consequently the need for large and heavy equipment. However it may be possible that similar effects may be achievable using systems such as NACA ducts to passively duct freestream flow into the wake whilst maintaining the lines and appearance of a standard vehicle, and this is a suggested investigation for further work outside of the current thesis. It may also be possible to reduce the duty cycle of the jet using pulsed blowing, such that the wake flow is still modified, but the total mass flow rate requirement is reduced. Alternatively a pulsed jet may induce some of the effects that have been described when using Synthetic Jets and also help to recover pressure in the wake by using specific excitation frequencies.

Application of SJ actuators to the Windsor model has been avoided because of the lack of available momentum coefficient and the number of performance variables that raised doubts about their successful application. However, a pressurised cavity with controllable valves that can create a consistent mass outlet flux whilst also being able to control actuation frequency may lead to further understanding of how pulsed jet excitations may affect base pressures.

5.10 Discussion

The influence of steady blowing applied at a variety of angles on the roof trailing edge of a simplified $\frac{1}{4}$ scale square-back style vehicle has been investigated. Increases in measured drag coefficient were observed for all configurations tested except for the '45 degrees down' configuration, where large improvements in drag are possible.

The changes in drag coefficient were corrected for blockage effects and the influence of jet thrust has been subtracted. Where significant drag reductions were observed an effort has been made to understand the mechanisms which cause this change. For these configurations the majority of changes in drag forces are as a result of base pressure modification which has been supported using an area weighted base pressure coefficient calculation.

In the cases tested at $Re = 3.01 \times 10^6$ the reduction in drag observed when blowing was applied at a 45° downwards angle has been attributed to a reduction in wake size via a deflection of the upper shear layer downwards and reduction in the levels of vorticity found in the wake. This reduction in

vorticity in the lower vortex structure leads to a reduction in the local surface velocities on the model base. The vorticity of the lower wake structure is reduced by the jet flow opposing the direction of rotation of the large lower vortex.

Although the highest reductions in C_d are achieved at the highest C_μ configurations tested, an analysis of the net change in aerodynamic power has revealed that a system would be most efficient using low C_μ configurations.

Although the current work shows promise for the use of active blowing the current mass flow rates required would be prohibitive when trying to directly implement the techniques to a production road vehicle. The use of passive ducting of freestream flow may allow the technique to be exploited whilst still maintaining global vehicle shapes and packaging requirements. The next stage of investigations should look for lower energy demand means of creating the saving found in this chapter.

Chapter 6

**ACTIVE CONTROL - PULSED BLOWING
EXPERIMENTS, RESULTS AND DISCUSSION**

6.0 Active Control Pulsed Blowing – Experiments, Results and Discussion

6.1 Introduction

In Chapter 4.0 a number of zero net mass flux devices have been tested on a simple cylinder model with some success. However there was a general lack of momentum coefficient available from the actuators to be consistently effective at high Reynolds numbers. In Chapter 5 significant reductions in C_d were achieved using steady blowing but this required a relatively large mass flux. The tests conducted in the current chapter are to investigate if a reduction in the duty cycle of the blowing can still achieve a significant reduction in C_d . It is also hoped that some of the flow control effects exhibited by SJ actuators may be created using pulsed blowing, which can also be easily controlled and quantified.

6.2 Model

The design of the ‘jet angle adapters’ and pressurised cavity described in the previous Chapter was changed, whilst still maintaining a similar principle of operation. The pressurised cavity was made as large as physically possible to fit inside the model. This was done to avoid the pressurised air in the cavity being completely exhausted during the outlet stage of the pulsed blowing, which would have led to a gradual reduction in jet outlet velocity over the outlet stroke.

The valves selected to switch the jet outlet from closed to open were Festo MHJ fast switching valves, capable of switching at up to 1.5KHz. The MHJ valves are only available with a small 4mm pipe push fit outlet, limiting the outlet cross sectional area, which is very small. If a single valve was used then area change from a single valve outlet to the outlet area of a 1mm slot spanning the width of the Windsor model would have led to significant losses. To mitigate against the effects of losses due to area changes the slot was divided into 9 equal width sections, with each section fed by a pair of MHJ valves. This required 18 valves connected via a custom PCB to a Labview digital out card that was capable of triggering the valves simultaneously (Figure 6.1). This is the experimental solution but for a production vehicle approach a purpose designed system would be required.

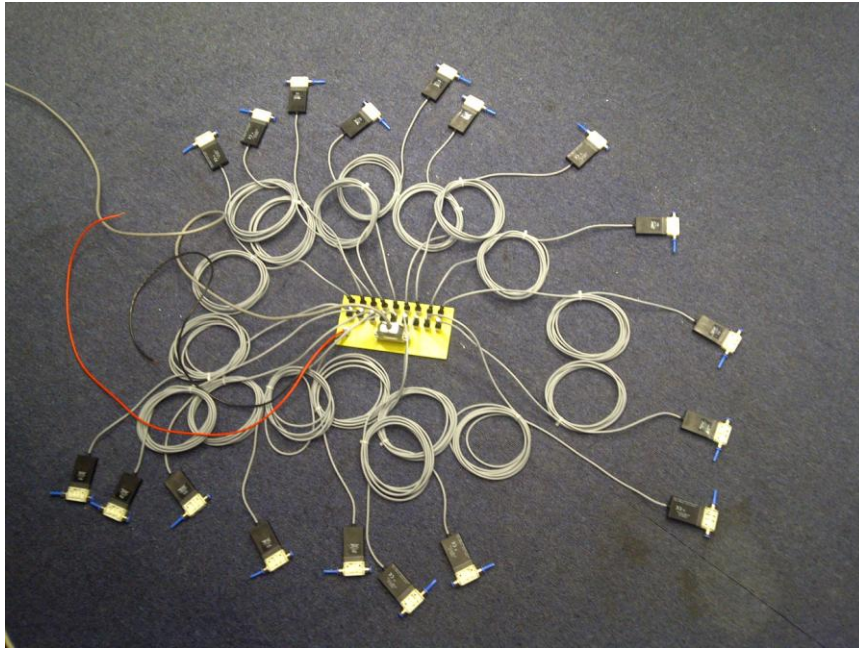


Figure 6.1 - Festo MHJ fast acting valves connected to custom PCB

New 'jet angle adaptors' were manufactured from 3 sections of rapid prototype components and one aluminium manifold which were bonded together. The rear of the Windsor model was also modified to dovetail with the new jet angle adaptors at the rear roof trailing edge or the lower floor trailing edge (Figure 3.1). This was done to create the possibility of actuating the jet at the floor trailing edge to try to disrupt or enhance the lower recirculating vortex which has so far proved to be the dominant feature in the flow.

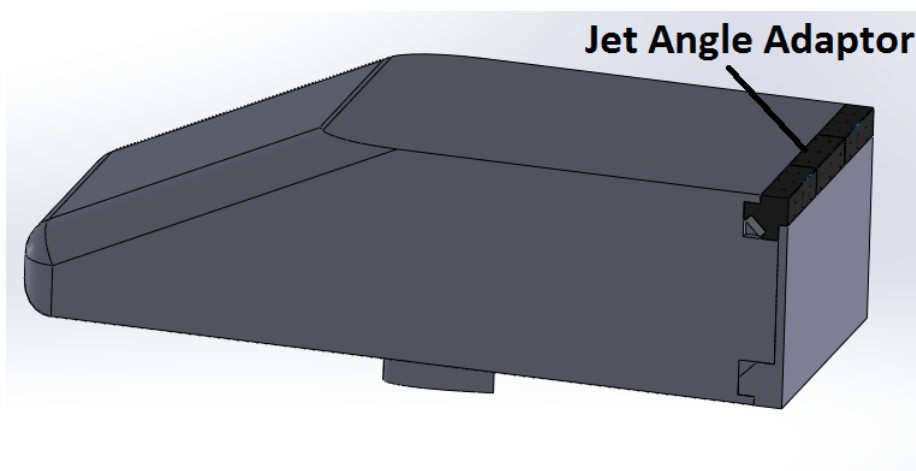


Figure 6.2 - Model of Windsor model with jet angle adaptor located at roof trailing edge

The circular outlet of each valve was positioned as close as possible to the jet angle adaptor and the valve outlet was gradually blended into the rectangular jet outlet section using internal ducting formed from the rapid prototype material (Figure 6.3). This ducting was also used to direct the air outlet angle

of the jet (i.e. 45 degrees up or 45 degrees down). Figure 6.4 is a view from behind the model with the base panel removed showing the complete assembly inside the model. The same air feed lines were used to deliver air to the large cavity inside the model as shown in Figure 5.2.

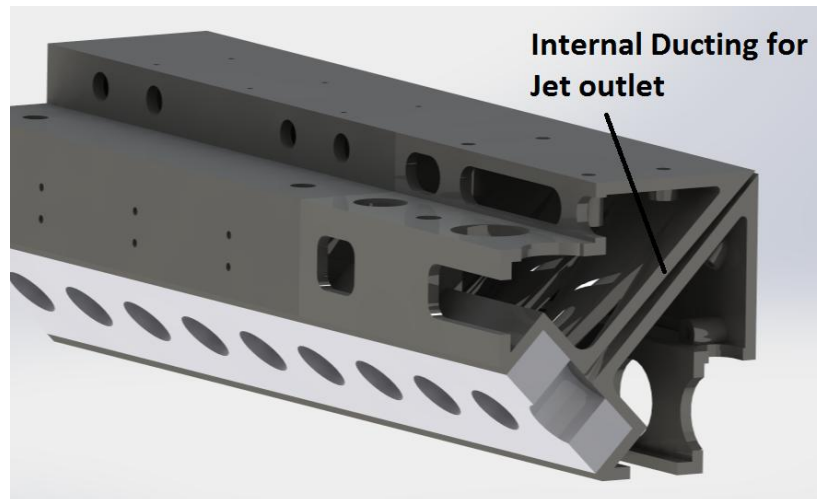


Figure 6.3 - Section view of jet angle adaptor showing internal ducting

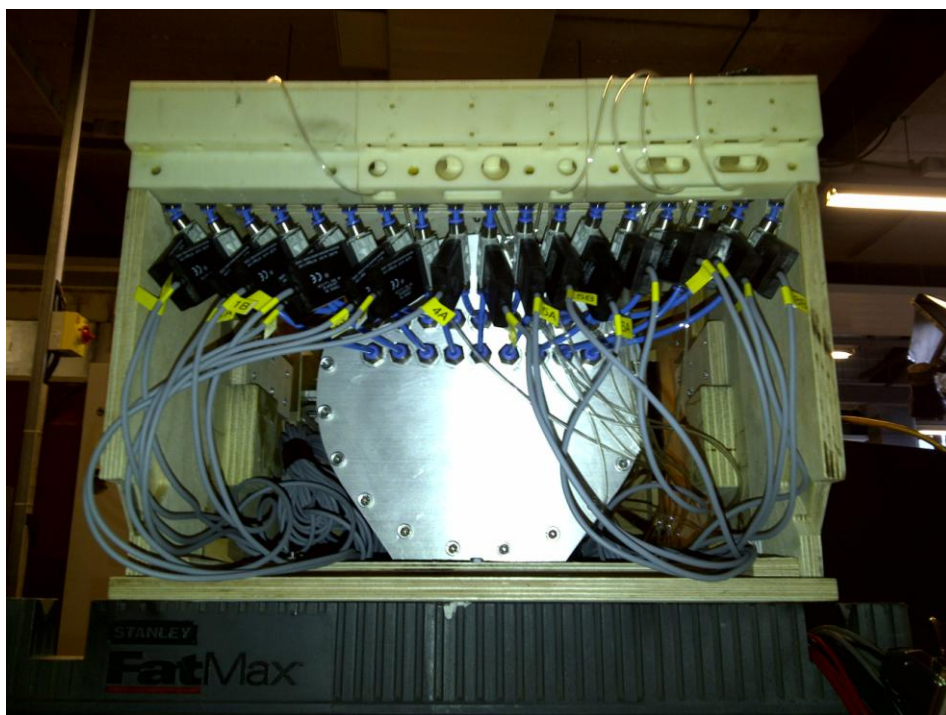


Figure 6.4 - View looking into rear of the Windsor model with the base panel removed

6.3 Jet Characterisation

The exit velocity of the jet was measured with a single wire hot wire probe using the same methodology as described in section 2.4 and was again conducted in quiescent conditions. The hotwire was traversed in 1mm steps along the length of the slot and the maximum slot exit velocity was averaged for use in the calculation of the jet exit momentum coefficient. The equation used for the momentum coefficient calculation in this application was the same as for a the blowing configurations given in Equation 5.1 and the peak jet exit velocity, spatially averaged over the outlet length was used. The jets were always driven such that the valve open times and the vale closed times were the same within one cycle of actuation.

Figure 6.5 shows an example of the measured exit velocity profiles over two full phases of the jet running at 10 Hz. Example measurements are given at 3 positions relative to the edge of one of the individual outlet sections. Positions 1, 3 and 5 show the velocity profiles at locations 1mm, 3mm and 5mm inside the edge of the outlet section. Figure 6.5 shows that near the outer edge of an outlet section the velocity magnitude is reduced, and this gradually increases until a position 5mm inside the outer edge, when the velocity magnitude stays constant as the hotwire is traversed closer to the centre of the outlet section. This reduction in outlet velocity at the edges is incorporated into the averaged peak outlet velocity calculated over the entire outlet length.

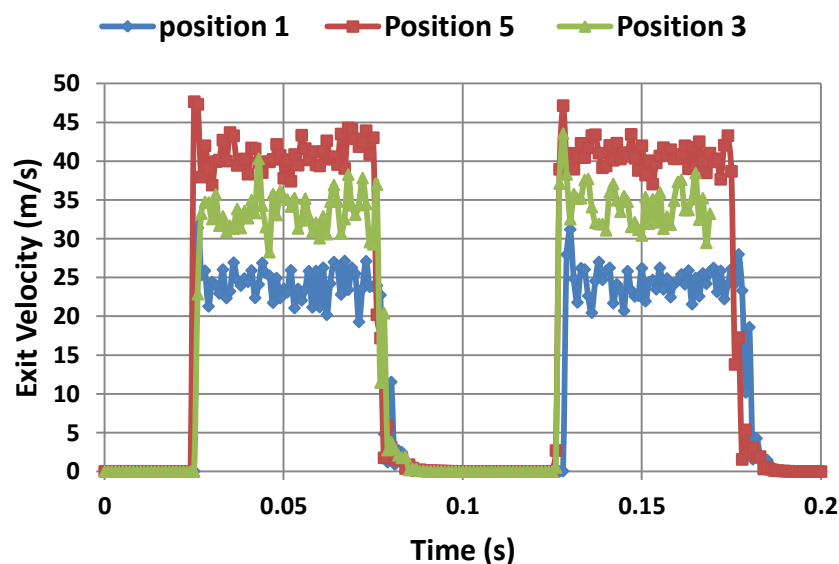


Figure 6.5 - Jet exit velocity profiles at different positions along an outlet section at 10 Hz actuation frequency

Differences in the velocity profiles compared to the SJ profiles shown in Figure 4.5 can be observed instantly. The synthetic jet produces a smooth sinusoidal shape, whereby the peak velocity is

achieved gradually and then the inward stroke pulls the outlet speeds back down to a minimum. For the pulsed jet configuration the outlet stroke is in the form of a square wave with a very fast development of the peak velocity as the valve opens, and a sharp reduction to 0m/s as the valve closes.

During the ‘valve closed’ section of the cycle the measured velocity is 0m/s indicating that the valves form a good seal and no leakage occurs. Using position 5 as an example; as the valve opens a large pulse of velocity is measured up to ~47m/s. This pulse quickly settles to an almost constant value of ~41 m/s. For lower frequencies such as the 1Hz signal shown in Figure 6.6 a slight decay in the exit velocity can be observed over the ‘valve open’ section of the cycle. This effect has been minimised by using as large a pressurised cavity as physically possible but some effect is still present. Even though this decay is present the mean outlet velocity throughout the outlet phase of the cycle is 41m/s. The fact that the average outlet velocity at 1Hz is the same as at 10Hz demonstrates that it is possible to achieve consistent momentum coefficients whilst modifying the actuation frequency of the jets. This was controlled via the measurement and control of the pressure in the cavity that supplies the jet outlets.

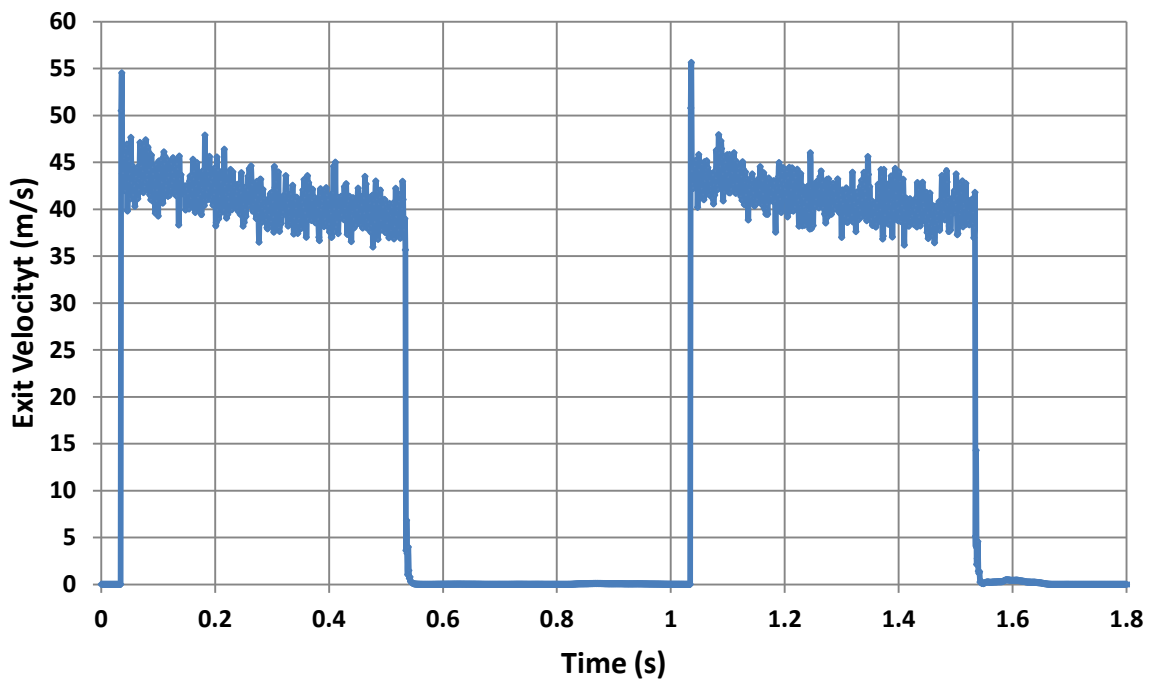


Figure 6.6 - Jet exit velocity profile at position 5 for an actuation frequency of 1Hz

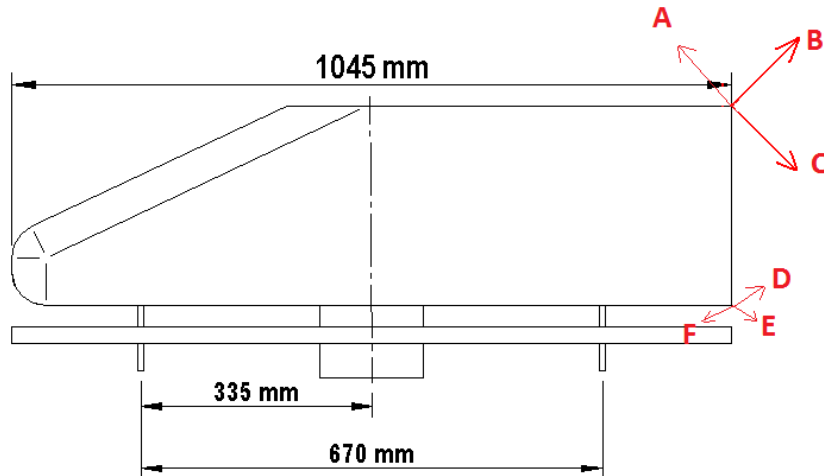


Figure 6.7 - Pulsed jet orientations tested

The configurations tested are shown in Figure 6.7 and actuation frequencies between 0.25Hz and 25Hz were tested. Although the valves were capable of operating faster, the LabView cards available were not able to drive the valves faster than 25Hz. The ride height tested was fixed at 10.3%. The application of wool tufts to the outlet of the jets showed that configurations C and D showed the same jet vectoring behaviour discussed in section 5.2.1. Figure 6.8 shows two frames from a video of the actuator running in configuration D where the wool tufts are settled horizontally in the valve closed state, and then curved upwards towards the base surface in the valve open state.



Figure 6.8 – Images of wool tufts at slot exit for configuration D, for A) valve closed state B) valve closed state

6.4 Balance Results

The thrust force produced by each jet configuration and actuation frequency was measured in quiescent conditions. This force was averaged over a 1 minute period and was subtracted from the forces measured during the wind on measurements with the jets active. Figure 6.9 shows the Results for configuration B where it could have been expected that the drag would increase.

At the low actuation frequency range of 0.25Hz -1Hz there is an increase in drag of ~10-12 counts for the $C_{\mu}=0.0066$ case and ~18-21 counts for the $C_{\mu}=0.0117$ case. These Changes correspond to a percentage change of 3.5-4% and 5.5-6.5% for the two momentum coefficients respectively. The C_{μ} values of the current pulsed tests of 0.0066 and 0.0117 also correspond to a jet exit velocity to freestream velocity ratio of 0.75 and 1 respectively.

This condition is similar to a steady blowing experiment with a reduced duty cycle and the changes in drag can be compared to the result seen in Figure 5.9a; for steady blowing velocity ratios of between 0.75 and 1 at a 10.3% ride height. On initial comparison the data seems to match up and the steady blowing experiment creates an increase in drag in these velocity ratio regions with magnitudes of ~4% for $0.75V_j/V_0$ and 6% for $1V_j/V_0$.

This is an interesting result when considering the duty cycle of the jets. One might have expected to see a reduced effectiveness by effectively reducing the time that the jets are turned on for. Knowing that the valve open time is identical to the valve closed time this is analogous to a 50% blowing duty cycle and anything up to a 50% reduction in the increases in drag might have been expected. It may be the case that the low frequency actuation and long period of the blowing outlet phase sets up some stability in the changes created in the wake, and as such the changes stay effective for a short period as the valves are closed. This would mean that drag changes created by constant blowing could also be possible using a 50% duty cycle, and hence reducing the input energy required for the system.

As the actuation frequency is increased the coefficient of drag is gradually increased. This result is also somewhat surprising as the momentum coefficient, the velocity ratio, and the effective duty cycle of the jets are staying constant. This means that whatever change is taking place must be as a direct result in the change in actuation frequency. This behaviour is seen at both Reynolds numbers, and Momentum coefficients tested (40m/s $C_{\mu}=0.0066$ and 30m/s $C_{\mu}=0.0117$). Further examination of PIV data is used to investigate this trend in section 6.5.

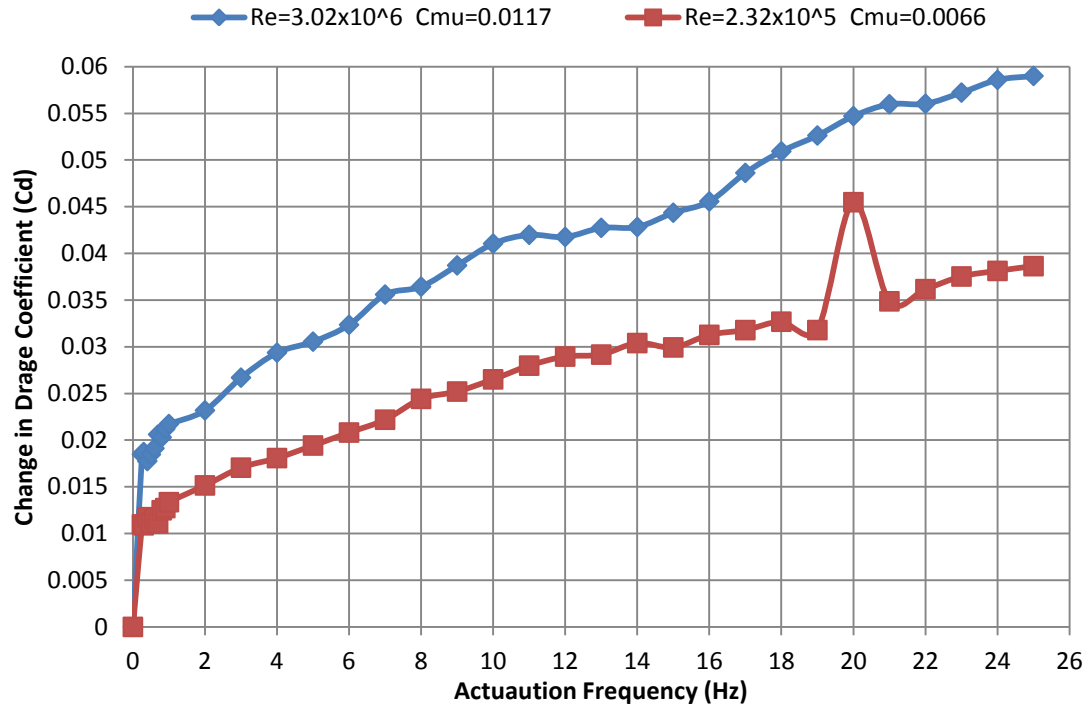


Figure 6.9 - Change in drag coefficient vs actuation frequency for configuration B

Figure 6.10 shows the changes in drag for configuration C, which produced a significant saving in drag for the steady blowing experiments. As per configuration B the lower frequency range of 0.25Hz to 1 Hz produce similar results to the steady blowing experiments with initial reductions in drag. For the larger momentum coefficient of 0.0117 the drag is reduced up to 1Hz actuation frequencies and increased after that, but for the lower momentum coefficient drag is increased at any actuation frequency above 0.5Hz. When drag is reduced in this region the savings are only ~2% and 4.5% for the low and high momentum coefficient actuation configurations respectively. When comparing this to the steady blowing results shown in Figure 5.10 these savings are 30-60% lower than the savings achieved with steady blowing at the equivalent velocity ratios (0.75 and 1).

As the frequency of actuation is increased the drag is gradually increased for both Reynolds numbers and actuation momentum coefficients. The drag increases gradually and almost scales linearly with increasing actuation frequency. Clearly the introduction of pulsed flow into the wake is having some effect which becomes gradually stronger as a function of the applied frequency.

Following the low frequency actuation regions (0.25-1Hz) this steady increase in drag with actuation frequency also has significant magnitude for both configuration B and C. In fact, configuration C which may have been expected to produce drag saving characteristics, ends up increasing drag by up to 12% at 25Hz.

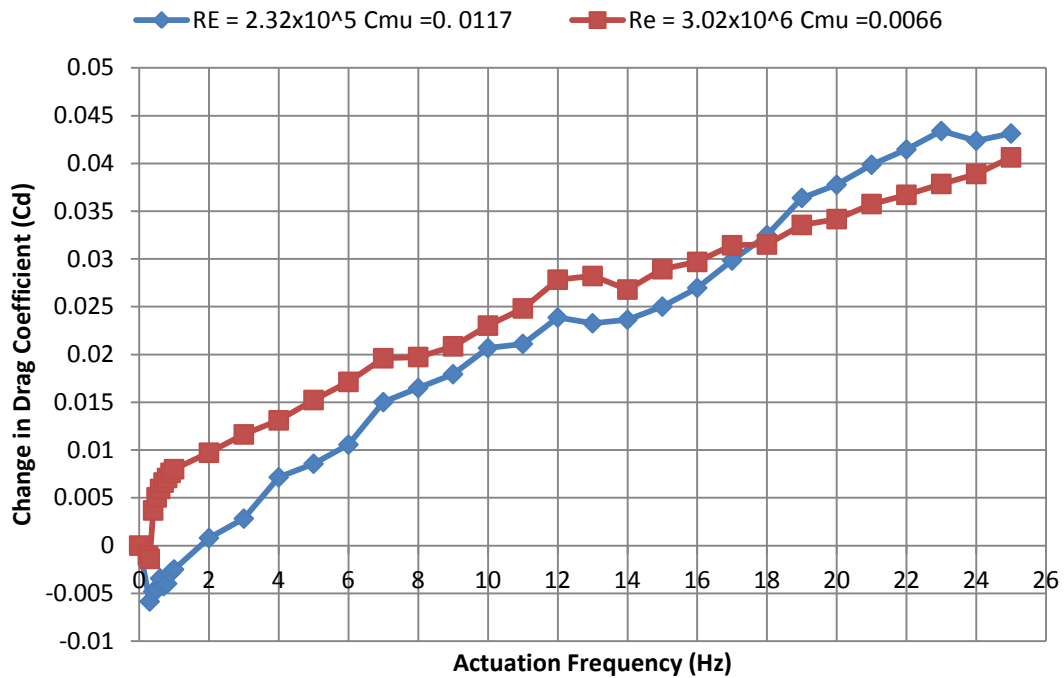


Figure 6.10 - Change in drag coefficient vs actuation frequency for configuration C

Configurations D,E and F were incorporated to investigate if the strength of the lower vortex structure could be disrupted by applying pulsed blowing at the floor trailing edge. Figure 6.11 shows the balance results for these configurations and shows configurations E and F only ever increase the total amount of drag. For both E and F the initial application of pulsed blowing creates a sharp increase in drag coefficient with respect to the baseline configuration, but Configuration F has a much larger effect than configuration E. The significant effects seen in configuration F are a result of the significant disruption applied to the underbody flow by the forward facing jets, where as the effects created from jet configuration E are somewhat more subtle.

As frequency is increased whilst maintaining a fixed momentum coefficient, drag changes are gradually increased for both configurations, but again the forward facing jets of configuration F create greater gradient of change than configuration E.

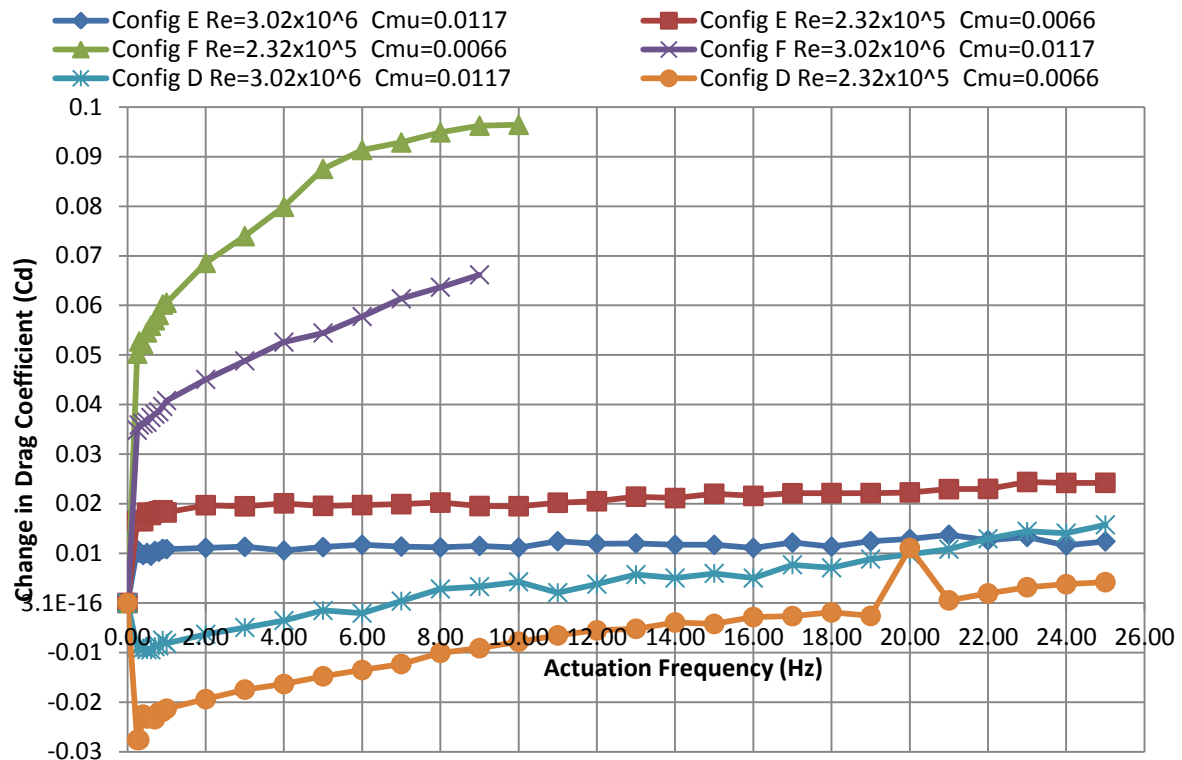


Figure 6.11 - Change in drag coefficient vs actuation frequency for configuration D,E and F

The most interesting result occurs in configuration D where a significant reduction in drag is achieved for the lower actuation frequencies. For momentum coefficients of 0.117 drag reductions occur up to actuation frequencies of 20Hz, and magnitudes of drag reduction are as much as 9.5%. For the lower momentum coefficient drag in only decreased up to 6Hz.

Unfortunately the behaviour linked to increases in actuation frequency is also seen in this configuration and eventually the drag reductions become drag increases. Whatever the mechanism is that creates the initial drag saving may be, (whether it is wake size reduction or manipulation of the lower vortex strength) it is eventually negated by the effects of increasing the actuation frequency of the jets. A more detailed study of the resultant in-wake structures is required and PIV data will be used to try to identify how increased jet actuation frequency increases drag.

6.5 PIV

The main question resulting from the balance measurements is why the drag coefficient was consistently increased with increasing actuation frequency no matter what the configuration of the jet orientation was.

6.5.1 Configuration B

From the previous chapters it has been identified that total body drag can be modified by modifying the base pressure distribution. The main area to be targeted is the lower half of the base where surface pressure distributions can be modified by changing the position and strength of the lower vortex. In addition to targeting this vortex overall wake size will influence the global base pressures.

PIV data for configuration B, for steady blowing, 10Hz actuation and 25Hz actuation is shown in Figure 6.12. The data shows vorticity values as a contour plot with velocity vectors in the foreground. With steady blowing it is seen that the wake is large with the shear layer being deflected up and out of the top of the FoV (as shown in section 5.8) As the actuation is changed from steady blowing to a pulsed actuation at 10 Hz the total wake size is actually reduced, with the upper shear layer seemingly being turned downwards by the cyclic actuation. The wake size continues to be reduced slightly as the actuation frequency is increased from 10Hz to 25Hz.

In addition to the wake size being reduced when the blowing is pulsed the total size of the lower vortex is also reduced (which is the opposite of what one might expect from the previous blowing investigations) as the drag increases with increasing actuation frequency.

At 10Hz the lower vortex interacts with the base up to $h/H \sim 0.7$ and at 25Hz the lower vortex only reaches up to $h/H \sim 0.65$. However as the size of the wake is reduced the levels of vorticity in the lower vortex increase; at 10Hz there is clockwise vorticity near the base from $\sim 200-250\text{s}^{-1}$ but at 25Hz the clockwise vorticity near the base surface is increased to $250-300\text{s}^{-1}$. In addition to an increase in levels of clockwise vorticity in the mid-lower half of the wake, the anticlockwise vorticity in the upper half of the wake is also increased by the application of pulsed blowing. At an actuation frequency of 25Hz, levels of clockwise vorticity close to the base surface above $h/H=0.65$ are of a magnitude between $100-300\text{s}^{-1}$.

From the data presented in Figure 6.12 it appears that as actuation frequency is increased the strength of the vortical structures close to the base surface is increased. As the strength of these vortices is increased the base surface velocities will be increased and base surface pressures will be decreased as a result. In order to try to quantify the increase in vortex strength the vorticity levels close to the base are analysed further.

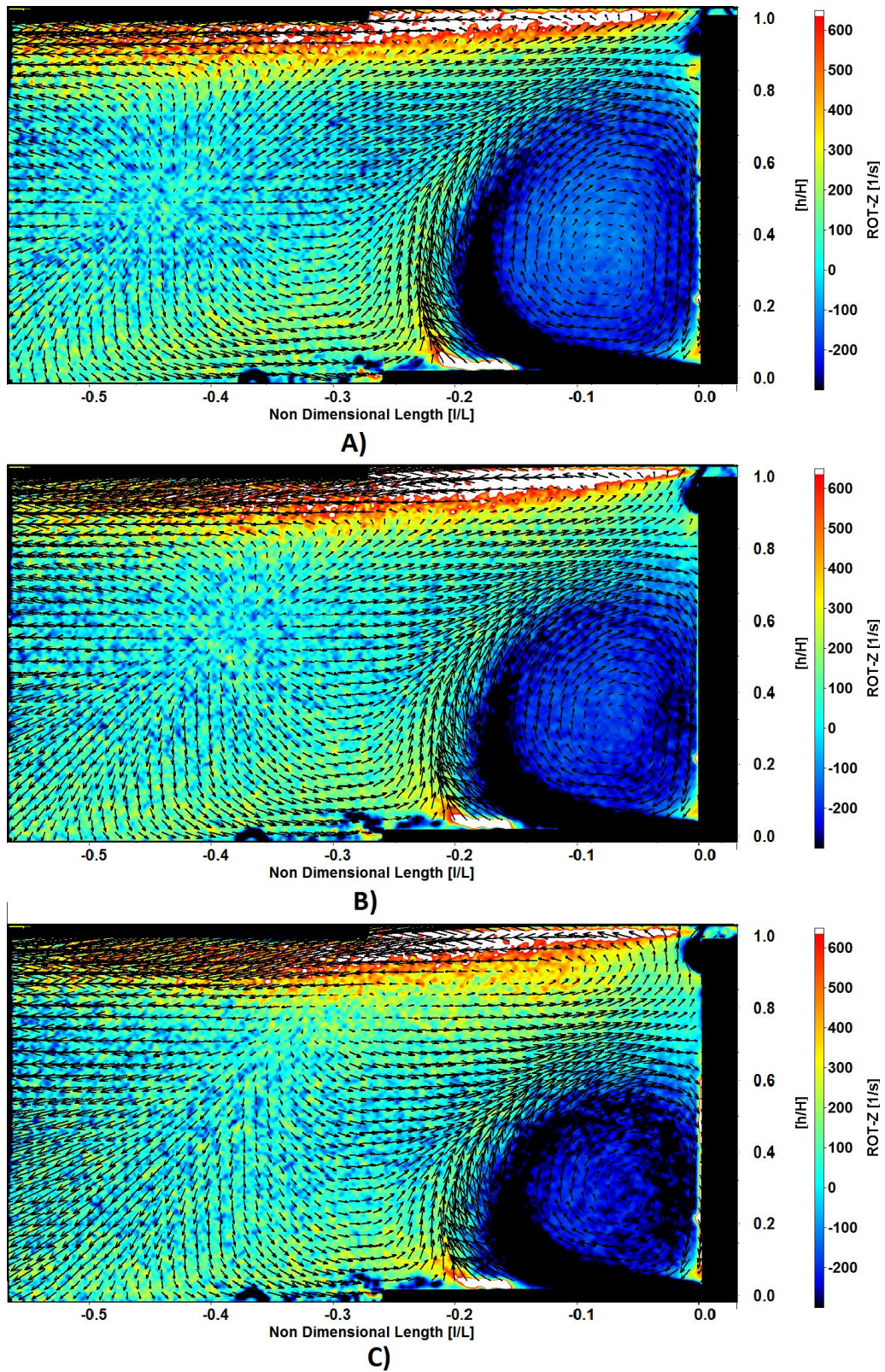


Figure 6.12 - PIV vector fields with vorticity contours in the background for jet orientation B, with the jet running at $C_{\mu}= 0.0066$ as: A) steady blowing; B) Pulsed 10Hz actuation and C) Pulsed 25Hz actuation

An area of interest close to the base surface was identified for investigating the vorticity levels further. The vorticity data at each grid position within this region of interest was extracted and the average level of vorticity could then be plotted.

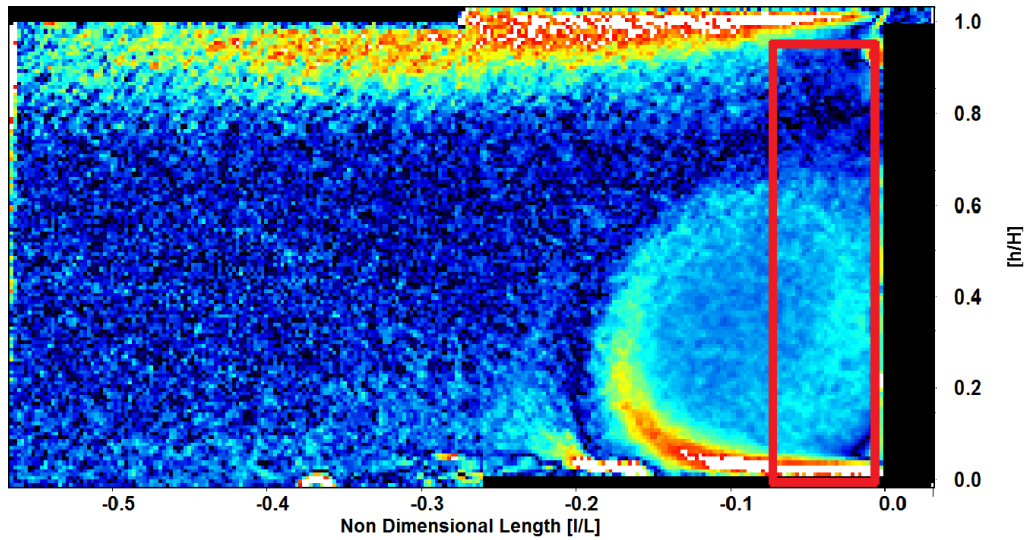


Figure 6.13 - Example data set of positive vorticity with region of interest used for averaging shown in red

The region contains both positive and negative vorticity values and in the current configuration it appears both the upper and lower vortices are being strengthened with the application of pulsed blowing. So that the positive and negative vorticity did not cancel out in the averaging process the images were squared and then square rooted to produce only positive vorticity values. The region of interest used is shown in Figure 6.13 with the positive vorticity values in the background. The averaged positive vorticity magnitude for different jet conditions in configuration B is plotted in Figure 6.14.

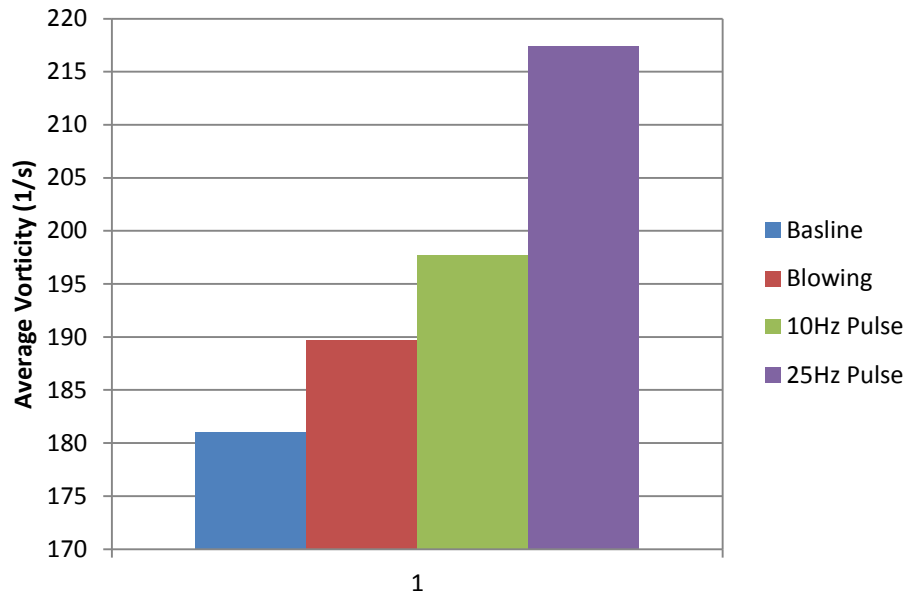


Figure 6.14 - Averaged vorticity within region of interest for configuration B

Figure 6.14 shows that as steady blowing is introduced, the mean levels of vorticity in the region of interest increase relative to the baseline configuration. As the jets are pulsed at 10 Hz vorticity levels increase and as actuation frequency is increased to 25Hz the vorticity increases again. The jump of 15Hz between the 10 Hz configuration and the 25Hz configuration can also be seen in the vorticity levels as the magnitude of increase is larger than the increase between the blown case and the 10Hz actuated case.

The increases in vorticity levels, and increases in the overall wake size, that occur when steady blowing or low frequency pulsed blowing is applied in the current configuration explains why there is a large initial increase in drag relative to the baseline configuration. The fact that drag gradually increases as the pulsed actuation frequency is increased (even though there is an apparent wake size reduction) can be linked to the gradual increase in the levels of vorticity close to the base, or in the region of interest examined. This increase in vorticity will result in increased suction on the base surface where the vortical structures interact with it.

The same examination of vorticity levels in the near wake will be applied to configurations C and D to try to corroborate the link between vorticity, vortex strength and surface velocities with a reduction in base pressures.

6.5.2 Configuration C

For configuration C the vorticity levels are shown in Figure 6.15 for the 10Hz, 15Hz and 25Hz pulsed blowing cases. The overall wake size is seen to reduce between the baseline configuration and the

10Hz pulsed jet results. The wake size also continues to reduce even between the 10Hz and 25Hz cases, which is seen as the shear layer being deflected downwards. This wake size reduction is occurring as the total drag force is increasing (Figure 6.10).

The overall size of the lower vortex structure remains relatively constant as actuation frequency is increased with the top of the structures located $\sim h/H = 0.65$ (Figure 6.15). The levels of clockwise vorticity within the lower vortex gradually increase with frequency shown by the appearance of more black contour plot regions. In addition to the increases in vorticity in the lower wake the levels of anti-clockwise vorticity in the upper wake are increase, shown as more yellow regions of the contour plot close to the upper base surface.

The averaged magnitudes of vorticity within the region of interest shown in Figure 6.13 are plotted in Figure 6.16 for configuration C. This plot also shows a link between the levels of vorticity and the increasing drag forces associated with increased actuation frequency (Figure 6.10). The level of vorticity for the low frequency actuation at 1Hz is slightly reduced relative to the baseline case but the magnitudes of change are not significant. As frequency is increased so too do the levels of vorticity by up to 40s^{-1} which reinforces theory that there is a direct link between the increasing drag forces with the increased vorticity observed as actuation frequency increases.

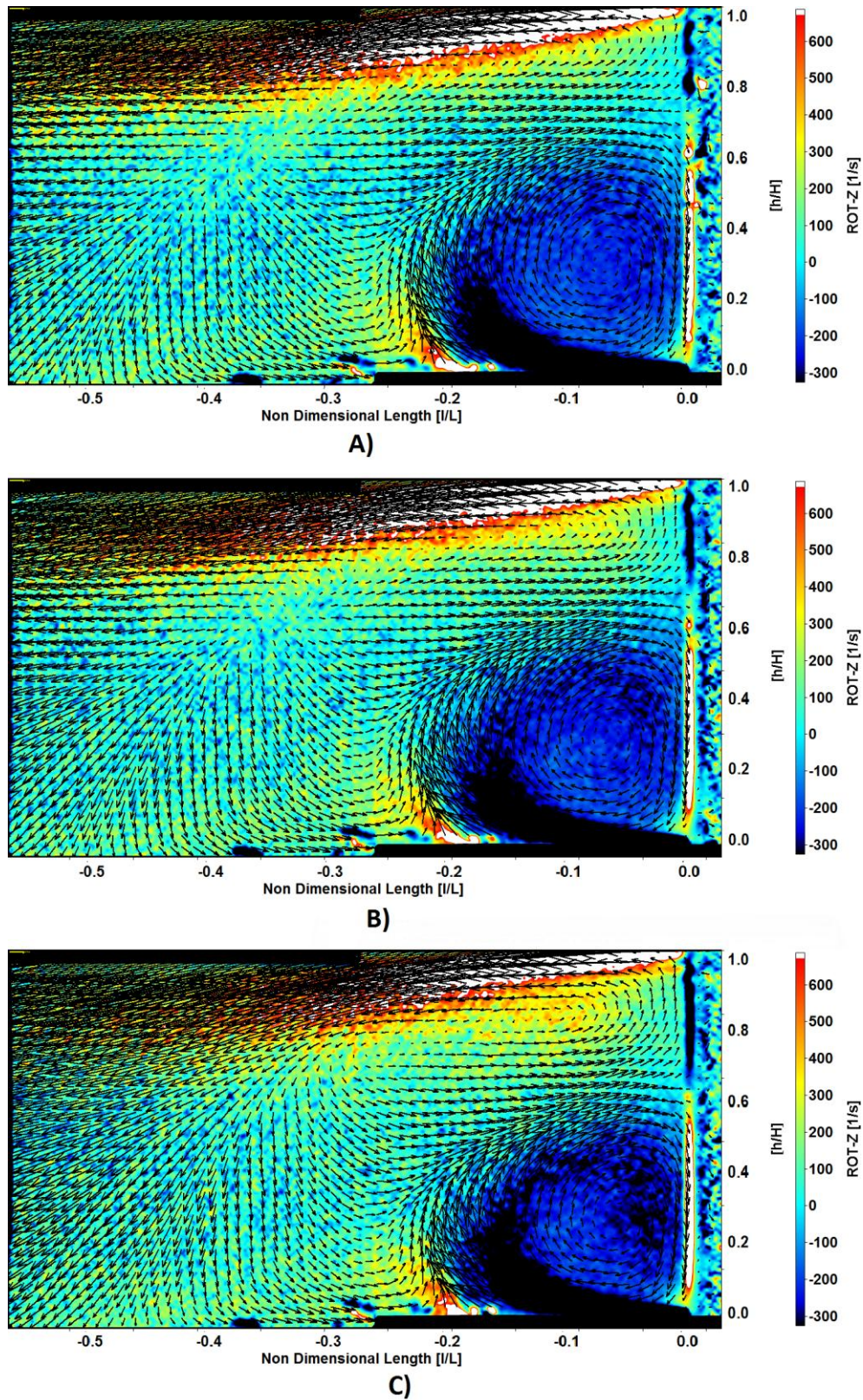


Figure 6.15 - PIV vector fields with vorticity contours in the background for jet orientation C, with the jet running at $C_{\mu}= 0.0066$ as: A) Pulsed 10 Hz actuation; B) Pulsed 15Hz actuation and C) Pulsed 25Hz actuation

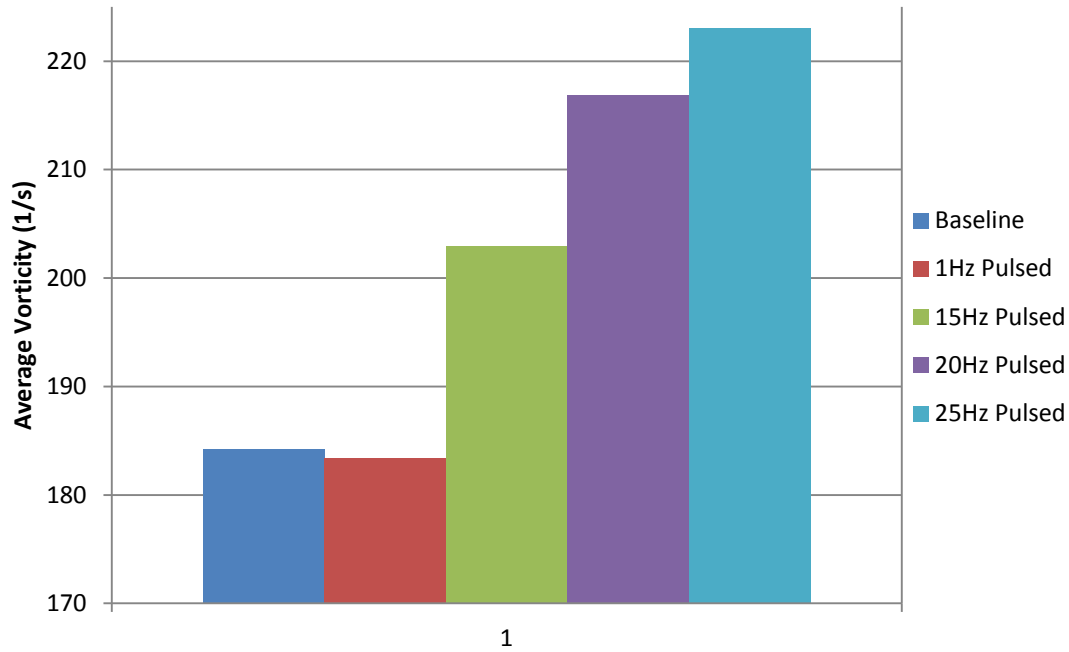


Figure 6.16 - Averaged vorticity within region of interest for configuration C

6.5.3 Configuration D

Configuration D showed significant reductions in drag for the lower actuation frequencies with the characteristic increase in drag at higher frequencies. On examination of the PIV data (Figure 6.17) for the lower frequencies it can be seen that the wake size does not change significantly relative to the baseline, however the vorticity in the lower vortex is reduced. It is only at the higher frequency of 25Hz where the upper shear layer is seen to be deflected upwards and increases the overall wake size. In addition to the increase in wake size a significant amount of vorticity is seen in the lower vortex at 25Hz.

The rotational energy in the lower vortex is reduced at lower actuation frequencies by virtue of the direction at which the jet exits. The actual outlet direction of the jet is ~ 10 degrees off vertical (see Figure 5.6) which would oppose the downward flow along the base surface created by the lower vortex. As actuation frequencies are increased the jet becomes less able to oppose the downward flow direction created by the lower vortex and the effects created by pulsing the flow dominate, leading to an increase in the lower vortex strength.

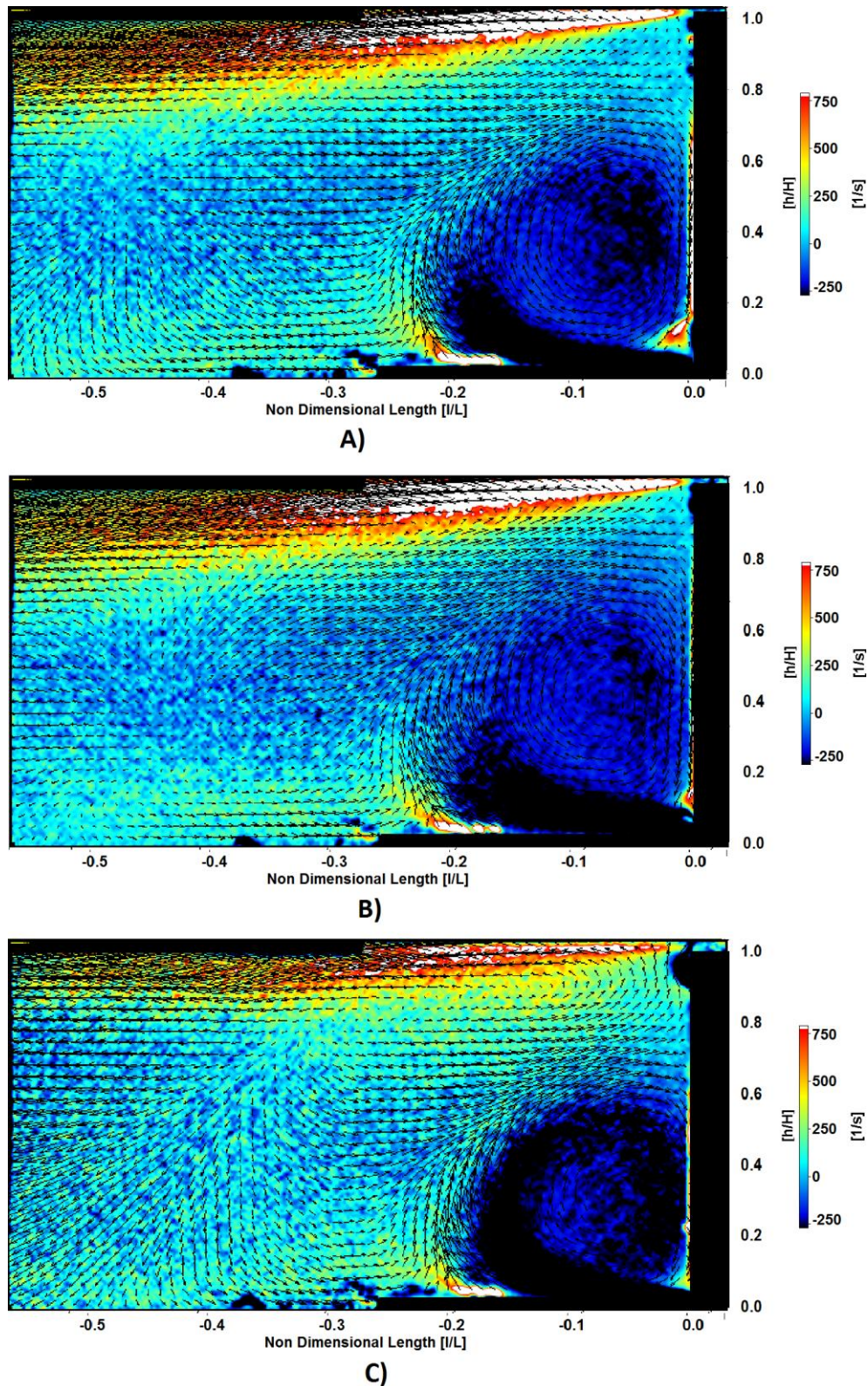


Figure 6.17 - PIV vector fields with vorticity contours in the background for jet orientation D, with the jet running at $C_{\mu}= 0.0066$ as A) Baseline flow case, B) Pulsed 1Hz actuation and C) Pulsed 25Hz actuation

The averaged magnitudes of vorticity within the region of interest shown in Figure 6.13 are plotted for the current configuration. The changes in mean vorticity correlate very well with the overall changes in drag shown in Figure 6.11. At low actuation frequencies the vorticity is reduced relative to the baseline, as the jet opposes the flow created in the lower vortex. At higher actuation frequencies of 10Hz and 25Hz the vorticity is higher than the baseline flow case, as the vorticity in the upper and lower structures increase as a result of the pulsed jet.

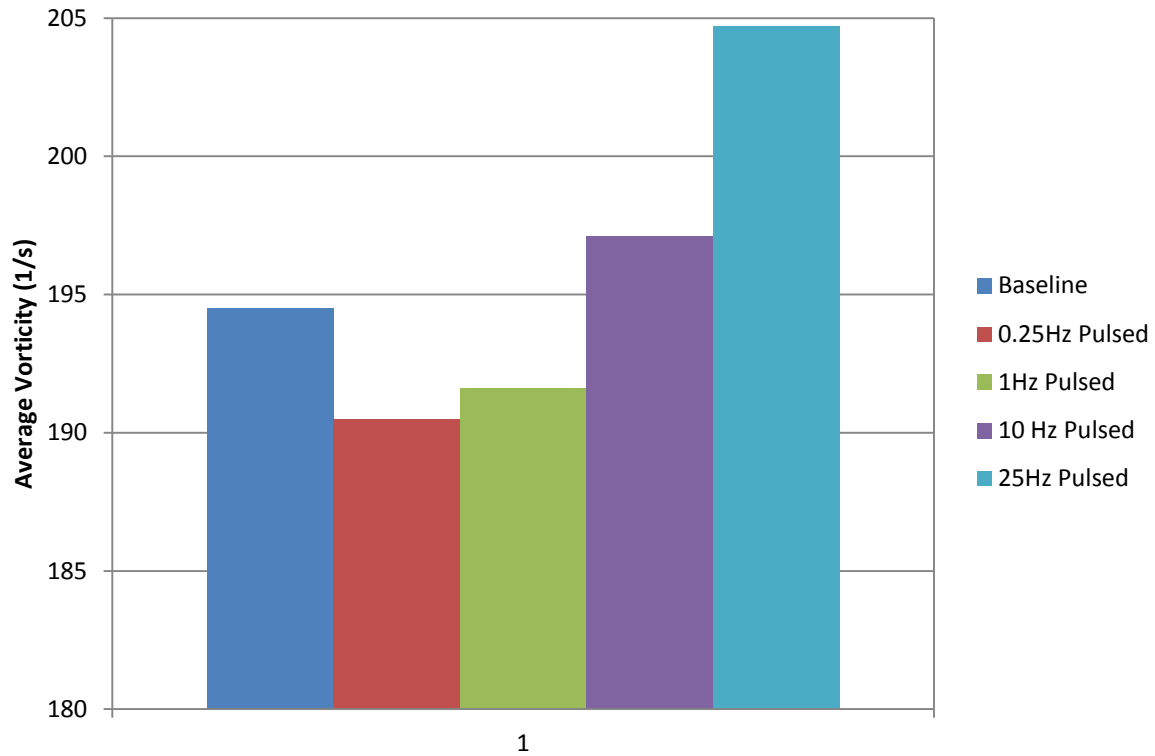


Figure 6.18 - Averaged vorticity within region of interest for configuration D

6.6 Discussion

A number of configurations have been investigated using pulsed blowing at the rear edge of the model. Some configurations created drag reductions where the lower vortex strength was reduced. Where the jet acted to deflect the upper shear layer upwards, consistent drag increases were observed.

An interesting link has been found between the actuation frequency and a gradual increase in drag; as frequency is increased drag is increased for all cases. This behaviour is attributed to the increase in vorticity close to the base surface that occurs as frequency is increased. An averaging process applied to the derived vorticity within the PIV data has shown good correlations between the measured body forces, and the actuation frequency. It would be of interest for further work to increase the actuation frequencies further to investigate if the trend continues or if some other regime is established.

The required mass flow has been reduced by pulsing the jets, however in all cases where a drag reduction occurred, the savings were also reduced. The switching of the valves requires an energy input and as such the pulsing of the jets does not offer any improvement over the standard blowing system.

The additional investigations carried out at the lower edge of the model have again shown that drag can be reduced if the energy within the lower vortex structure is manipulated. The previous investigations with active blowing and pulsed blowing create questions regarding if this effect can be created passively. Potentially this could be achieved using ducted freestream flow, or alternatively the lower vortex strength could be disrupted with some form of discrete shape change on the base surface.

Chapter 7

**PASSIVE CONTROL OF IN WAKE STRUCTURES
EXPERIMENTS, RESULTS AND DISCUSSION**

7.0 Passive Control of In Wake Structures – Experiments, Results and Discussion

7.1 Introduction

In the experiments conducted in the previous Chapters it has been shown that the manipulation of the vehicle wake size alone is not the only factor that will influence base pressures. The large lower vortex structure in the near wake of the model is consistently linked to a region of low pressure on the base. In the previous chapters it has been argued that reducing the vorticity of this structure can cause an increase in base pressure, and in fact an increase in vorticity introduced by pulsed jets will actually increase the drag force on the body. It has also been argued that applying constant blowing from the upper rear roof trailing edge to reduce the vorticity creates a reduction in the downward flow velocity moving over the base surface, which in turn creates a drag reduction.

It is clear the way in which the lower vortex structure interacts with the base surface plays a large role in creation of the level of negative pressure on the base surface. The same dependence of base surface pressures on vortex structure interaction has been observed by other authors (Bearman, 1965) (Pastoor et al., 2008) and the manipulation of this interaction has been used to change vehicle drag forces. In the current chapter small passive features are added to the lower half of the base surface to try to manipulate the way in which the lower vortex structure interacts with it. The intention is to reduce the downward flow velocity over the base surface and reduce vorticity, causing an increase in base pressures. The fact that these passive modifications do not require an energy input means that any saving found here will all directly contribute to a reduction in the vehicle power requirements.

In addition to testing at model scale there was a short opportunity to test the theories outlined below at full scale on a production vehicle to investigate if the effects observed scale efficiently.

7.2 Experimental Configurations

7.2.1 Model Scale

The standard configuration of the base surface on the Windsor model is flat and perpendicular to the onset flow direction. As a means of testing the theory that disrupting the lower vortex structure can induce a drag saving some simple passive modifications to the Windsor model were designed. For the different configurations the model was fitted with small 1mm thick, 8mm deep ‘slats’ on the lower half of its base surface, as shown in detail A of Figure 7.1. The first slat added was positioned 35mm

above the model floor and additional slats were spaced 35mm apart. The configurations tested are described in

Table 7.1. The slats were designed to act as a small trip type device to interrupt the lower vortex flow. All the other geometry of the model remains as per the previous chapter, including the NACA0021 wing profile in the centre of the model floor.

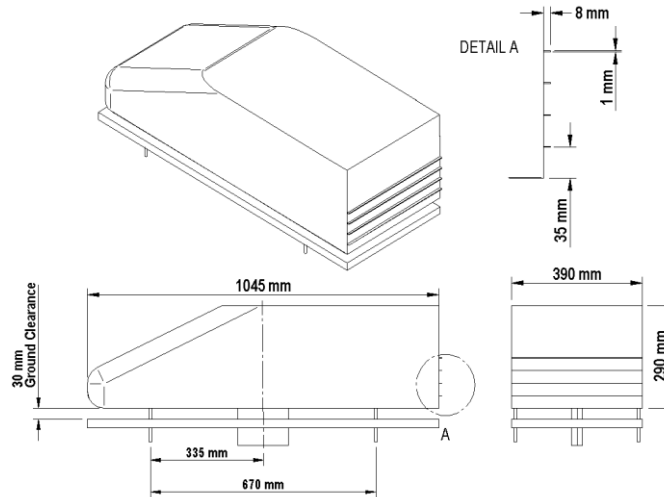


Figure 7.1 - Windsor model illustrating the position of slats

Table 7.1 - Scale model configurations

Configuration Number	Description
0	Baseline configuration no slats added to model
1	3 Slats added to the base surface of the model spaced evenly 35mm apart from the floor of the model
2	4 Slats added to the base surface of the model spaced evenly 35mm apart from the floor of the model

7.2.2 Full Scale Vehicle Testing

The opportunity arose to test the ‘slats’ at full scale to see if the effects would scale to a production vehicle scale. In order to replicate the ¼ scale tests as closely as possible the overall proportions of the test vehicle were selected to match closely with the Windsor model. The vehicle selected was a commercially available square back MPV (Ford S-Max). In addition to trying to match the overbody

vehicle shapes to the model scale tests a false flat floor was fitted the vehicle underbody. The standard underbody of the vehicle used had very limited aerodynamic optimisation and incorporated several large voids and a non smooth floor. Figure 7.2 shows images taken from underneath the vehicle whilst it was parked on a car lift, with and without the underbody smoothing in place.

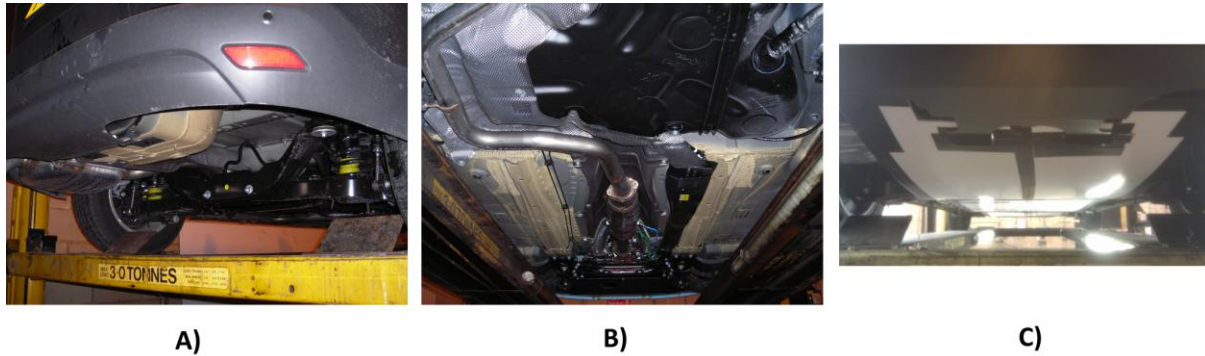


Figure 7.2 - Images showing vehicle under floor: A) standard rear floor section; B) Standard central floor section and C) Smoothed floor section viewed from rear of vehicle looking forwards

It was deemed necessary to smooth the underfloor to create some form of the stable vortex structures seen in the model scale wake flows; it was believed the very ‘rough floor’ of the standard vehicle may inhibit the formation of these stable structures, or at least make them less stable.

Experiments were conducted in the MIRA full scale test facility which is a fixed floor, closed working section, open return wind tunnel. The vehicle wheels were not rotating during the tests. The working section of the tunnel is 7.94m wide and 4.42m high, giving a blockage ratio of 7.6%, using the manufacturer’s quoted frontal area of 2.65m². Tests were performed at freestream velocities of 22.4, 26.8 and 31.3m/s (50, 60 and 70mph). Force measurements were made using a six component under-floor balance and corrected for blockage using the standard MIRA blockage correction method (Equation 2.4). 30 surface pressure ‘spades’ (see Figure 7.3) were positioned across one half of the vehicle base and were connected via flexible tubing to a single 64 channel pressure scanner mounted inside the vehicle. The scanner was powered using a transformer wired into the standard in cabin power supply. The scanner specification was identical to that used in the model scale testing and measurements were non-dimensionalised using a pitot static tube located upstream of the vehicle. The pressure measurements were corrected using Equation 2.6.

The configurations tested at full scale consisted of adding up to six 30mm deep slats across the width of the base as shown in Figure 7.3. The configurations tested are described in

Table 7.2. and all the configurations were tested with both a smooth under floor and the standard vehicle underfloor.



Figure 7.3- Full scale test vehicle shown in configuration 1 with pressure ‘spades’ attached to one half of the vehicle base surface

Table 7.2 - Full scale vehicle configurations

Configuration Number	Description
0	No slats fitted baseline vehicle configuration
1	6 Slats fitted to the base surface of the vehicle as shown in Figure 7.3
2	5 slats fitted to the base as per configuration 1 but with the upper slat removed
3	4 slats fitted to the base as per configuration 1 but with the upper slat removed
4	3 slats fitted to the base as per configuration 3 but with the upper slat removed
5	2 slats fitted to the base as per configuration 4 but with the upper slat removed
6	1 slat fitted to the base as per configuration 5 but with the upper slat removed

7.3 Experimental Results

7.3.1 Model Scale

The balance measured change in C_d relative to the baseline configuration for the scale model tests are shown in Figure 7.4. C_d values are accurate to ± 1 count and measured lift coefficients values are accurate ± 5 counts. Slats were only applied to the lower half of the base during the model scale experiments. These configurations were selected because of the previous data gathered at model scale showing the dominance of the lower vortex structure. Configuration numbers are as described in Table 7.1.

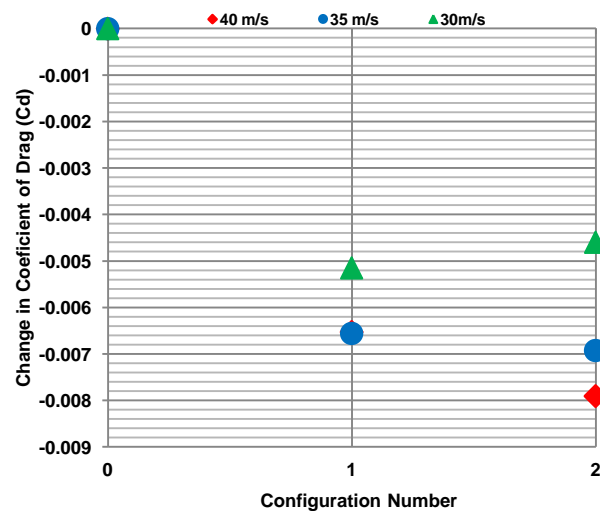


Figure 7.4 - Change in C_d from baseline vs configuration number

Figure 7.4 shows that the addition of slats to the base of the model reduces C_d by up to 8 counts for configuration 2. This is a considerable reduction in overall C_d for such a small shape change within the wake. Particularly as in previous studies (Duel and George, 1993) shape changes within the wake intended to modify the structures of the wake have been considerably larger than those employed here. This is another result that suggests that a significant drag change is the result of a modification to the structure of the wake, specifically the strong lower vortex structure.

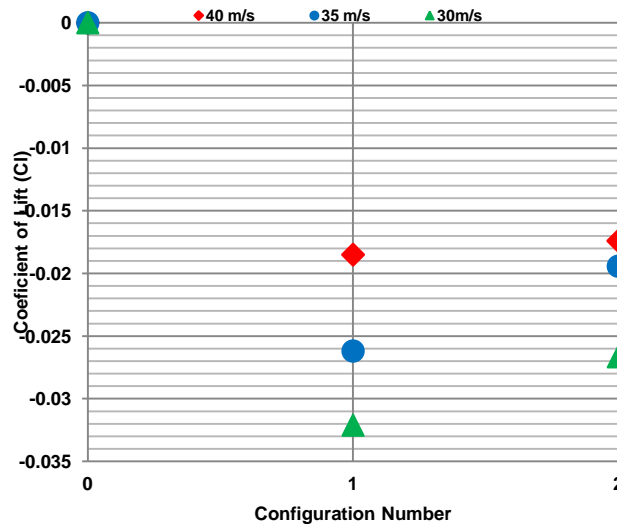


Figure 7.5 - Change in C_l from baseline

Figure 7.5 shows the vehicle lift coefficient, and the effect of the configuration changes relative to the baseline configuration. An initial observation is that the C_l values are much more sensitive to Reynolds number changes than the drag results, however they all follow a trend that with the addition of slats to the lower half of the base C_l is reduced. This is again a significant change in C_l for a relatively small shape change, and it supports the theory that disrupting the lower vortex in close proximity to the base will cause a base pressure increase. It is possible that small modifications at the rear of the model can cause changes in the stagnation point at the front of the vehicle which could account for the changes in lift, however looking at the balance of front and rear C_l changes this effect is only a small percentage of the overall lift change. The rear lift coefficient (C_{lr}) never contributes less than 80% to the total changes in C_l recorded. This indicates that changes in lift due to movement of the front stagnation point are small, and the majority of the lift changes occur because of changes to the wake structure effecting the flow around the rear section of the vehicle.

Figure 7.6 shows a contour plot of base pressure coefficients (C_p) for the baseline configuration (no slats) and Figure 7.7 shows the C_p distribution when four slats are added (configuration 2). The plots are oriented such that a view is taken looking from directly behind the model where zero on the x axis corresponds to the model centreline and zero on the z axis corresponds to the bottom of the model.

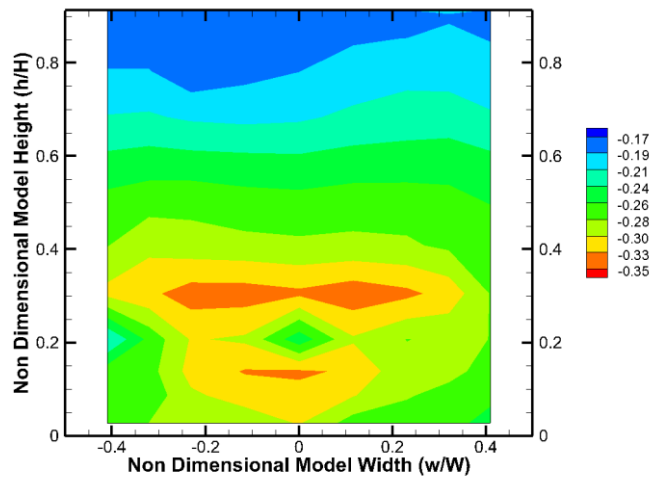


Figure 7.6 - C_p distribution on model base with no slats fitted (freestream velocity 40m/s)

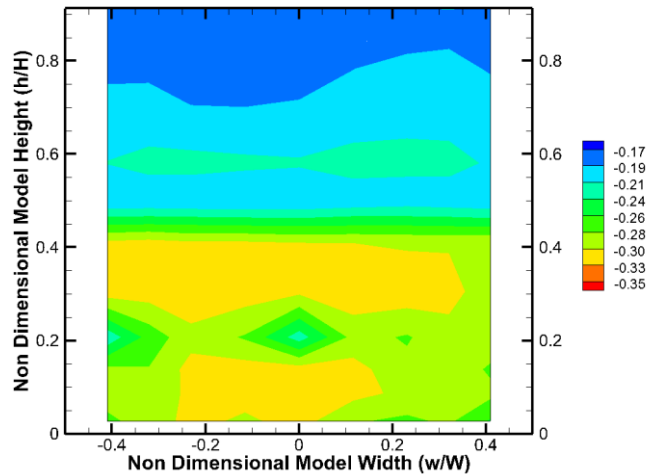


Figure 7.7 - C_p distribution on model base with 4 slats fitted (freestream velocity 40m/s)

The suction region created by the lower vortex structure can again be seen below $h/H=0.4$ in Figure 7.7. The flow is still largely two dimensional across the width of the model, with the presence of some three dimensional structures in the lower corners of the base. Figure 7.7 shows that when 4 slats are added the surface pressures become much more uniform across the width of the model, especially in the upper half of the base. It also seems to show a global increase in C_p , with the majority occurring within the upper base region. In order to more easily identify where increases in pressure occur the baseline pressure distribution has been subtracted from the pressure distribution for 3 slats, and the distribution for 4 slats, and the resulting plots are shown in Figure 7.8 and Figure 7.9 respectively.

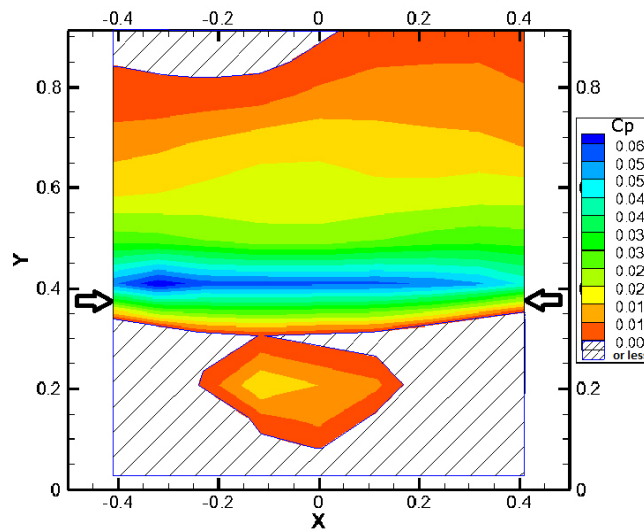


Figure 7.8 - Change in model base pressure relative to baseline configuration with 3 slats fitted (freestream velocity 40m/s)

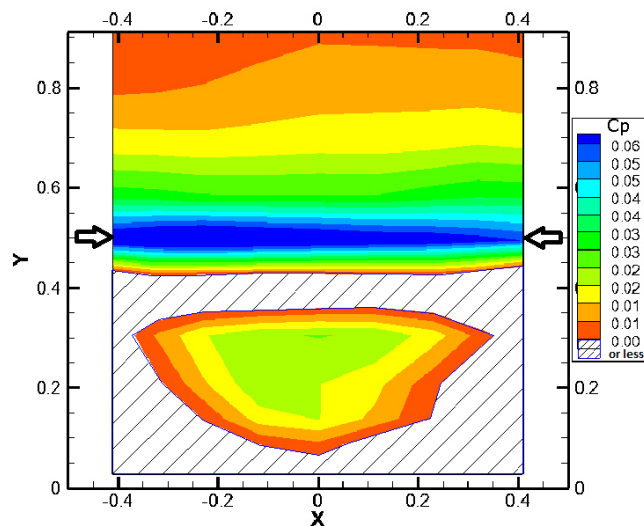


Figure 7.9 - Change in model base pressure relative to baseline configuration with 4 slats fitted (freestream velocity 40m/s)

For clarity any areas that showed no change or a slight decrease in pressure are identified by a hatched region, and the position of the uppermost slat is identified in each plot by two arrows. It is immediately apparent that a large region of increased pressure occurs along the width of the upper slats. It appears that the reversed flow from the lower vortex, seen in the earlier PIV results for the baseline flow, impinges on the upper slat when it recirculates back around towards the base surface. In doing so it creates a region of increased pressure above the slat which spreads upwards on the

upper half of the base. In this case the rotational energy within the vortex is being used to react with the slats introduced and create a more favourable pressure gradient on the base surface.

Additionally the suction at the centre of the lower vortex region between $x \approx -0.2$ to 0.2 and $y \approx 0.1$ to 0.5 in Figure 7.9 shows an increase in pressure. This pressure increase may be associated with a reduction in the rotational energy of the structure, and hence the velocity across the base surface. In this case reducing the energy in the vortex has two effects; one to create the increased base pressure seen above the slats, and another to reduce the suction component in the lower base half created as a result of the original interaction.

Note that the plots do not show an exact distinction between the pressure above and below the upper slat because of interpolation between tapping locations applied when generating the contours in Figure 7.8 and Figure 7.9.

7.3.2 Full Scale

While it was not the intention to directly reproduce every aspect of the model scale tests at full scale, to replicate the body model surfaces as closely as possible the full scale vehicle was fitted with a flat floor. This was considered important in order to generate stable recirculating structures within the wake of the vehicle. It is worthy of note that the addition of the flat floor alone created a drag reduction of 32 counts, which adds weight to the argument for flat floors being fitted on production vehicles. This magnitude of drag reduction also supports the findings of previous work (Le Good, Howell and Passmore, 1995).

When slats were added to the base of the vehicle without a smooth underfloor in place there was no change in drag that could be considered to be outside of measurement error (± 1.5 counts). This result illustrates that the mechanisms targeted by the addition of small slats in these tests are highly dependent on the conditioning of the flow before it separates from the rear edges of the vehicle. It suggests that if the separation location/line all the way around the vehicle is transient rather than fixed, the wake structures targeted never become sufficiently stable for them to be influenced by the addition of the slats.

Figure 7.10 shows the effect of adding up to six slats (configuration 1) and removing them at each configuration from the top down, when the vehicle was fitted with a flat floor. When six slats are in place (configuration 1) there is a drag reduction of up to 4 counts, however when the upper slat is removed in configurations 2-6 there is no reduction in drag. These results indicate that in order to

achieve a change in drag it is either the upper slat that is important or the presence of all the slats that cause the change.

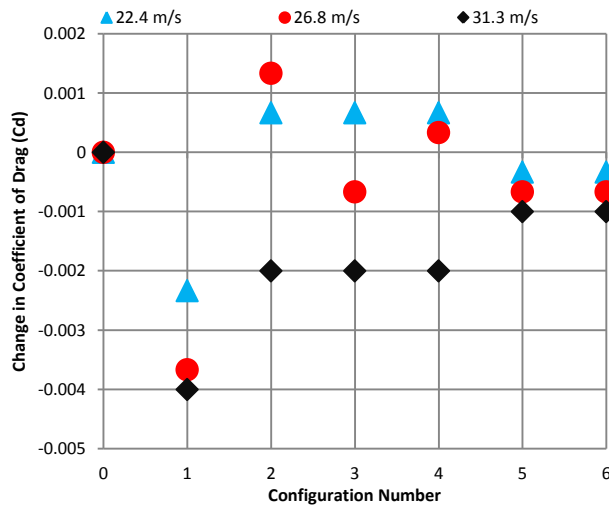


Figure 7.10 - Change in C_d vs configuration number

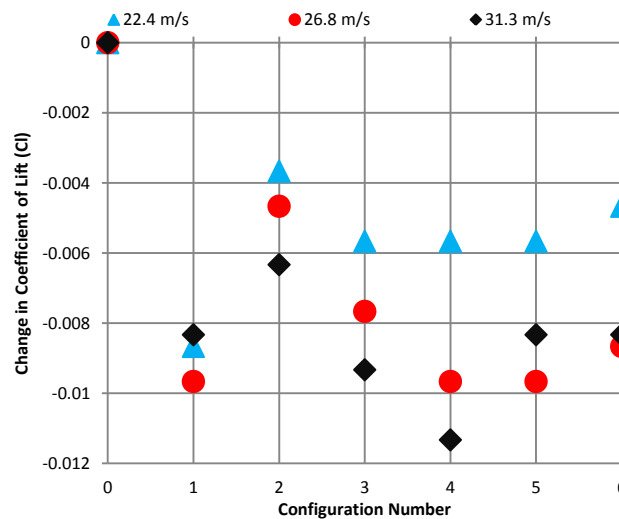


Figure 7.11 - Change in C_l vs configuration number

Figure 7.11 shows the changes in lift when slats are added and although lift is reduced when all six slats are in place by up to 10 counts, it is also the case that lift is reduced in configurations 2-6 where no changes in drag were observed. It is clear some modification to the flow structure around the rear of the vehicle and in the wake must be occurring to create the changes in drag seen in configuration 1 and the consistent changes in lift seen throughout configuration changes 2-6.

Figure 7.12 shows the changes in base pressure for configuration 1 relative to the base pressures of the baseline configuration. A global base pressure increase occurs above $0.2H/h$ from the floor of the vehicle, whilst an increase in suction occurs across the lower 20% of the base region. The changes do not show the high concentration of high pressure across the width of a single slat as seen at model

scale in Figure 7.8 and Figure 7.9, indicating that the means by which the base pressures are modified may be different. However, the slats applied are a uniform two dimensional physical addition across the width of the base, and the resulting changes in base pressure are relatively uniform across the width of the vehicle.

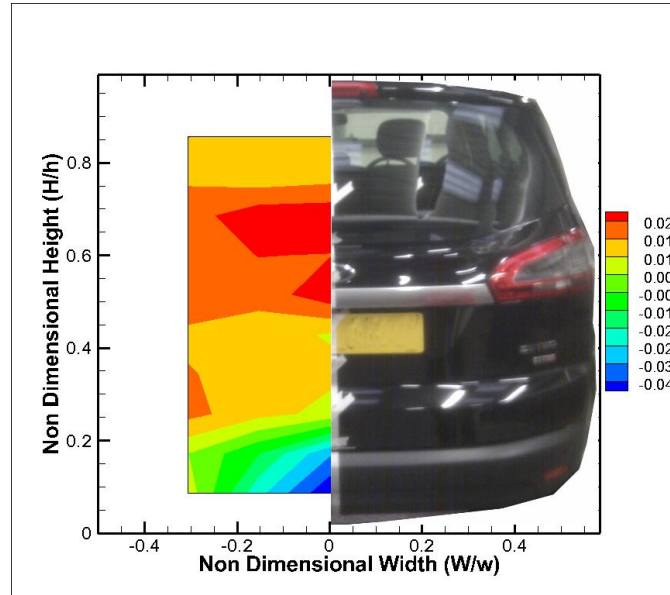


Figure 7.12 – Change in base pressure (C_p) with 6 slats applied

Examination of the baseline base pressure distribution individually infers a three dimensionality of the wake flow. When 6 slats are added the individual base pressure distribution for configuration 6 shows a much more uniform wake flow structure across the width of the base. This phenomena is similar to the effect seen at model scale where the wake is forced into a more 2 dimensional regime.

7.4 Discussion

A small passive modification has been tested in ¼ scale and full scale wind tunnel tests. The addition of low profile horizontal slats to the base surface of the scale model produced drag reductions of up to 8 counts and lift reductions of up to 32 counts.

Pressure measurements on the base of the model showed that the interaction of the upper slat with the recirculating vortex structure in the wake creates a region of increased pressure above the upper slat. Additionally pressure was recovered in the lower half of the base where the suction regions associated with the presence of the lower vortex structure are located.

At full scale the addition of horizontal slats to the base of the vehicle created drag reductions of 4 counts and lift reductions of 10 counts. Tests conducted without a smooth underfloor showed little or no change to the lift and drag forces.

In the full scale configurations where force changes were observed pressure measurements showed a global recovery of base pressure on the base above $0.2H/h$ from the floor of the vehicle; below $h/H=0.2$ a reduction in base pressure was observed. A lack of understanding of the standard full scale vehicle wake structure means the aerodynamic force changes observed cannot be explained as easily as the scale model results.

Further investigation is required to fully understand how such a small passive modification can cause such large force changes observed at full scale. However the changes implemented in the current test are physically small and located in the wake of a squareback vehicle. Such small modifications in the wake region would not normally be addressed in an aerodynamic optimisation process since small changes on the base region of a vehicle have previously been considered unimportant. Any changes in this region which have previously been effective have required large physical changes, or trailing edge modifications such as tapering or tripping. With this in mind the reductions in lift and drag as a result of the configurations tested have been surprisingly large.

The pressure results in Figure 7.8 and Figure 7.9 go some way to explaining how the wake structures can interact with the base slats to cause body force changes in the scale model tests. However an area weighted calculation based on the contribution from these small slats shows that the changes in lift cannot be explained by pressure changes on the horizontal surfaces of the slats themselves, due to their small horizontal area (as a percentage of the whole vehicle horizontal area).

Further investigation using tappings located on the floor and roof of the model may identify if the lift reduction using the base slats is caused by pressure changes on the floor of the model by accelerating flow underneath it. Although the mechanisms involved in creating the changes on the full scale model are still not understood, it is clear that small changes in the physical architecture of the vehicle/model relationship can have an effect on where the base slats are effective. This is thought to be due to the differences in the wake structures found in the two experiments. None of the base slats tested at full scale without a flat floor had an effect, again highlighting the sensitivity to wake structure changes.

The use of moving ground simulation and rotating wheels will also influence the flow under the vehicle and the structure of the wake. As a result the optimum position of the slats may be further influenced by these changes in the test conditions, which may have to be addressed in any vehicle optimization process.

Chapter 8

CONCLUSIONS AND FURTHER WORK

8.0 Conclusions and Further Work

It has been shown that reducing C_d of road vehicles can result in significant CO_2 emissions reductions and that new technologies associated with reducing C_d are a worthy field of research.

Many passive and active drag reduction technologies and systems have been reviewed and in the current thesis a focus has been given to the analysis of a synthetic jet system, steady blowing, and pulsed blowing for vehicle drag reduction. Early experiments on a 2D cylinder have shown synthetic jets to work to control flow in laminar, transitional and turbulent boundary layers, however a lack in C_μ has meant a lack in performance at higher freestream velocities. Although SJ's offer an attractive package to create a pulsed disturbance to freestream flows, the practicalities surrounding these systems currently restricts their application to controlled experimentation at representative Reynold's numbers. These practicality limitations also have significant implications for the uptake of the technology into mainstream road vehicle production. Without significant developments in the actuators available to enable a 'flexible' synthetic jet arrangement the technology will not currently be applicable to full scale applications. A 'flexible' synthetic jet would be defined as an actuator that can offer significant momentum coefficients at a wide range of actuation frequencies with a low energy demand. For the reason above synthetic jet actuators were not applied to a road vehicle model. However the use of steady blowing and pulsed blowing was investigated on a scaled vehicle model.

Before applying the technology to a vehicle model a simple passive optimisation was conducted to investigate how wake modification can affect base pressure. These investigations highlighted that wake size and 'in wake' flow topologies are the main factors influencing the pressures on the base surface. The baseline vehicle investigations also revealed that there was no clear shedding patterns from the upper or lower surfaces, but there was some non-coherent shedding occurring which was characterised as a Markovian process.

The application of steady blowing at the upper and lower rear edges of the vehicle model create attractive reductions in drag forces. The reductions are also still viable when the energy demands of the actuation systems are accounted for. In these experiments the global size of the wake was not modified as significantly as in the passive optimisation experiments, yet the drag changes were more significant. The influence of a large lower vortex structure on the base pressures was identified as a significant mechanism in the creation of the drag savings. In the cases where drag was reduced by steady blowing, the vorticity found in this lower structure was also reduced. Although there is a net drag saving the energy requirements of a blowing system would still be significant, requiring the generation of large mass flow rates and potentially significant storage tanks. These factors all inhibit the applicability to larger road vehicles. It is suggested that further work could investigate the use of

local ducting on the upper and lower surfaces to try to re-direct freestream flow into the wake in the same manner that the current jets were oriented. Although it is acknowledged that the ducting itself will create adverse drag savings it may be that these can be compensated for by the positive effects created in the wake as a result of 'blowing'. In the current investigation an attempt to reduce the duty cycle of the jets, a new system was implemented where the jets were pulsed on and off.

The application of pulsed jets found drag reduction was created at low frequency actuation but the savings were reduced as the frequency was increased. In most cases the drag was actually increased relative to the baseline case at higher actuation frequencies. After investigation of PIV data it was found that as frequency is increased so too is the level of vorticity found close to the base. Again a link was drawn between the vortex strength or vorticity in the large lower vortex structure, and the changes in base pressures. The reduction in energy demands required to create mass flow for the jets created by pulsing them will not go far enough to create a clear path for the implementation of the current technology in standard vehicles.

Although the current work did not find clear drag reductions as a result of pulsing the jet, there are clearly significant modifications to the flow with the increased frequencies. Specifically as the frequency is increased wake size is modified more significantly, but more importantly, the vorticity levels in the wake are increased. It is suggested that further work with the current model could experiment with higher frequencies to investigate if the trend linking vorticity to increased frequencies continues, or if another behavioural regime can be created. Either way it is clear that a reduction in vorticity or a change in the position/size of the lower vortex will have a significant effect on any changes in base pressure created, and the focus of further work using this model should target the lower vortex structure. Additionally the current work highlights that vorticity intensity and location, even within wake flows, can contribute significantly to resultant surface pressures. As a result it would be of value to re-visit work on wake flows with different shaped vehicle models, using modern measurement techniques such as PIV, to investigate the presence of vorticity located close to rearward surfaces, that previously may have been regarded as unimportant.

In other applications, such as underbody diffuser flows, it can be the case that vorticity is a desirable characteristic, where vortices are used to create down force. In this application pulsed jets may create benefits with their ability to increase vorticity.

Knowing the negative effects vorticity can create in wake flows on the current model some small passive devices were used to test the theory. From the work carried out in Chapter 7.0, it is clear that wake size manipulation is not the only means of creating base pressure recovery and lift changes, and detailed optimisation on the base surface may be a means of further aerodynamic optimisation. The

flow mechanisms involved in creating the observed changes are still not fully understood and the transient nature of wake flows makes the understanding a difficult task. However it is clear that with an optimisation process applied to a specific vehicle shape, drag and lift modification may be possible if there is the presence of any quasi-stable vortical structures.

9.0 References

Ahmed, S.R. and Baumert, W. (1979) *The Structure of Wake Flow Behind Road Vehicles*, Proc. ASME-CSME. Conf. Aerodynamics of Transportation.

Ahmed, S.R., Ramm, G. and Faltin, G. (1984) *Some Salient Features of the Time Averaged Ground Vehicle Wake*, SAE Technical Paper 840300, doi:10.4271/840300.

Amitay, M. and Glezer, A. (2002) Role of Actuation Frequency in Controlled Flow Reattachment over a Stalled Airfoil, AIAA Journal Vol. 40, No. 2, February 2002.

Barnard, R.H. (1996) *Road Vehicle Aerodynamic Design*, Addison Wesley Longman, Harlow.

Bearman, P.W. (1965) Investigation of the flow behind a two-dimensional model with a blunt trailing edge and fitted with splitter plates, J. Fluid Mech. (1965), vol. 21, part 2, pp. 241-255.

Bearman P.W., a.M.T. (1983) *Effect of freestream turbulence on flow around bluff bodies*, Prog. Aerospace Science Vol 20 1983. 97-123.

Beaudoin, J.-F. and Aider, J.-L. (2008) *Drag and lift reduction of a 3D bluff body using flaps*, Exp Fluids (2008) 44:491–501.

Béra, J.-C., Michard, M., Sunyach, M. and Comte-Bellot, G. (2000) *Changing lift and drag by jet oscillation: experiments on a circular cylinder with turbulent separation*, Eur. J. Mech. B - Fluids 19 (2000) Pg 575–595.

Brazaa, M., Perrina, R. and Hoarau, Y. (2006) *Turbulence Properties in the Cylinder Wake at High Reynolds Numbers*, Journal of Fluids and Structures, 22 (2006) Pg 757–771.

Brunn, A. and Nitsche, W. (2006) *Active control of turbulent separated flows over slanted surfaces*, International Journal of Heat and Fluid Flow 27 (2006) Pg 748–755.

Carr, G.W., Atkin, P.D. and Sommerville, J. (1994) *An empirically-based prediction method for car aerodynamic lift and side forces*, SAE Technical Paper 1994-11-0100.

Ching, W.K. and Ng, M.K. (2006) *Markov Chains; Models, Algorithms and Applications*, ISBN 978-0-387-29337-0.

Coleman, H.W. and Steele, W.G., (1999) *Experimentation and Uncertainty Analysis for Engineers*, 2nd Edition, John Wiley & Sons, Inc., New York, NY.

Cooper, K.R., Bertenyi, T., Dutil, G. and Syms, J. (1998) *The Aerodynamic Performance of Automotive Underbody Diffusers*, SAE Technical Paper 980030.

Duel, E.G. and George, A.R. (1993) *Measurements in the Unsteady Near Wakes of Ground Vehicle Bodies*, SAE Technical Paper 930298.

Englar, R.J. (1987) The application of circulation control pneumatic technology to powered-lift STOL aircraft, SAE Technical Paper 872335.

Englar, R.J. (2003) Drag Reduction, Safety Enhancement, and Performance Improvement for Heavy Vehicles and SUVs Using Advanced Pneumatic Aerodynamic Technology, SAE Technical Paper 2003-01-3378.

Englar, R.J. (2005) Improved Pneumatic Aerodynamics for Drag Reduction, Fuel Economy, Safety and Stability Increase for Heavy Vehicles, SAE Technical Paper 2005-01-3627.

Geropp, D. and Odenthal, H.-J. (2000) *Drag Reduction of Motor Vehicles by Active Flow Control Using the Coanda Effect*, Experiments in Fluids 28 (2000) Pg 74-85.

Glezer, A. and Amitay, M. (2002) *Synthetic Jets*, Annual Review of Fluid Mechanics 34 Pg 503-529.

Glezer, A., Amitay, M. and Honahan, A.M. (2005) *Aspects of Low- and High-Frequency Actuation for Aerodynamic Flow Control*, AIAA Journal Vol 43 No.7 July 2005.

Guo, F. and Zhong, S. (2006) A PIV Investigation of the Characteristics of Micro-scale Synthetic Jets, AIAA paper 2006-3183.

Heisler, H. (2002) *Advanced Vehicle Technology*, 2nd Edition, Butterworth-Heinemann, Oxford.

Hollis, D. (2004) Particle Image Velocimetry in Gas Turbine Combustor Flow Fields, PhD Thesis, Loughborough University.

Holman, R. and Utturkar, Y. (2005) *Formation Criterion for Synthetic Jets*, AIAA Journal Vol. 43, No. 10, October 2005.

Horn, H..N.J..a.W.J. (n.d) 'Rating Mass-related Energy Demand for Vehicles with New Powertrain Concepts'.

Howell, J. and Le Good, G. (2008) The Effect of Backlight Aspect Ratio on Vortex and Base Drag for a Simple Car-Like Shape, SAE Technical Paper 2008-01-0737.

Howell, J., Sheppard, A. and Blakemore, A. (2003) *Aerodynamic Drag Reduction for a Simple Bluff Body Using Base Bleed*, SAE Technical Paper 2003-01-0995.

Hucho, W.H. (1998) *Aerodynamics of Road Vehicles*, SAE International.

Jowsey, L. (2008) *An Experimental Study of an Automotive Underbody Diffuser*, PhD Studies, Loughborough University.

Keating, A., Shock, R. and Chen, H. (2008) Lattice Boltzmann Simulations of the Unsteady Flow Behind the Ahmed Body, 2008010740th edition.

Kee, J.D., Kim, M.S. and Lee, B.C. (2001) The COANDA Flow Control and Newtonian Concept Approach to Achieve Drag Reduction of Passenger Vehicles, SAE Technical Paper 2001-01-1267.

Khalighi, B., Zhang, S. and Koromilas, C. (2001) 'Experimental and Computational Study of Unsteady Wake Flow Behind a Bluff Body with a Drag Reduction Device'.

Kim, Y.H. and Gary, K.P. (2006) Optimization of a Rectangular Orifice Synthetic Jet Generator, AIAA paper 2006-2862.

Kourta, A. (2008) *Separated Flow Control and Actuators Development*, Presentation, KATnet II, Separation and Control Workshop, 1-3 April 2008, ONERA, Toulouse, France. Web link: http://www.kat-net.net/publications/data/64_20080423_%5B5%5D_kourta.pdf.

Kowata, S., Ha, J., Yoshioka, S., Kato, T. and Kohama, Y. (2008) *Drag Force Reduction of a Bluff-Body with an Underbody Slant and Rear Flaps*, SAE Technical Paper 2008-01-2599.

Lanser, W.R. and Ross, J.C. (1991) Aerodynamic Performance of a Drag Reduction Device on a Full-Scale Tractor/Trailer, SAE Technical Paper 912125.

Le Good, G.M., Howell, J.P. and Passmore, M.A. (1995) *On-road aerodynamic drag measurements compared with wind tunnel data*, SAE Paper 950627.

Leclerc, C. and Levallois, E. (2006) Aerodynamic Drag Reduction by Synthetic Jet: A 2D Numerical Study Around a Simplified Car, AIAA Flow Control Conference Paper 2006-3337.

Lockerby, D.A. and Carpenter, P.W. (2004) *Modeling and Design of Microjet Actuators*, AIAA Journal Vol. 42, No. 2, February 2004.

Mason, W.T. and Beebe, P.S. (1976) *The Drag Related Flow Field Characteristics of Trucks and Buses*, Aerodynamic Drag Mechanics of Bluff Bodies and Road Vehicle Symposium, held at General Motors Research Laboratory, Warren, Michigan, September 27-28, 1976.

McKormick, D.C. (2000) Boundary Layer Separation Control with Directed Synthetic Jets, AIAA paper 2000-0519.

Mittal, R. and Rampungoon, P. (2002) *On the virtual aeroshaping effect of synthetic jets*, Physics of Fluids Volume 14, Number 4 April 2002.

Modi, V.J. (1997) *Moving Surface Boundary-Layer Control: a Review*, Journal of Fluids and Structures (1997) 11 Pg 627-663.

Modi, V.J. and Ying, B. (1990) Boundary-Layer Control of Bluff Bodies Through Momentum Injection, SAE Technical Paper 902225.

Pastoor, M., Henning, L., Noack, B.R., King, R. and Tadmor, G. (2008) *Feedback shear layer control for bluff body drag reduction*, J. Fluid Mech., vol. 608, pp. 161–196.

Peterson, R.L. (1981) Drag Reduction Obtained by the Addition of a Boattail to a Box Shaped Vehicle, NASA Contractor Report 163113.

Plackett, L. (2009) *Experimental analysis of impulsively started jet flow*, Loughborough University, Masters Thesis.

Raffel, M., Willert, C.E., Wereley, S.T. and Kompenhans, J. (2007) *Particle Image Velocimetry - A Practicle Guide*, Springer ISBN 978-3-540-72308-0.

Ribaldone, E.. (n.d) 'Application of mulit-objective optimization to the aerodynamic development of passenger vehicles at FIAT'.

Roshko, A. (1961) Experiments on the Flow Past a Circular Cylinder at Very High Reynolds Number, *Journal of Fluid Mechanics* 10 Pg 345-356.

Roumeas, M. (2006) *Contribution à l'analyse et au contrôle des sillages de corps épais par aspiration ou soufflage continu*, PhD Thesis Institut de Mécanique des Fluides de Toulouse - IMFT (Toulouse, France).

Rouméas, M., Gilliéron, P. and Kourta, A. (2006) *Analyze and Control of the Near-Wake Flow over a Square Back Geometry*, AIAA paper 2006-3336.

Schrefl, M. (n.d) 'The Audi A1 – Aerodynamics and Aeroacoustics'.

Schultz, S. (2010) *Aerodynamics of Modern Sport Utility Vehicles*, Technical Paper, 8th MIRA International Vehicle Aerodynamics Conference.

Sharma, R.N. (2006) An Analytical Model for Synthetic Jet Actuation, AIAA paper 2006-3035.

Smith, B.L. and Glezer, A. (2002) *Jet Vectoring Using Synthetic Jets*, *J. Fluid Mech.* Vol. 458 Pg 1-34.

TrailerTail (2007) <http://www.atdynamics.com/trailertail.htm>.

Verzicco, R., Fatica, M., Iaccarino, G. and Moin, P. (2002) *Large Eddy Simulation of a Road Vehicle with Drag-Reduction Devices*, *AIAA Journal* Vol. 40, No. 12.

Wong, D.T.M. and Mair, W.A. (1983) *Boat-Tailed Afterbodies of Square Section as Drag Reduction Devices*, *Journal of Wind Engineering and Industrial Aerodynamics*, 12 (1983).